WILDFIRES IN EARTH SYSTEM: DRIVER, TRANSPORT AND FEEDBACK

A Dissertation
Presented to
The Academic Faculty

by

[Ziming Ke]

In Partial Fulfillment
of the Requirements for the Degree
Doctor of Philosophy in the
Earth and Atmospheric Science

Georgia Institute of Technology
August 2018

WILDFIRES IN EARTH SYSTEM: DRIVER, TRANSPORT AND FEEDBACK

Approved by:

Dr. Yuhang Wang, Advisor
School of Earth and Atmospheric Science
Georgia Institute of Technology

Dr. Robert X. Black
School of Earth and Atmospheric Science
Georgia Institute of Technology

Dr. Yi Deng
School of Earth and Atmospheric Science *Georgia Institute of Technology*

Dr. Hanqin Tian
School of Forestry and Wildlife Sciences
Auburn University

Dr. Yongqiang Liu
Southern Research Station
U.S. forest Service

Date Approved: April 23rd, 2018

ACKNOWLEDGEMENTS

Firstly, I would like to express my sincere gratitude to my advisor Prof. Yuhang Wang for the continuous support of my Ph.D. study and related research, for his patience, motivation, and immense knowledge. His guidance helped me in all the time of research and writing of this thesis. I could not have imagined having a better advisor and mentor for my Ph.D. study.

Besides my advisor, I would like to thank the rest of my thesis committee: Dr. Robert X. Black, Dr. Yi Deng, Dr. Hanqin Tian and Dr. Yongqiang Liu, for their insightful comments and encouragement, but also for the hard question which incented me to widen my research from various perspectives.

I thank all Dr.Wang's group members, especially Jianfeng Li and Yufei Zou, for the discussions and suggestions in four years. Also, I thank the kind support and advices from Dr. Jia Yang and Dr. Sufen Pan in Auburn University.

Last but most important, I would like to thank my family: my wife, my daughter and my parents for supporting me spiritually throughout writing this thesis and my life in general. Without them, I would not finish any research.

TABLE OF CONTENTS

LIST OF TABLES

LIST OF FIGURES

SUMMARY

Wildfires release large amounts of greenhouse gases, carbonaceous aerosols, and other pollutants, therefore having complex impacts on the earth climate, local weather, and air quality. The plume heights (smoke injection height) are important for calculating the transport and lifetime of wildfire emitted pollutants, which can significantly affect regional air quality and atmospheric radiation budget. This research has developed an observation-based global plume-rise dataset, a modified one-dimensional plume-rise model was used with observation-based fire size and Maximum Fire Radiative Power (MFRP), which are derived from satellite fire hotspot measurements of Fire Radiative Power (FRP) as a function of plant functional type (PFT) for different regions, to compute plume rise heights. The resulting dataset from 2002 to 2010 captured well the observed plume height distribution derived from the Multi-angle Imaging SpectroRadiometer (MISR) measurements. In general, the average fire plume rise height increases with latitude reflecting in part an increase of fire intensity. A key parameter for the impacts of fire emissions is the fraction of fire plumes penetrating above the boundary layer. While at the time of MISR observation (10:30 am LT) it is relatively low at 20%, the fraction increases to an average of ~55% in the late afternoon when the atmosphere is most unstable. By integrating plume heights into wildfire emission data, 3 community atmospheric models 5.0 (CAM5) runs were performed: control run, plume smoke run and surface smoke run. The resulted in AOD associated with wildfires well captured the pattern shown by satellite observed smoke related AOD distribution. The impacts of the plumes were investigated, and the results showed the plume rise enhanced AOD downstream of the wildfire spots by

20 to 50% and slightly reduced the AOD near wildfires in both topics and high latitudes, reflecting its impacts on pollutant transport and atmospheric radiative balance. The offline plume rise data are further applied to implement an online plume rise module in the Community Atmospheric Model version 5, allowing for the feedbacks of climate/weather on fire plume rise.

As an application of the developed plume height dataset, the impact of West Canada wildfires (WCWs) have been investigated. Fire emitted aerosols can significantly affect air quality and increase the ratio of organic carbon (OC) to elemental carbon (EC) in downwind regions. The observed OC/EC ratios at the Interagency Monitoring of Protected Visual Environments (IMPROVE) network sites over the Northeast United States (NEUS) show significant correlations with WCWs burned area in June from 2001 to 2015. Satellite observations of aerosol optical depth (AOD) corroborates this correlation. Detailed analysis of the observations and ensemble modeling simulations using the atmospheric community model version 5 (CAM5) show that both WCWs intensity and atmospheric transport are the factors controlling the disturbance of OC/EC and AOD over the NEUS. A high lower tropospheric latitudinal pressure gradient over eastern North America (i.e., a low-pressure system over Eastern Canada and a high-pressure system over the Southeast U.S.) leads to a strong effect of WCWs on the NEUS. While the strength of WCWs (wildfire index) explains 48% variance of the OC/EC ratio perturbation over NEUS, the transport effect explains another 35% variance.

Africa wildfires response to half of global fire emissions. To investigate the driver of the wildfire variability, the relationship between fire, climate, and ecosystem are examined in arid, intermediate and mesic regions. The results show that the wildfires are

significantly link to LAI through all the regions, indicating the fuel availability has significant impact on wildfire variability. In the arid region, the LAI is driven by precipitation, while the cloudiness could potentially impact on LAI in mesic region.

Through suppressing the tree sapling recruitment, the fire-forest interaction is recognized as an important disturbance to produce the savanna-forest landscape in Africa. This study present new evidence about the fire-forest interaction, by analyzing the MODIS landcover data and the GFED burned area data. The results show significant lag correlations between the burned area and the forest amount in both hemisphere Africa savanna area during 2001 to 2012, with correlation coefficients -0.56 and -0.75. It motivates the investigation to what extent the fire suppression could promote the reforestation to reach the RCP4.5 forest landcover target in Africa by 2100. An ecosystem model has been modified to include the fire-forest feedback explicitly, the land patch interaction and capable to be driven by the change of the fire. The model forced by current fire well reproduced the current landscape in Africa with correlation coefficient value 0.8. Ensemble runs have been performed with broad range of parameter values, suggesting that 90% of the fire needs to be reduced compared to 2005 level to reach the RCP4.5 forest target in 2100.

CHAPTER 1. INTRODUCTION

Wildfires release large amounts of greenhouse gases, carbonaceous aerosols, and other pollutants, therefore having complex impacts on the earth climate, local weather, and air quality. The amount of carbon released from fires (2-4 Pg C yr^{-1}) is up to half of the amount of carbon resulted from fossil-fuel combustion (7 Pg C yr^{-1}) (e.g., Browman et al., 2009; van der Werf et al., 2006). In addition to greenhouse gases, carbonaceous aerosols (organic and black carbon) released in fire smokes modulate atmosphere and earth surface radiative forcing balance directly through scattering and absorbing solar radiation and indirectly through changing cloud properties (e.g., Bauer & Menon, 2012; Boucher et al., 2013; Jiang et al., 2016). Climate model experiments indicated that the organic carbonaceous aerosols generally increase the Aerosol Optical Depth (AOD) and reduce surface temperature, while fire emitted black carbon aerosols enhance heat absorption in the troposphere and increase air temperature; the combination of these two effects could potentially suppress atmospheric convection and subsequently affect global circulations (e.g., Bauer and Menon, 2012; Tosca et al., 2013a). In the tropics, previous studies highlighted the role of black carbon in changing the Hadley circulation and precipitation patterns (Allen et al., 2012; Hodnebrog et al., 2016; Tosca et al., 2015). At the middle to high latitudes, previous studies indicated potential impacts of smoke emissions on regional climate and weather patterns (Grell et al., 2011; Liu, 2004; Madden et al., 2015), even hazard weathers (Pablo E. Saide et al., 2016). Additionally, strong evidence was found linking the Arctic air quality and high latitudes wildfires during spring and summer

(Evangeliou et al., 2016; Monks et al., 2012; Winiger et al., 2016) and for its potential impacts on Greenland ice shelves melting (Keegan et al., 2014).

Beside its impact on climate, the wildfires around the world produce a great amount of the black carbon (BC), organic carbon (OC) and other pollutants (Giglio et al., 2013; Jaffe et al., 2008; Randerson et al., 2012), and largely contribute to fine particulate matters (PM2.5) through directly emitting primary organic matters (POM) and the formation of secondary organic aerosols (SOA). Although the total amount of pollutants released by wildfires is relatively smaller than anthropogenic emissions (Van Der Werf et al., 2010), the spatial and temporal variations of wildfires contribute variability and uncertainty to OC, EC and PM2.5 concentrations in U.S. (Hu et al., 2008; Park et al., 2007; Zeng and Wang, 2011) and all over the world (Giglio et al., 2013; Liu et al., 2014). Epidemiologic studies have revealed that the exposure to PM2.5 significantly increases the risk for cardiorespiratory morbidity and mortality (Arden Pope III et al., 2009; Delfino et al., 2005; Donaldson et al., 2001) and particularly emphasize the wildfires' impacts on public health (Künzli et al., 2006). Recent studies suggest that the water-soluble organic matters in PM2.5 associated with dithiothreitol (DTT) activity may measurably increase the emergency department visits, which relates to asthma and wheezing attacks and congestive heart failure, and attribute the majority of these harmful organic matters to wildfires (Bates et al., 2015; Fang et al., 2016).

1.1 The importance of plume heights on wildfire pollutants transport

To accurately simulate the impacts of wildfire emissions, a crucial parameter is plume height or injection height, defined as the altitude at which wildfire smoke emissions are released into the atmosphere. This parameter affects the transport of emitted pollutants and thereby influences climate and air quality in the broader downwind regions. Generally, if the plume heights are above the Atmospheric Boundary Layer (ABL), the emissions can penetrate into the free troposphere and be transported to locations further away from the ignition sources in part because of higher wind speed in the free troposphere than the ABL; in comparison, if the plume heights are within the ABL, the impacts of pollutants are restricted to smaller regions (e.g., Liu et al., 2014; Paugam et al., 2016).

The reported fire plume heights range from completely within the ABL, less than 600 meters (Trentmann et al., 2002), to free troposphere (de Gouw et al., 2006), even the stratosphere (Dirksen et al., 2009). The plume heights derived from the Multi-angle Imaging SpectroRadiometer (MISR) stereo imaging developed by Kahn et al. (2007) were widely used to evaluate model simulated plume height data (e.g., Kahn et al., 2008; Tosca et al., 2011; Val Martin et al., 2009) with a resolution of 500 m in the vertical and 1.1 km in the horizontal (Kahn et al., 2007). The global MISR wildfire plume height dataset is available at https://www-misr.jpl.nasa.gov/getData/accessData/MisrMinxPlumes/.

A somewhat surprising result of the MISR fire plume height data is that the fraction of fire plume height above the ABL is relatively low, ~10% over North America (Kahn et al., 2008; Val Martin et al., 2009) and only 4% in Southeast Asia (Tosca et al., 2011). However, the MISR instrument is onboard the sun-synchronous Terra satellite; its local equatorial crossing time is approximately 10:30 a.m. Hence MISR data only reflected fire plume heights in the late morning and likely missed the daily maximum fire plume heights

that would occur in the late afternoon due to the diurnal cycle of wildfires intensity (Ellicott et al., 2009) and unstable BL conditions (Sofiev et al., 2012).

Therefore, my thesis developed a fire plume height dataset that captures the diurnal variation on a global scale is needed to improve the understanding of the temporal and spatial variability of fire plume heights and their impacts. Also, the developed plume height dataset is used to study the impact of the Canadian wildfires on northeast U.S. (NEUS), because of its long-distance transport of the pollutants. Furthermore, this thesis formulates a parameterization for use in climate model applications for on-line simulation purpose.

To develop the plume height dataset, we use the 1-D plume-rise model by Freitas et al. (2006, 2010). The governing equations of this model are based on first principles of thermodynamics, vertical momentum flux, and continuity equation. Val Martin et al. (2012) applied this model with MODIS Fire Radiative Power (FRP) and assimilated GEOS meteorology data to calculate the wildfire plume heights over North America for the 2002 and 2004-2007 fire seasons, and compared the results with the MISR plume heights. They suggested that the plume-rise model tends to underestimate the observed plume heights, but ignored the diurnal variation of wildfire plume heights. The relatively coarse spatial (2^{o}x2.5^{o}) and temporal (6 hrs) resolutions may have contributed to the model biases due to the sensitivity of wildfire plume height to ambient meteorological conditions (Sofiev et al., 2012).

Using assimilated high-resolution meteorological reanalysis and satellite observations, this thesis improved upon previous studies to develop an observation-based (offline) global fire plume height dataset from 2002 to 2010 with diurnal variability and to

formulate an online parameterization of fire plume height for a climate model. The results of these work are detailed in Chapter 2.

1.2 The impact of wildfire on NEUS air quality

The Northeast U.S. (NEUS) is one of the most populated regions in U.S., including New York City, Boston, and Philadelphia. The intrusions of pollutant plumes caused by eastern Canadian wildfires have attracted research attention in recent years (e.g., Kang et al., 2014; McKeen et al., 2002; Sapkota et al., 2005; Saunders and Waugh, 2015) and it is probably due to two reasons. The first reason is the increase of wildfires over North America in recent decades (Giglio et al., 2013; Westerling et al., 2006) and the second reason is the regional decrease of anthropogenic emissions due primarily to regulatory measures (Fiore et al., 2014; Gégo et al., 2007). The impacts of wildfires plumes on regional aerosol optical depth (AOD) were characterized (Adam et al., 2004; Colarco, 2004) and the extreme PM2.5 violation events associated with wildfires plume invasion during summer were examined (e.g. DeBell et al., 2004; Fiore et al., 2014; Sapkota et al., 2005; Saunders and Waugh, 2015). Studies also reported that the east Canada wildfires significantly increased the surface ozone concentrations in the NEUS region by the increase of the ozone precursors (Dreessen et al., 2016; Jaffe and Wigder, 2012; Kang et al., 2014; Saunders and Waugh, 2015).

As described above, the most studies about the wildfires' impact on NEUS are focus on east Canadian wildfires located at north of NEUS, and focus on individual wildfire plume invasion events, while the study about the long-range transport of pollutants from

the West Canada Wildfires (WCWs) to the NEUS is little, although the WCWs are more intense than the east Canada wildfire. However, recent study suggested that the WCWs' pollutants had been transported to Ontario, Canada in 2010 (Dempsey, 2013), which is close to NEUS, and its long-term impact on Toronto, Ontario air quality has been reported by Lutsch et al. (2016), suggesting that the WCWs' potential long-term impact on NEUS air quality during the fire season.

Therefore, my thesis has investigated the impact of the WCWs on NEUS air quality on the decadal timescale. The OC/EC ratio derived from the Interagency Monitoring of Protected Visual Environments (IMPROVE) network sites are used as the proxy to track carbonaceous pollutants resulted from wildfires. The value of OC/EC ratio is generally high from wildfires emission compared to other sources (Andreae and Merlet, 2001). Additionally, the wildfires contribute much more interannually variations to the OC/EC ratio during the fire season compared to the relatively stable OC/EC ratio caused by anthropogenic emissions (Zeng and Wang, 2011). Importantly, the higher OC/EC ratio implies higher wildfire caused organic matter concentration, which is closely associated with DTT activity risking public health (Bates et al., 2015).

In this part of thesis, the long-term impact of the WCWs on NEUS air quality disturbance has been analyzed, and the atmospheric circulation pattern associated with this long-range transport have been examined. A linear regression model has been built to reproduce the NEUS regional OC/EC ratio, and the climate model experiment has been performed to verify the transport. The results about this study are detailed in chapter 3.

1.3 The variability of wildfires in Africa

The Africa wildfire is responsible for 70% of global burned area and 50% of fire-related carbon emissions (Giglio et al., 2013; Van Der Werf et al., 2010). Northern Hemisphere Africa (NHAF) and Southern Hemisphere Africa (SHAF) are two regions separated by equator. The movement of Intertropical Convergence Zone (ITCZ) largely influences the precipitation pattern in Africa. Its north-south movement, caused by the surface pressure change over the continent, results in the opposite wet/dry season in NHAF and SHAF. Both satellite data and model simulation results show that the Africa precipitation generally increased over recent three decades, probably due the strengthening of Walker circulation and Sea Surface Temperature (SST) anomalies related to ENSO (Maidment et al., 2015). However, the burned area in NHAF and SHAF display opposite trends: a gradual decrease of 1.7 Mha yr^{-1} (-1.4% yr^{-1}) in NHAF and a gradual increase of 2.3 Mha yr-1 (+1.8% yr^{-1}) in SHAF (Giglio et al., 2013).

Studies try to explain these contradictory effects of precipitation on wildfires by distinguish precipitation's impact in arid and mesic regions and tends to related the wildfire variability to the precipitation changes (Andela and van der Werf, 2014a; Chen et al., 2016a; Van Der Werf et al., 2008). In arid region, where water availability limits the growth of vegetation, wildfires are largely controlled by the fuel availability, thus the precipitation is positively related to the wildfire amount (van Wilgen et al. 2000). On the other side, precipitation prevents vegetation from wildfires in the wet region, by shrinking the fire season and keeping fuels drying out, suggesting a negative correlation between the precipitation and wildfires (Barbosa et al., 1999; Stroppiana et al., 2000). Although the fire increase in SHAF can be attributed to the positive precipitation-fire effect, the observed

correlation between fire and precipitation is week in NHAF. To further explain the reduction of fire in NHAF, the human driven cropland increase is take into consideration (Andela et al., 2017).

However, there is a great deficit between the rate of cropland increase (0.28% yr-1 of total land area) and the rate of wildfire decrease (2-7% yr-1 of total land area) over NHAF (Ichoku et al., 2016). Furthermore, the boundary of the fuel limited region is vague and previous ecosystem study shows that the most savanna ecosystems fire could be fuel limited rather than only in arid area (Griffin et al., 1983). Beside water, the temperature and cloudiness are also controlled the vegetation growth (Seddon et al., 2016). This suggests that the fuel availability could impact the wildfire beyond the arid area. In the mesic region, the factor could impact the fuel availability is the cloudiness. The long-term satellite observation since 1982 show the vegetation growth in Africa mesic region is primarily related to the cloudiness and solar radiation strength (Neami et al., 2003; Seddon et al., 2016). In the wet season, the increasing cloudiness could attenuate the strength of surface solar radiation and then reduce the photosynthesis of plant (Myneni et al., 2007).

Therefore, this thesis examines the relationships between precipitation, vegetation growth, cloudiness and wildfire, through divided the NHAF and SHAF into arid, intermediate, and mesic regions. The impact of fuel limitation and fire weather have been investigated in each region. The results of this study are detailed in chapter 4.

1.4 The wildfire's role in ecosystem

A fifth of the Earth's land surface is covered by savannas (Scholes, 2003) and the most of the biomass burning in Africa has been occurred over the savanna land (Giglio et al., 2013). In savanna ecosystems, an important feature is that the coexistence of trees and grasses, implying a transition between grasslands and forests. The classic ecological theory, which assumes that the distribution of the Earth's biomes is largely determined by 'climate envelopes', expects this transition is gradually with the gradually climate change alone the climate envelopes (Schimper, 1903). In other words, the tree cover rate in savannas is expected to display a continuous transit between grasslands and forests. However, the satellite observations show that under a range of the mean annual precipitation (MAP), there are two peaks of the tree cover rate: one in savanna (~20%) and one is forest (~80%) (Staver et al., 2011c; Verbesselt et al., 2016), implying the alternative states or the bistability (Hirota et al., 2011; Staver et al., 2011a).

Under this bistability, one important characteristic is the hysteresis. It means the tipping point of climate where savannas are convert to forest is higher than that where forest is convert to savanna, resulting in nonlinear and unstable transitions between the savannas and forests, rising the concerns about the global forest resilience (Hirota et al., 2011; Mayer and Khalyani, 2011). The local water availability is used to explain this nonlinear transition and coexistence. In a drier climate, the grasses overcome trees by stronger water absorption ability in the surface layer of the soil (Bond 2008; Higgins et al., 2012; Sankaran et al., 2004). In a wetter climate, the adult trees can growth stronger roots, which can reach to deeper water source than grass roots (Walter, 1971; Ward et al., 2013). But when MAP is in a certain range, between 1000~2000 mm enough precipitation to

support tree growth, the local water availability can not well explain the discontinuity of the tree cover ratio at continental scale (Sankaran et al., 2004).

Another important mechanism to explain the bistability is the feedback between wildfires and grasses (Staver et al., 2011c). The grasses due to its high flammability strengthen the wildfire spread and the intensity in the open canopy ecosystem. After fire, the grasses benefit from their faster recovery speed than the trees and the more open canopy resulted from the tree branch damages (Hoffmann et al., 2012). Also, fires suppress the savanna tree sapling growth and recruitment (Hanna, 2008). Thus, this forms a positive feedback between the fire and grasses to reinforce savanna formation and persistence where the climate condition could support forest development. One the other hand, when wildfires are absent or rare, the trees occupy more canopy space and limited the grasses light availability to suppress the grass growth. The seed spread and sapling tree recruitment also benefit from the low fire rate. Combined with the water availability, studies show at the low rainfall area, MAP 1000 mm, precipitation is the limitation and fire is less important, while in the mesic area, MAP greater than 1000 mm, the fire is more important to constrain the tree cover (Hirota et al., 2011; Staver et al., 2011c).

To describe this fire-vegetation feedback, a group of equations were established (Staver et al., 2011c; Staver and Levin, 2012). The *G, S, T* represent the grasses, savanna sapling trees,

$$\frac{dG}{dt} = \mu s + \nu T - \beta GT \tag{1.1}$$

$$\frac{dS}{dt} = \beta GT - \omega(G)S - \mu s \tag{1.2}$$

$$\frac{dT}{dt} = \omega(G)S - \nu T \tag{1.3}$$

and savanna adult trees. The $\frac{d}{dt}$ represents the object's change against time. This model is nonspatial but creates the limited space for the *G*, *S*, and *T* by holding the total area of *G*, *S* and *T* constant. The μ and ν is the death rate of the savanna sapling trees and the savanna adult trees. The β is the birth rate of the savanna trees saplings, which is a proportion of the *G* and *T*. The ω is the savanna sapling tree recruitment rate as a function of the grasses G. In equation (1.1), the change of the grasses is depends on the death of the savanna trees and saplings, μS and νT, respectively, as well as the birth of the new tree saplings (βGT). In equation (1.2), the savanna tree saplings change rate is depends on the its birth amount (βGT) subtracts its death amount (μs) and recruitment amount to the adult trees ($\omega(G)S$). The adult trees amount only be impacted by two factors, the recruitment amount from the sapling trees and its death amount, which is shown in equation (1.3).

The fire is not explicitly represented in the equations, but is implicitly represented in variable $\omega(G)$. Here the ω is defined as a sigmoidal function of *G*. In equation (1.4), the ω_1 and the ω_0 are two parameters represent the sapling tree recruitment rate when grasses dominant and the adult tree dominant in the certain domain. The shape of the function is shown in Fig. 1.1

$$\omega(G) = \omega_0 + \frac{\omega_1 - \omega_0}{1 + e^{-(G-\theta_1)/s_1}} \tag{1.4}$$

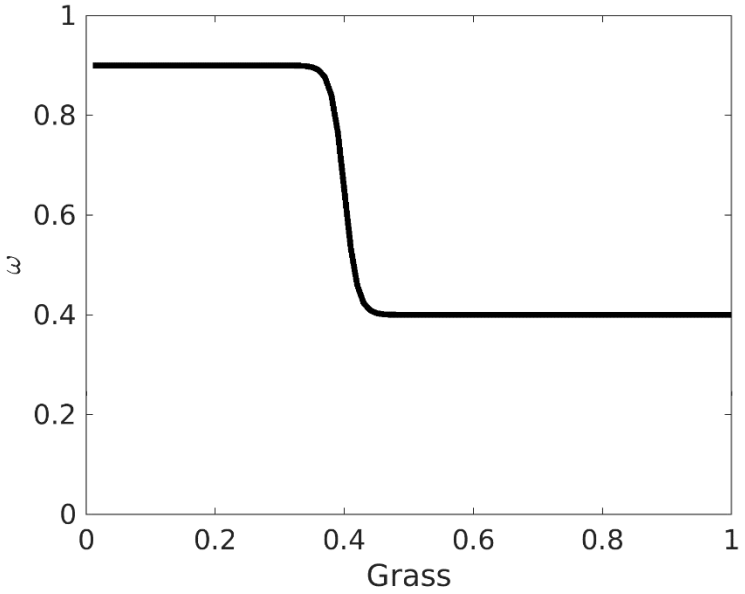

Figure 1. 1 The $\omega(G)$ function when the ω_0 is 0.9 and ω_1 is 0.4. The x axis is the grass fraction in the domain and the y axis is the value of the ω.

The ω is like the step-function shape with the maximum value in the low grass region and the minimum value in the high grass region. The ω setting based on two fundamental assumptions (Staver et al., 2011c). The fire spread in savannas depends on the abundance of the grass. There is a threshold of the fire spread, θ_1, which is 0.4 based on observation (Archibald et al. 2009). When *G* is less than this value, which is forest in most cases, the fire is almost nonexistent in the system. When *G* is greater than 0.4, the fire is sufficient. Although the fire rare kills adult trees and the tree saplings, it does impact the rate of the sapling tree recruitment (Higgins et al. 2000, Hoffmann et al. 2009). Therefore, the $\omega(G)$ can be looked as the fire's control in tree sapling recruitment, which is also controlled by the grass abundance.

Through solving the Jacobian matrix, the above equation set can give zero to two stable equilibrium solutions of *G*, *S* and *T* based on the parameter settings. One stable equilibria means only one state, either grassland or forest, is possible, while two equilibria means the bistability are possible. This suggests that the fire-vegetation feedback is enough to support the bistability situation mathematically in the mesic region, where water availability is not a limitation. The different parameter values, β, μ and ν, represent different climate conditions attractions, like pro-forest (more precipitation and less forest death) or pro-grass (less precipitation and higher forest death), giving the equations the potential to investigate the impact of the climate change to the landcover (forest vs. grassland).

Although there are progresses of understanding the savanna bistability and the fire-vegetation feedback, direct observation evidence in continental scale is absent to display the relationship between the fire activity and the forests growth. Only limited site studies show that the forests were enhanced when the local fire are suppressed in local scale (Kennan, 1972; Shackleton & Scholes, 2000; Tilman et al., 2000;). Moreover, the Staver-2011 ecosystem model is nonspatial and thus cannot represent the Africa landcover situation and the potential change in the future under climate change context. Studies show that the interactions between the land patches is important to represent the local savanna-forest condition (Staal et al., 2016; Wuyts et al., 2017). The patch spatial interactions include fire spread and tree seeding spread between the adjacent patches, resulting in the enhancement of the dominant state and accelerating the state change rate in the local savanna-forest boundary. Additionally, the unclear of the parameter values in the Staver-2011 model and the nature of the bifurcation characteristic of the equations increase the

complexity of this ecosystem model (Touboul et al., 2017). The last, because the fire is implicitly represented in the Staver-2011 model and described as a function of grass abundance, the model can not represent how the fire drive the landcover change, given the climate change context and dramatic shift of the fire regime in the Africa (Andela et al., 2017). The wildfire is not only depends on the grass fraction, but also depends on the climate factors and human activities (Andela and van der Werf, 2014b). Therefore, wildfires could be represented as a forcing to drive landcover change rather than an explicit disturbance in the model.

This part of thesis through analyzing the satellite-based wildfire and landcover data illustrates the new evidence that support negative fire-forest relationship in continental scale. It motivates the investigation, by using the ecosystem model that explicitly including the fire-forest feedback. The purpose of this research is to investigate the extent of the forest management (fire suppression) by which the forest growth could reach the RCP4.5 target in Africa by 2100. To reach the goal, we firstly modified the Staver-2011 model to convert it to be driven by fire forcing and apply it to Africa. To determine appropriate parameter sets, three experiments are designed with different model configuration. After obtained appropriate parameter values, we perform the model under different fire reduction scenarios to determine which scenario can best match the RCP4.5 forest pathway in Africa. The details of the model modifications and the results are described in Chapter 5.

CHARPTER 2. GLOBAL WILDFIRE PLUME HEIGHT DATASET AND PARAMETERIZATIONS FOR CLIMATE MODEL APPLICATIONS

2.1 The offline global plume height dataset

In this study, we calculated hourly global plume heights from 2002 to 2010, and the processes to determine a plume height are shown in Figure 1. The long-term fire information, including location, date and fire radiative power (FRP), obtained from MODIS MCD14ML product from 2001 to 2014 is used to determine the maximum fire radiative power (MFRP), which is month-, region- and PFT-specific. The FRP of an individual fire is used to calculate the total fire energy flux (*E*) via FRPx10 approach and to determine the fire size, through scaled-FRP approach with corresponding MFRP. Together, the total fire energy flux, fire size, and corresponding meteorology fields determine the plume height through performing the modified plume-rise model (**Fig. 2.1**). These processes are region- and PFT-specified. The region and the PFT partition and the meteorology data used in this study are introduced in section 2.1.1 and the methods for calculate the total fire energy and the fire size are documented in section 2.1.2. The 1D plume-rise model modification is detailed in section 2.1.3. In section 2.1.4, the method to calculate the plume diurnal cycle is introduced, and the MISR data and the AOD data used in this study are documented in section 2.1.5 and 2.1.6. To verify the impacts of the plume height, numerical experiments have been performed, the information about the design of the experiments and the model setup are described in section 2.1.7.

Meteorology data, fire regions, and plant functional types (PFTs)

To calculate a certain plume, this 1D model needs vertical meteorology fields, total fire heat flux, and the fire size (**Fig. 2.1**). In this study, the meteorology fields were from the Climate Forecast System Reanalysis (CFSR) hourly forecast data, with 0.5^{o} x 0.5^{o} horizontal resolution and 37 vertical layers, from 2002 to 2010 (Saha et al., 2014). We used four meteorology variables, the temperature, geopotential height, specific humidity and wind, in each layer from land surface to the top of troposphere. The reason of choosing hourly and high spatial resolution data is due to the strong sensitivity of plumes to atmospheric buoyance (Sofiev et al., 2012).

The 1D plume model used in this study is developed by Freitas et al., 2007 and 2010. These governing equations are based on first law of thermodynamics, vertical momentum flux, and continuity equation. The vertical turbulence equation is based on Simpson and Wiggert cloud convection scheme (Simpson and Wiggert, 1969). The dynamic codes is based on Latham (1994). For let it suit the fire plume calculation, the initial speed and temperature of air parcel is calculated first based on a virtual source of buoyancy placed below model surface (Turner, 1973; Latham, 1994). The top boundary is Rayleigh friction layer. In 2010, a horizontal wind entrainment option was added in (Freitas, 2010). The final height of the plume is determined as the height at which the vertical speed of air parcel is smaller than 1 m/s (Freitas et al., 2007).

There are fifteen wildfire regions used in this study (**Fig.2.2** and **Table 2.1**), which are based on GFED fourteen regions but separate the Temperate North America as Western (WTNA) and Eastern (ETNA) parts due to the distinguish wildfire characteristics between the Western and Eastern area.

In this study, 6 categories of PFTs are defined: needle leaf forest, broad leaf forest, shrub, grass, crop, and unvegetated. These PFTs which are simplified from the 16 MODIS landcover types from MODIS Landcover dataset MCD12Q1 in the IGBP Land Cover Type Classification (Channan et al., 2014) (**Table 2.2**). Using 6 categories of PFTs is to keep consistency with CLM 6 PFTs, which is also mainly derived from the MCD12Q1 IGBP Land Cover Type Classification since CLM 3.0 (Lawrence and Chase, 2007), because we also provide a plume-rise parameterization for the CESM online simulation besides the plume-rise dataset for CESM offline simulations. The spatial distribution of the 6 PFTs are shown in **Fig. 2.3**.

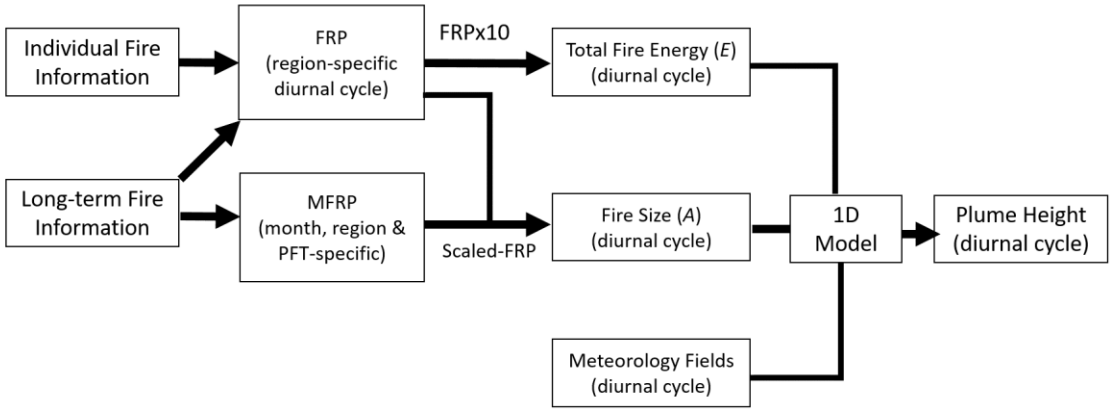

Figure 2. 1. The schematic of calculating the offline plume height dataset.

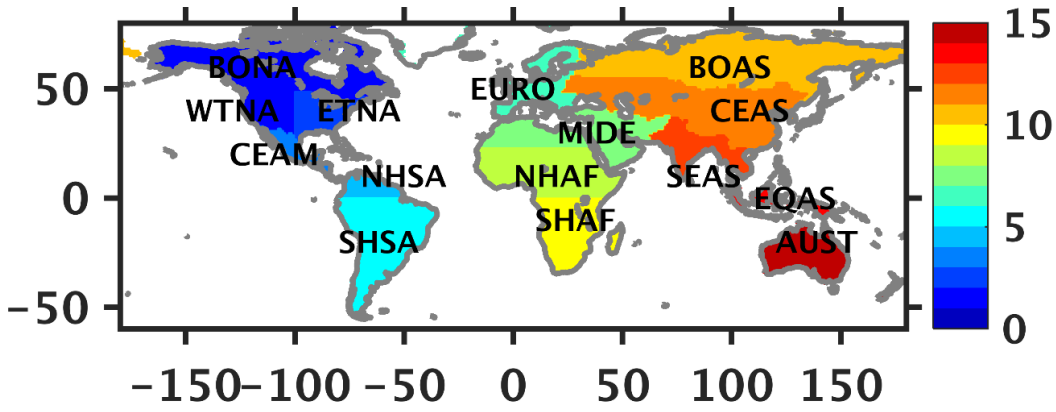

Figure 2. 2. The wildfire regions used in this study**.**

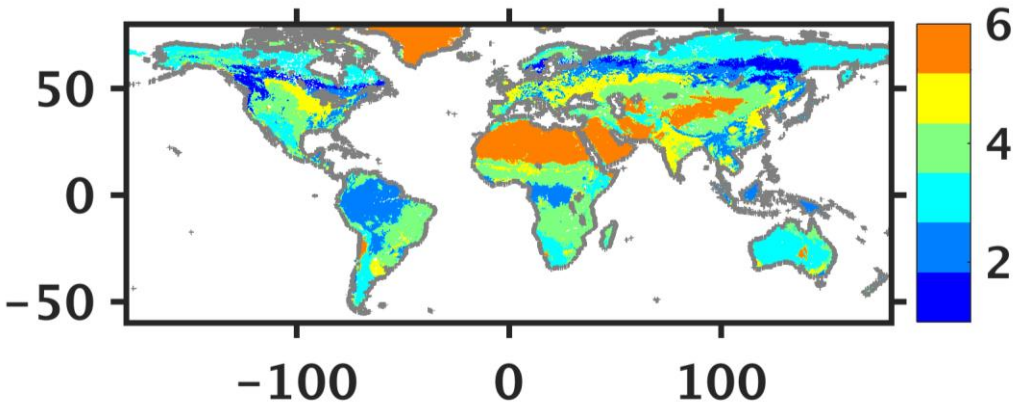

Figure 2. 3. The PFT spatial distribution used in this study. The information of the six PFTs are detailed in the Table 2.2

Table 2. 1. The definitions of 15 wildfire regions used in this study. The region partition is based on the GFED 14 wildfire regions but separates the Temperate North America (TNA) as Western (WTNA) and Eastern (ETNA) parts**.**

Abbrev.	**Short Name**	**Comments**
BONA	Boreal North America	Alaska and Canada.
WTNA	Western Temperate North America	Western Conterminous United States.
ETNA	Eastern Temperate North America	Eastern Conterminous United States.
CEAM	Central America	Mexico and Central America.
NHSA	Northern Hemisphere South America	Division with SHSA is at the Equator.
SHSA	Southern Hemisphere South America	Division with NHSA is at the Equator.
EURO	Europe	Includes the Baltic States but excluding White Russia and the Ukraine.
MIDE	Middle East	Africa north of the Tropic of Cancer, and the Middle East plus Afghanistan.
NHAF	Northern Hemisphere Africa	Africa between the Tropic of Cancer and the Equator.
SHAF	Southern Hemisphere Africa	
BOAS	Boreal Asia	Russia, excluding area south of 55 N between the Ukraine and Kazakhstan.
CEAS	Central Asia	Mongolia, China, Japan, and former USSR except Russia.
SEAS	Southeast Asia	Asia east of Afghanistan and south of China.
EQAS	Equatorial Asia	Malaysia, Indonesia, and Papua New Guinea.
AUST	Australia	Includes New Zealand.

Table 2. 2. The plant function types used in this study and the corresponding MODIS PFT.

Plant Function Type	MODIS 16 land cover code
Needle Tree	1, 3
Broad Leaf Tree	2,4,5
Shrub	6,7
Grass	8,9,10
Crop	12,13,14
Barren Land	15,16

Total fire energy flux and fire size

In this study, the total fire energy flux was determined by the FRP×10 approach and the fire size was determined by the scaled-FRP approach, because this combination performed the best estimation of the plume heights over North America compared to other 15 combinations of approaches (Val Martin et al., 2012). The information about detected fires including locations, date and FRPs was obtained from the MODIS MCD14ML Global Monthly Fire Location Product (Giglio, 2013). Although both Terra and Aqua data provide active fire product, only Terra product have been processed for plume height calculation to avoid the reduplicative counting of detected fires.

By using the scaled-FRP approach to determine the fire size, an individual fire size is calculated as equation (2.1),

$$A = \Delta r * FRP/MFRP \qquad (2.1)$$

in which, Δr is the resolution of the detected fire, and it is *1 km*^{2}. The *FRP* is the fire radiative energy of an individual fire detected by MODIS with unit of *MW/ km*^{2}, and the *MFRP* is the Maximum FRP (MFRP), which is the 99th percentile value of ever detected *FRP* for a certain wildfire region, plant functional type and calendar month from 2001 to 2014. We assume the *MFRP* represents the *FRP* released under completed burning condition over the *1 km*^{2} area. The values of MFRP are documented in Table S3, with unit of *MW/ km*^{2}. The ratio of FRP to MFRP represents the burn fraction of this area. Therefore, the unit of the fire size *A* is *km*^{2}. If detected wildfire hotspots are next to each other (the distance less than 1.1 km), these fires are aggregated into a big fire. The fire with strongest

FRP is chosen as the primary fire and the FRPs of other smaller fires are added into this primary fire's FRP. In this way, a new aggregated fire hotspot is produced with the primary fire's location (latitude and longitude) and aggregated FRP. The aggregation process is similar as described in other studies (Kahn et al., 2007; Val Martin et al., 2009).

For determining total fire energy flux, the FRPx10 approach was applied to each detected fire. Previous studies determined that the satellite detected fire radiative energy is about 12-14% of total fire energy (Freeborn et al., 2008; Wooster et al., 2005). Thus, it is reasonable to assume the total fire energy flux as the detected fire radiative energy flux multiplies ten, shown as equation (2.2).

$$E = 10 * FRP \tag{2.2}$$

in which, the *E* stands for the total fire energy flux with unit *MW*, and the *FRP* is same as defined in equation (2.1) but the unit switches to *MW*. The FRPx10 and scaled-FRP both used the data derived from MODIS MCD14ML product to keep the data consistency.

In summary, the long-term fire information, including location, date and FRP, obtained from MODIS MCD14ML product from 2001 to 2010 is used to determine the MFRP, which is month-, region- and PFT-specific. The FRP of an individual fire is used to calculate the total fire energy flux (*E*) via FRPx10 approach and to determine the fire size, through scaled-FRP approach with corresponding MFRP. Together, the total fire energy flux, fire size, and corresponding meteorology fields determine the plume height through performing the modified plume-rise model. The schematic of the processes is summarized in **Fig. 2.1**.

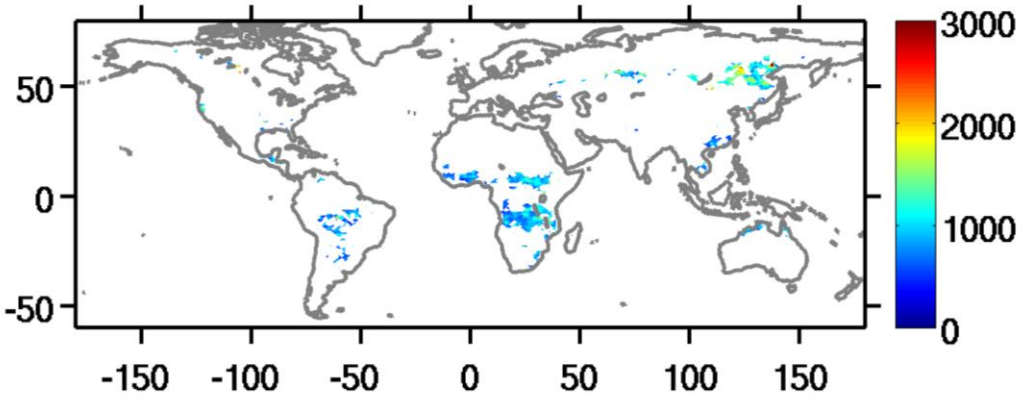

Figure 2. 4. The plume heights of MISR plume height project 2. The plume heights shown are the plumes with 'good' quality flag**.**

1-D model modification

We applied the 1-D plume-rise model developed by Freitas et al. (Freitas et al., 2006, 2010) in this study. This model has a physical plume-rise scheme, which is governed by conservation of energy, vertical momentum, and mass. It was previously used in regional air quality and climate models (Grell et al., 2011; Pfister et al., 2011; Stein et al., 2009). The vertical momentum flux in the model was computed as (Freitas et al., 2007),

$$\frac{\partial w}{\partial t} + w\frac{\partial w}{\partial z} = \frac{1}{1+\gamma} gB - \frac{2\alpha}{R} w^2 + \frac{\partial}{\partial z}\left(K_{zz}\frac{\partial w}{\partial z}\right) \quad (2.3)$$

where w is the vertical velocity, t is the time, z is the vertical movement, g is the acceleration due to gravity, and γ is the parameter to compensate for the neglect of non-hydrostatic pressure perturbations and was set to be 0.5 in this study (Simpson and Wiggert, 1969). The B is the buoyance term related to the difference of temperature between plume air parcel and its environment. The $\frac{2\alpha}{R}$ is the traditional entrainment coefficient, where $\alpha = 0.1$ and R is the radius of the plume air parcel. The eddy viscosity term, K_{zz}, was set as a constant in original model. However, the K_{zz} is a term varying with altitude. In this study, we rewrote eddy viscosity term as

$$\frac{\partial}{\partial z}\left(K_{zz}\frac{\partial w}{\partial z}\right) = K_{zz}\frac{\partial^2 w}{\partial z^2} + \frac{\partial K_{zz}}{\partial z}\left(\frac{\partial w}{\partial z}\right) \tag{2.4}$$

In equation (2.4), the $\frac{\partial K_{zz}}{\partial z}\left(\frac{\partial w}{\partial z}\right)$ term is an extra term compared to original model setting due to taking the change of K_{zz} with altitude into consideration. We set the K_{zz} values as a parabolic curve, which is increasing from surface, reaching the peak in the middle of the boundary layer and decreasing to small value at the top of boundary layer as described in (Lamb and Durran, 1978). While the peak K_{zz} value is as same as the default K_{zz} value (500 $kgs^{-1}m^{-1}$) in 1D plume-rise model, its value decrease gradually to 1 at the surface and the top of the boundary layer height, which is 2000 meters vertically. As the $\frac{\partial w}{\partial z}$ is a negative term when plume is raising, the $\frac{\partial K_{zz}}{\partial z}\left(\frac{\partial w}{\partial z}\right)$ becomes negative when K_{zz} is increasing with altitude (first half of boundary layer) while $\frac{\partial K_{zz}}{\partial z}\left(\frac{\partial w}{\partial z}\right)$ becomes positive when K_{zz} is decreasing with altitude (second half of boundary layer). The negative term of $\frac{\partial K_{zz}}{\partial z}\left(\frac{\partial w}{\partial z}\right)$ in first 1000 m suppresses the w and confines the small fire plumes in the first 1000 m. This feature helps confine the tropical grass fire plumes in reasonable range. On

the other side, the positive term of $\frac{\partial K_{zz}}{\partial z}\left(\frac{\partial w}{\partial z}\right)$ enhances the w and promotes the big fire plumes in the second 1000 m. This effect of lifting w in the second half of boundary layer could increase the final plume height to solve the issue that the model underestimated the plume heights of forest fires mentioned in previous studies (Freitas et al., 2010; Val Martin et al., 2012). In this study, the boundary layer height is fixed to avoid the discrepancy of boundary layer height from different meteorology dataset due to their different definitions (Val Martin et al., 2012). Moreover, as the K_{zz} is also a function of surface temperature, we set the K_{zz} has apeak value 500 $kgs^{-1}m^{-1}$ in tropics (30^0 S to 30^0 N) and gradually reduce to 300 at north and south poles. The other details about the 1D plume-rise model is described in supplementary materials.

The diurnal cycle of plume

Above sections introduce the method to calculate the plume height when MODIS Terra satellite overpasses, while this section describe the method to calculate the plume height with diurnal cycle. For this purpose, the hourly meteorology fields are used, which are from CFSR 1-hr dataset, because the plume height is sensitive to the stability in atmosphere, especially the stability within the planetary boundary layer (Sofiev et al., 2012; Val Martin et al., 2012). Besides the diurnal variability in atmosphere, the wildfire also has diurnal variability (Mu et al., 2011) that could be parameterized by a modified Gaussian Function according to Ellicott et al., 2009 and Vermote et al., 2009, shown in equation (2.5),

$$FRP(t) = FRP_{peak} * (b + e^{\frac{-(t-h)^2}{2\sigma^2}}) \quad (2.5)$$

where the *FRP* is a function of time and the unit of the time is hour. The FRP_{peak} is peak *FRP* value during a day, which usually happens in the afternoon. The *h* is the time when FRP_{peak} occurs and the *b* provides a background *FRP*, which is a constant. This is important during the night. The σ is standard deviation of this curve. According to Vermote et al. (2009), the *h*, *b* and δ can be wrote as the function of Terra-to-Aqua FRP (T/A) ratios, *r*, shown as equation (6) to (9).

$$h = -1.23r + 14.57 \tag{2.6}$$

$$\delta = 3.89r + 1.03 \tag{2.7}$$

$$b = 0.86r^2 - 0.52r + 0.08 \tag{2.8}$$

$$r = FRP_{terra}/FRP_{aqua} \tag{2.9}$$

The *r* is a region-specific T/A ratio from 2001 to 2014 for the 15 regions described above. As the MODIS MCD14ML products provide the location, detected time, and FRP for the fire spots, the FRP_{terra} is the determined as the accumulated FRP detected by satellite Terra around local time 10:30 for a certain region from 2001 to 2014 and the FRP_{aqua} is calculated as the accumulated FRP detected by satellite Aqua around local time 13:30 for a certain region from 2001 to 2014. Here we filtered out the FRP values that were detected at other times of a day (in the night for most of the cases) to satisfy the assumption in Vermote et al. (2009) that assuming the Terra and Aqua overpass time were 10:30 and 13:30 respectively for fitting the Gaussian curve. This is an update compare to Vermote et al. 2009, in which the daytime and nighttime *FRP*s have not been separate as they used the MODIS monthly climate modeling gridded *FRP*.

After calculated the *r, b,* δ and *h* for a certain region, the FRP_{peak} of a detected fire spot were determined by equation (2.10),

$$FRP_{peak} = FRP_T/(b + e^{\frac{-(t_T-h)^2}{2\sigma^2}}) \quad (10)$$

where the FRP_T is the FRP detected by MODIS Terra satellite and the t_T is the Terra overpass time during the daytime, which is given by MODIS MCD14ML products. By substituting the *b,* δ and *h* values for a certain region, the FRP_{peak} for an individual fire hotspot was determined. Through substitute FRP_{peak}, *b,* δ and *h* values into equation (2.5) the FRP values at different local time were determined. The parameter values of *b,* δ and *h* are documented in **Table 2.3** and the typical curves of diurnal cycles of each region are shown in **Fig.2.5**. To get the typical diurnal cycle for each region, we calculate the MFRP diurnal cycle instead of the FRP. We use the equation (2.10) and the parameters *r*, *h, b* and δ to determine the $MFRP_{peak}$, by assuming the MFRP value is observed at the 11:00 local time. Then by substituting the $MFRP_{peak}$, *r, h, b* and δ into equation (2.5), the MFRP value as a function of time can be determined. The typical MFRP cycle are shown in **Fig. 2.5**.

Through substituting *FRP(t)* determined by equation (2.5) into equation (2.3) and (2.4), the fire size, *A(t),* and total fire energy, *E*(t), both as a function of local time were determined. Combined the *A(t)* and *E(t)* with hourly meteorology fields from CFSR, the diurnal variations of plume heights were calculated (**Fig. 2.1**). The results suggested that a higher penetration rate to planetary boundary layer (more than 50%) can be expected in the late afternoon, as the effects of both meteorology and fire diurnal variability (shown in section 2.2).

Table 2. 3. The parameter values used in calculate the FRP diurnal cycles in different regions

	FRP peak	b	h	sigma
BONA	**18.948**	**0.048**	**13.911**	**3.113**
WTNA	**15.525**	**0.023**	**14.002**	**2.826**
ETNA	**4.184**	**0.095**	**13.792**	**3.489**
CEAM	**9.281**	**0.020**	**14.015**	**2.785**
NHSA	**5.347**	**0.007**	**14.097**	**2.527**
SHSA	**121.811**	**0.003**	**14.253**	**2.033**
EURO	**3.409**	**0.020**	**14.015**	**2.785**
MIDE	**2.379**	**0.063**	**13.870**	**3.243**
NHAF	**127.548**	**0.003**	**14.153**	**2.348**
SHAF	**196.897**	**0.006**	**14.289**	**1.920**
BOAS	**31.544**	**0.049**	**13.908**	**3.123**
CEAS	**18.347**	**0.116**	**13.748**	**3.629**
SEAS	**71.898**	**0.029**	**14.417**	**1.513**
EQAS	**7.399**	**0.010**	**14.318**	**1.827**
AUST	**38.804**	**0.106**	**13.769**	**3.564**

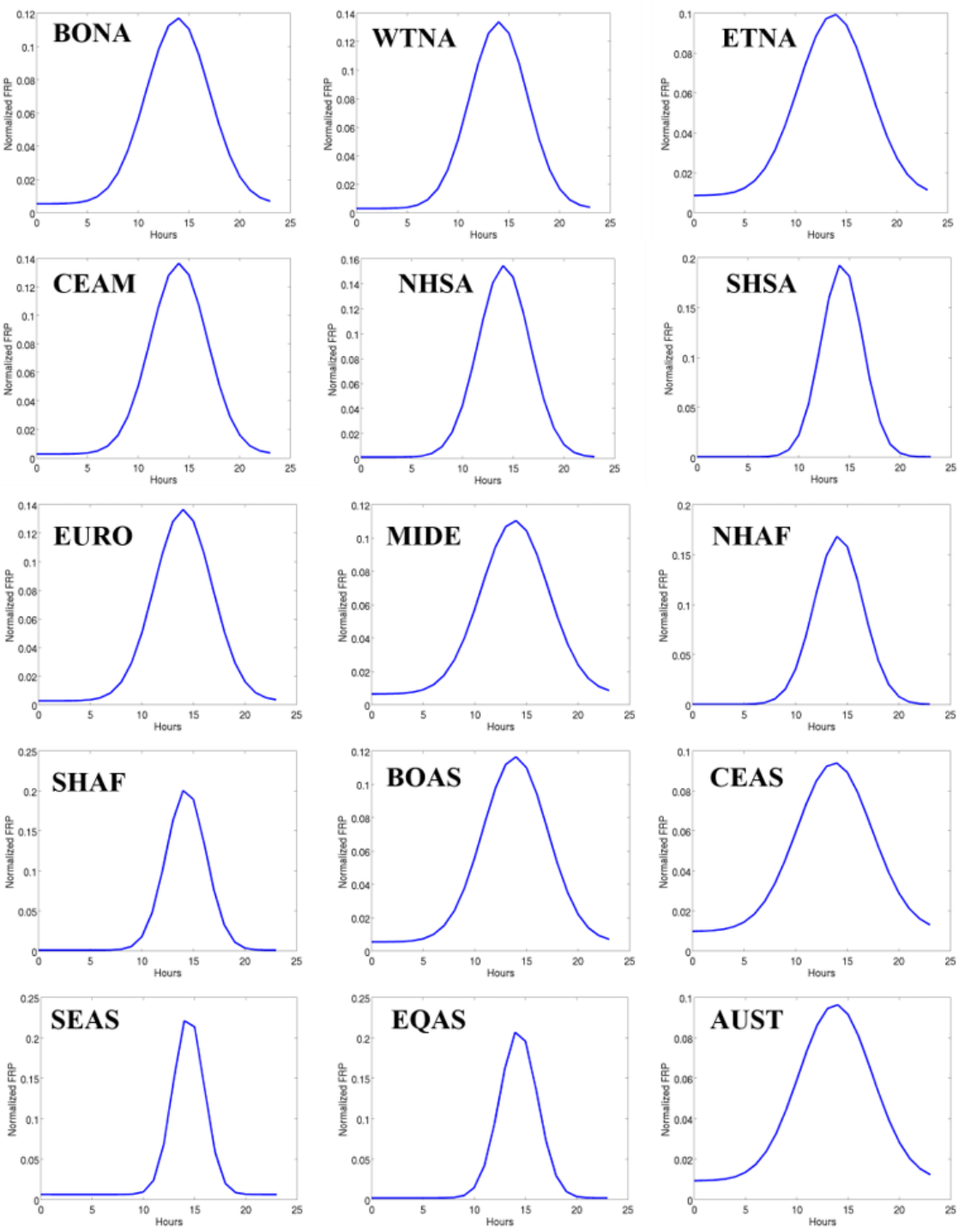

Figure 2. 5. The normalized MFRP diurnal cycles for 15 regions. The x-axis is local time and the y-axis is the amplitudes**.**

MISR plume heights

For evaluation purpose, the plume heights from the MISR plume height project have been used as reference (Kahn et al., 2008; Val Martin et al., 2009). This product includes plumes from 2002 to 2009 over eight regions, Africa, Alaska, Canada, Indonesia, North America, Siberia, South America, and Southeast Asia. The data availability for different regions within different years is summarized in Table S4. In this study, we choose plumes with 'good' quality tag and use the maximum plume height as the plume height, because the 1D plume-rise model gives the plume top height. Therefore, there are 7843 plumes out of 11770 are choose as reference, and their heights are shown in Figure 3b. In general, the plume heights are higher in high latitudes and lower in low latitudes. Although the MISR plume height project 2 data are available since 2015, this dataset has limited 'good' quality plumes and has the similar features as previous data (Fig.2.6). Therefore, this study uses the MISR plume height project product. (see http://misr.jpl.nasa.gov/getData/ accessData/MisrMinxPlumes/ for details)

As MISR and MODIS are both onboard Terra satellite, the fires caused MISR plumes are also recorded by MODIS. For each MISR plume, we obtain the corresponding fire information, including location, time, FRP, from MCD14ML product and then calculate the corresponding plume heights by inputting fire size, total fire energy flux, and meteorology fields into modified 1D plume-rise model as described in previous sections. The comparison between the model plume heights and MISR plume heights is in section 2.2, and is shown in **Fig.2.**.

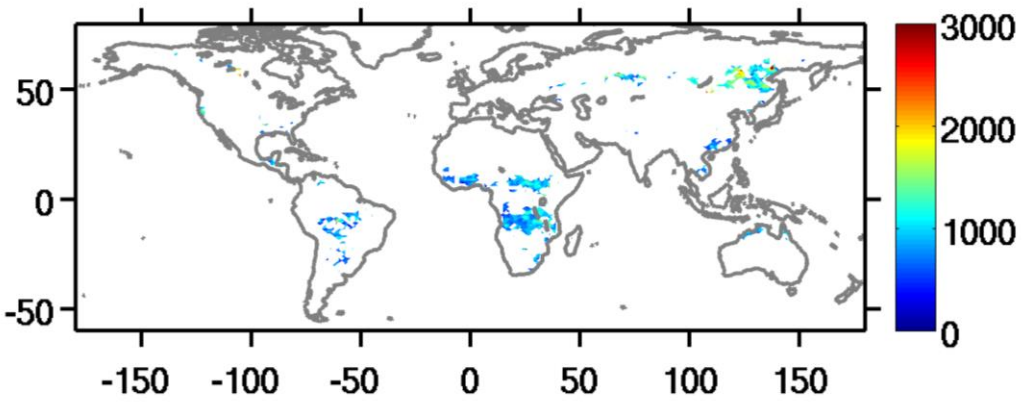

Figure 2. 6. The plume heights of MISR plume height project 2. The plume heights shown are the plumes with 'good' quality flag**.**

The AOD data

The Cloud-Aerosol Lidar and Infrared Pathfinder Satellite observations (CALIPSO) provides multiyear global dataset of lidar aerosol and cloud profiles with six identified aerosol types: clean marine, dust, polluted continental, clean continental, polluted dust, and smoke, through Cloud-Aerosol Lidar with Orthogonal Polarization (CALIOP) instrument onboard the CALIPSO satellite of the NASA A-Train (Winker et al., 2010). Study compared CALIPSO AOD with AERONET AOD at 147 AERONET sties and suggested that there was a lower bias of 13% compared to AERONET AOD for entire dataset that was mainly due the assumed lidar ratio (40 sr) is too low (Schuster et al., 2012). However, the two major biased regions are Sahara and Northwest China due to dust, where biomass burning were not significant. Importantly, the CALIPSO AOD was more sensitive to biomass burning region, such as South Africa and South America, compared to MODIS AOD products, while the former's spatial distribution and seasonal variability was generally comparably to MODIS AOD (Ma et al., 2013). In this study, we use the CALIPSO lidar level 3 all-sky daytime aerosol data product, which provides the monthly

mean AOD associated with dust and smoke in a 2^o x 5^o resolution, latitude and longitude respectively.

The climate mode experiment

In this study, we use the Community Earth System Model (CESM) version 1.2, with the community atmosphere model version 5 (CAM5) (Neale et al., 2012) coupled with community land model version 4 (CLM4) (Oleson et al., 2010). The 3-mode Modal Aerosol Model (MAM3) is included in CAM5 to simulate the aerosol lifecycle (Liu et al., 2012). In the MAM3, the aerosol mass and number mixing ratio are included in three lognormal modes: Aitken, accumulation, and course mode. Particularly, the BC and primary organic matter (POM) from both wildfires and anthropogenic sources are emitted into accumulation mode in the MAM3 and immediately mixed with any hygroscopic species in this mode.

Three Community Atmosphere Model 5.0 (CAM5) experiments are designed: the control run (NO-Smk), the surface smoke run (Srf-Smk), and the plume smoke run (Plm-Smk). The control run including all emissions but not the wildfire emission. The surface smoke run includes wildfire emission but releases it at the surface level. The plume smoke run releases the wildfire emission at the plume height defined by our plume height dataset. The settings are summarized in **Table 2.4**. The wildfire emission used in the study is Global Fire Emission Database with small fires (GFED4s) (Randerson et al., 2012), which has 0.5^o x 0.5^o degree spatial resolution and 3-hour temporal resolution from 1997 to present. In the surface smoke run, the GFED4s emissions were released on the surface. The typical

distribution of emission release levels in January and July are shown in Fig?. In January, the major burns happen in the South Hemisphere, especially the South America and Southern Africa. The PFT2, PFT3, and PFT4 are the typical PFT in these areas. In the afternoon, the south hemisphere emissions are released aloft mainly between 1500m to 4000m (**Fig. 2.7**). In July, the major burns move to the North Hemisphere, especially the Northern Africa, southeast Asia, Siberia and Canada. The PFT1, PFT2, and PFT4 are main plant function types in these areas. The emissions are released heights mainly between 500m and 3500m (**Fig. 2.8**). The model runs from 2006.01 to 2010.12, because the CLIPSO AOD available since 2006. The all model runs constrained by GEOS5 meteorology data.

The CAM5 model outputs includes the monthly AOD. The AOD difference between plume smoke run and control run are used to evaluate the impact of wildfire on global AOD. The difference between plume smoke run AOD and surface smoke run AOD are used to evaluate the contribution from the plume heights. The results are shown in section 2.3.

Table 2. 4. The design of the numerical experiments.

Experiment Name	Fire Emission	Other Emission	Plume Height	Data Availability
NO-Smk	Off	On	Off	2006~10
Srf-Smk	On	On	Surface	2006~10
Plm-Smk	On	On	Defined	2006~10

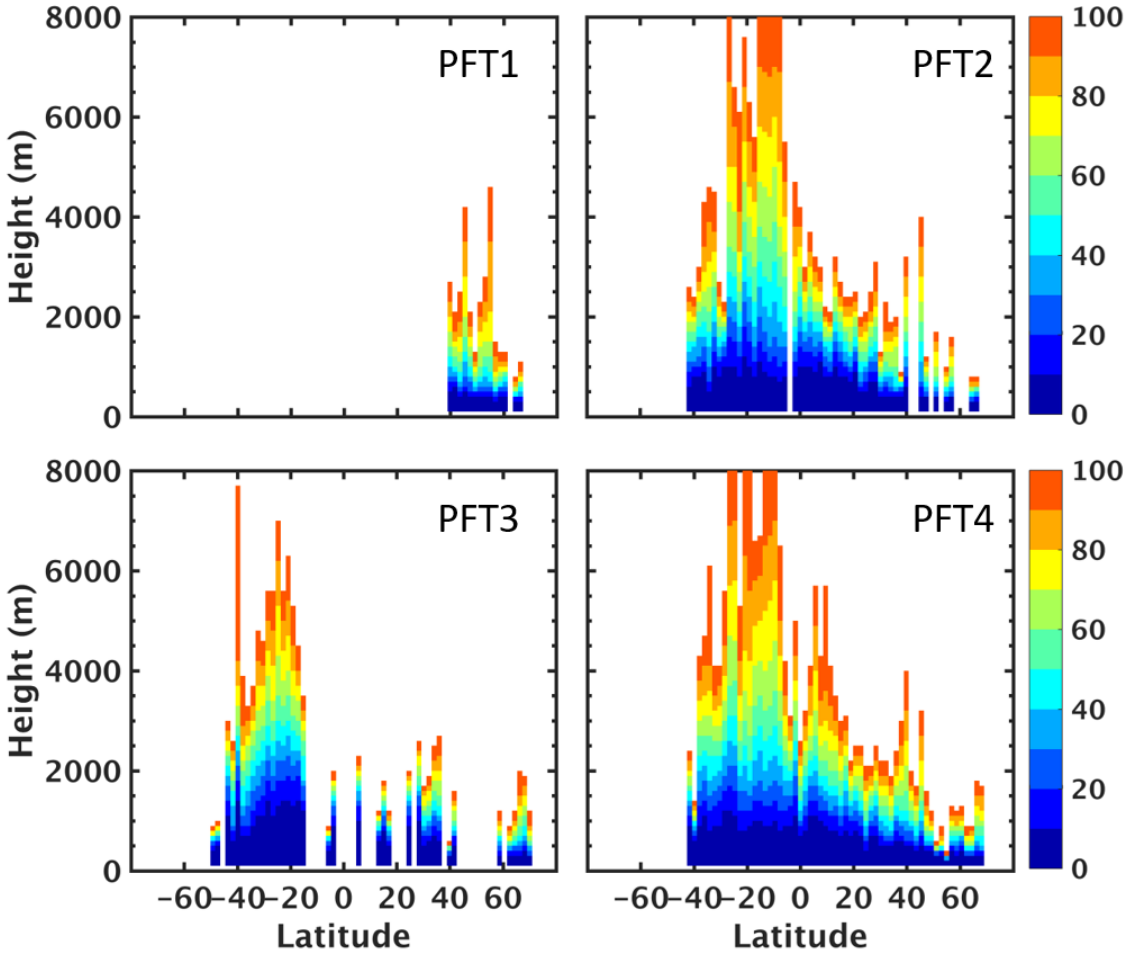

Figure 2. 7. The zonal mean emission distribution in January during 2002 to 2010. The shown distribution is the cumulative distribution from the surface to the top of the plume. The color shading shows the percentage for each 100-meter interval**.**

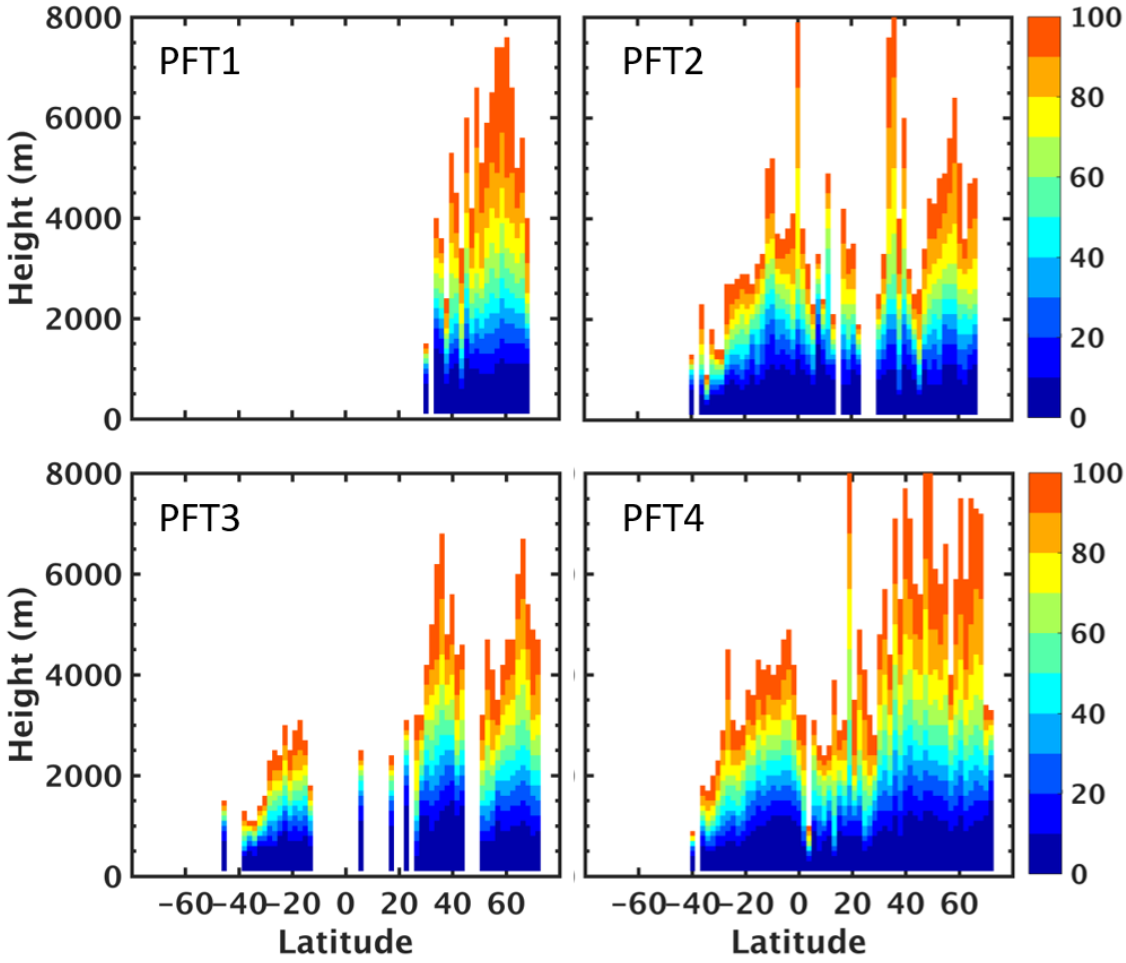

Figure 2. 8. Same as the Fig.2.7 but for July

2.2 Online parameterization of fire plume height in a climate model

For simulate the plume heights in climate model online runs, this study developed a plume-rise implementation for CESM. The online runs here defined as model runs by coupling the CAM5 with climate land model (CLM) 4.5 in community earth system model (CESM 1.2.2). This implementation includes a simplified region- and PFT-specified plume-rise parameterization scheme and a cumulative distribution function (CDF)

mapping scheme, shown in Figure 2. For the plume-rise parameterization scheme, we applied the linear regression between MISR plume heights and wildfire and meteorology parameters and then simplified it through Stepwise method. To obtain better plume-rise output, the CESM online inputs were prepared by the CDF mapping scheme. The most calculation are processed in CAM5 but requires the wildfire information from CLM 4.5 (Zou et al., 2017). The details about the two schemes are described as following

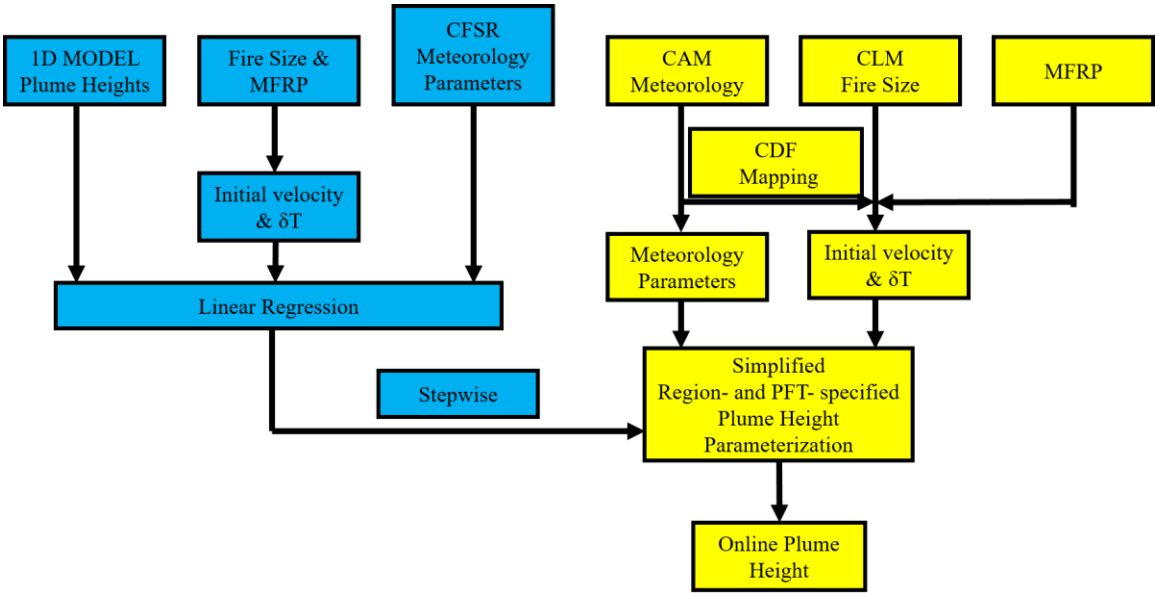

Figure 2. 9. The schematic of the CAM5 plume-rise implementation. The boxes filled with blue color represent the processes to develop the plume height parameterization off-line, while the boxes filled with yellow color represent ones to generate the on-line plume heights

the plume-rise parameterization

For CESM online runs, in which the atmosphere model couples with land model, the wildfires are generated from land model at each timestep andf that calculating the plume height through the 1D plume-rise model embedded in atmosphere model is not computing efficient (Val Martin et al., 2012). Therefore, this study developed an implementation for

CESM to calculate the plume height based on the fire information from the land model and the meteorology information from the atmospheric model. The schematic is shown in **Fig.2.9**.

Firstly, a simplified region- and PFT-specified plume height parameterization has been developed. The parameterization is based on linear regression model, finding the relationship between the our long-term 1D model plume heights and the fire and meteorology parameters, and is simplified though the Stepwise method to improve the computing efficiency (**Fig.2.9**. blue part). We keep the same 15 wildfire regions and 6 plant function types, as described previous (**Fig.2.2** and **2.3**). The plume heights calculated by 1D plume-rise model for the hotspots with at least 95 confidence level marked by MODIS from 2002 to 2010 are collected, as well as the fire parameters and the meteorology parameters. Here the fire parameters refer to the initial plume velocity and temperature difference between fire and ambient air, which are the bottom boundary condition in 1D plume-rise model and are calculated by assuming a virtual source of buoyancy placed below model surface (Latham, 1994; Turner, 1979). The fire size, MFRP, surface air temperature, and surface pressure are needed inputs to calculate the initial velocity and the temperature difference. The initial velocity is the most important parameter for this parameterization because it has best relationship with plume heights (**Fig. 2.10**) compared to other parameters, especially the FRP, which was considered as the most important parameter in previous study (e.g., Doherty et al., 2013; Sofiev et al., 2012; Val Martin et al., 2012). For a better regression result, besides the initial velocity and temperature difference we also considered another 25 parameters: the planetary boundary layer height (1 parameter), the vertically potential temperature difference for every 500 meters interval

from surface to 6000 m high (12 parameters), the horizontal wind speed for every 500 meters interval vertically from surface to 3000 meters (6 parameters), and the specific humidity in same layer as wind speed (6 parameters). Including the constant term, 28 terms were applied in the linear regression process for a certain fire region and plant function type. By using 'Stepwise' method in MATLAB with the 0.01 threshold, the number of effective parameters are reduced from 28 to less than 9. The selected parameters for a certain region and PFT are shown in Table 2.5 and the corresponding coefficients of the parameters are shown in Table 2.6. For a certain region and PFT without enough plume heights to conduct the linear regression, it is filled with the values from the closest region and PFT. The verification is shown in section 2.3.2.

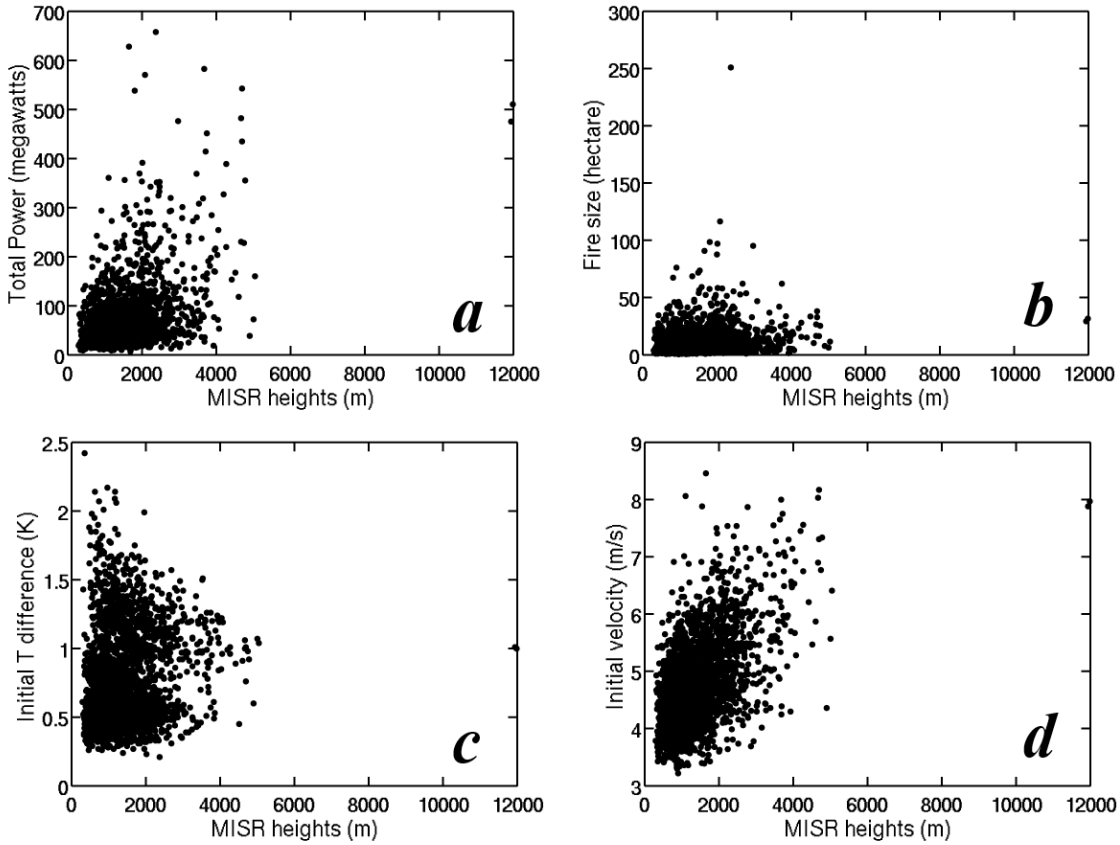

Figure 2. 10. The sensitivity of MISR plume heights to parameters. Panel *a* is the sensitivity to FRP, panel *b* is to fire size, panel *c* is for initial temperature and panel *d* is for initial velocity**.**

Table 2. 5. The terms used in parameterization. The first column is the region, and the second column is the PFT. The third to tenth column are the selected term by the Stepwise method. The values 1 is the plume velocity, the value 2 is the plume temperature difference, the value 3 is the PBLH, the value 4 to 15 is the potential temperature difference at layer 1 to 12, the value 16 to 21 is the wind speed at layer 1 to 6, the value 22 to 27 is the specific humidity at layer 1 to 6.

Region	PFT	term1	term2	term3	term4	term5	term6	term7	term8
1	1	1	2	3	5	6	16	20	0
1	2	1	3	0	0	0	0	0	0
1	3	1	3	5	6	19	0	0	0
1	4	1	2	3	4	5	6	8	9
1	5	0	0	0	0	0	0	0	0
1	6	0	0	0	0	0	0	0	0
2	1	1	3	5	8	21	0	0	0
2	2	5	0	0	0	0	0	0	0
2	3	1	3	5	12	0	0	0	0
2	4	1	3	5	10	0	0	0	0
2	5	3	5	8	0	0	0	0	0
2	6	0	0	0	0	0	0	0	0

Table 2.5 continued

3	1	0	0	0	0	0	0	0	0
3	2	1	3	4	7	8	10	16	0
3	3	5	0	0	0	0	0	0	0
3	4	1	3	4	5	7	8	0	0
3	5	1	3	4	5	7	8	16	0
3	6	0	0	0	0	0	0	0	0
4	1	0	0	0	0	0	0	0	0
4	2	1	4	5	0	0	0	0	0
4	3	0	0	0	0	0	0	0	0
4	4	1	3	4	5	6	8	20	0
4	5	1	4	5	6	8	0	0	0
4	6	0	0	0	0	0	0	0	0

Table 2.5 continued

5	1	0	0	0	0	0	0	0	0
5	2	1	3	4	5	7	18	0	0
5	3	1	3	4	5	7	16	17	20
5	4	1	2	3	4	5	7	22	24
5	5	1	4	5	0	0	0	0	0
5	6	0	0	0	0	0	0	0	0
6	1	0	0	0	0	0	0	0	0
6	2	0	0	0	0	0	0	0	0
6	3	0	0	0	0	0	0	0	0
6	4	1	3	5	8	0	0	0	0
6	5	1	3	8	0	0	0	0	0
6	6	0	0	0	0	0	0	0	0

Table 2.5 continued

7	1	0	0	0	0	0	0	0	0
7	2	0	0	0	0	0	0	0	0
7	3	1	3	4	8	0	0	0	0
7	4	0	0	0	0	0	0	0	0
7	5	1	3	4	8	0	0	0	0
7	6	1	4	0	0	0	0	0	0
8	1	0	0	0	0	0	0	0	0
8	2	0	0	0	0	0	0	0	0
8	3	0	0	0	0	0	0	0	0
8	4	0	0	0	0	0	0	0	0
8	5	0	0	0	0	0	0	0	0
8	6	0	0	0	0	0	0	0	0

Table 2.5 continued

9	1	0	0	0	0	0	0	0	0
9	2	0	0	0	0	0	0	0	0
9	3	4	5	0	0	0	0	0	0
9	4	1	4	5	8	0	0	0	0
9	5	0	0	0	0	0	0	0	0
9	6	0	0	0	0	0	0	0	0
10	1	3	9	0	0	0	0	0	0
10	2	1	3	9	0	0	0	0	0
10	3	1	3	4	5	7	8	12	18
10	4	1	3	4	9	0	0	0	0
10	5	3	0	0	0	0	0	0	0
10	6	0	0	0	0	0	0	0	0

Table 2.5 continued

11	1	0	0	0	0	0	0	0	0
11	2	1	3	4	0	0	0	0	0
11	3	1	6	9	0	0	0	0	0
11	4	1	3	4	5	9	10	15	0
11	5	1	3	4	8	0	0	0	0
11	6	0	0	0	0	0	0	0	0
12	1	0	0	0	0	0	0	0	0
12	2	0	0	0	0	0	0	0	0
12	3	0	0	0	0	0	0	0	0
12	4	0	0	0	0	0	0	0	0
12	5	0	0	0	0	0	0	0	0
12	6	0	0	0	0	0	0	0	0

Table 2.5 continued

13	1	0	0	0	0	0	0	0	0
13	2	1	4	5	0	0	0	0	0
13	3	0	0	0	0	0	0	0	0
13	4	0	0	0	0	0	0	0	0
13	5	0	0	0	0	0	0	0	0
13	6	0	0	0	0	0	0	0	0
14	1	0	0	0	0	0	0	0	0
14	2	5	0	0	0	0	0	0	0
14	3	1	4	5	6	8	14	18	26
14	4	1	3	4	5	6	7	26	0
14	5	0	0	0	0	0	0	0	0
14	6	0	0	0	0	0	0	0	0

Table 2.5 continued

15	1	0	0	0	0	0	0	0	0
15	2	1	3	4	7	0	0	0	0
15	3	0	0	0	0	0	0	0	0
15	4	1	3	4	7	0	0	0	0
15	5	1	3	7	0	0	0	0	0
15	6	0	0	0	0	0	0	0	0

Table 2. 6. The coefficients for all terms shown in table 2.5

Region	PFT	constant	term1	term2	term3	term4	term5	term6	term7	term8
1	1	622.532	90.745	-256.684	0.544	-65.249	-36.755	5.773	-5.838	0
1	2	-449.586	117.175	0.768	0	0	0	0	0	0
1	3	192.344	111.241	0.603	-57.142	-31.937	-1.471	0	0	0
1	4	152.818	95.285	-142.076	0.658	-27.352	-47.931	-29.251	17.685	28.892
1	5	0	0	0	0	0	0	0	0	0
1	6	0	0	0	0	0	0	0	0	0
2	1	72.335	80.075	0.462	-37.566	58.233	-1.875	0	0	0
2	2	1449.156	-84.2	0	0	0	0	0	0	0
2	3	931.457	65.761	0.202	-633.539	62.715	0	0	0	0
2	4	-54.223	99.975	0.367	-96.396	100.054	0	0	0	0
2	5	540.655	0.401	-54.292	74.803	0	0	0	0	0
2	6	0	0	0	0	0	0	0	0	0

Table 2.6 continued

3	1	0	0	0	0	0	0	0	0	0
3	2	-690.833	124.432	0.422	-81.618	38.835	41.66	31.667	3.967	0
3	3	1669.718	-150.90	0	0	0	0	0	0	0
3	4	-305.543	147.901	0.345	-154.50	-48.774	28.748	33.488	0	0
3	5	-226.98	124.95	0.303	-98.579	-27.371	35.313	23.251	3.151	0
3	6	0	0	0	0	0	0	0	0	0
4	1	0	0	0	0	0	0	0	0	0
4	2	778.797	101.112	-164.17	-140.65	0	0	0	0	0
4	3	0	0	0	0	0	0	0	0	0
4	4	320.716	135.451	0.235	-75.349	-60.866	-69.426	55.974	-1.906	0
4	5	932.271	83.681	-170.04	-211.23	-52.761	50.31	0	0	0
4	6	0	0	0	0	0	0	0	0	0

Table 2.6 continued

5	1	0	0	0	0	0	0	0	0	0
5	2	-42.46	153.616	0.087	-69.174	-42.461	54.506	-2.073	0	0
5	3	96.428	61.474	0.221	-66.191	-34.343	27.323	12.383	-7.302	2.146
5	4	502.82	106.212	-261.23	0.046	-80.378	-53.892	33.834	-901.16	858.837
5	5	680.814	57.808	-85.264	-44.439	0	0	0	0	0
5	6	0	0	0	0	0	0	0	0	0
6	1	0	0	0	0	0	0	0	0	0
6	2	0	0	0	0	0	0	0	0	0
6	3	0	0	0	0	0	0	0	0	0
6	4	371.827	47.032	0.363	-89.314	62.949	0	0	0	0
6	5	-773.491	183.756	0.543	79.029	0	0	0	0	0
6	6	0	0	0	0	0	0	0	0	0

Table 2.6 continued

7	1	0	0	0	0	0	0	0	0	0
7	2	0	0	0	0	0	0	0	0	0
7	3	-379.85	140.63	0.312	-239.92	104.97	0	0	0	0
7	4	0	0	0	0	0	0	0	0	0
7	5	-163.97	129.66	0.183	-162.08	110.757	0	0	0	0
7	6	-61.718	188.675	-168.51	0	0	0	0	0	0
8	1	0	0	0	0	0	0	0	0	0
8	2	0	0	0	0	0	0	0	0	0
8	3	0	0	0	0	0	0	0	0	0
8	4	0	0	0	0	0	0	0	0	0
8	5	0	0	0	0	0	0	0	0	0
8	6	0	0	0	0	0	0	0	0	0

Table 2.6 continued

9	1	0	0	0	0	0	0	0	0	0
9	2	0	0	0	0	0	0	0	0	0
9	3	1230.879	-206.95	-87.369	0	0	0	0	0	0
9	4	702.183	80.073	-168.25	-103.23	37.243	0	0	0	0
9	5	0	0	0	0	0	0	0	0	0
9	6	0	0	0	0	0	0	0	0	0
10	1	-97.886	0.807	93.22	0	0	0	0	0	0
10	2	-940.07	156.647	0.751	77.882	0	0	0	0	0
10	3	71.423	78.54	0.656	-54.23	-20.169	14.94	21.51	-24.581	-2.387
10	4	-543.112	127.58	0.68	-63.163	61.956	0	0	0	0
10	5	309.542	0.61	0	0	0	0	0	0	0
10	6	0	0	0	0	0	0	0	0	0

Table 2.6 continued

11	1	0	0	0	0	0	0	0	0	0
11	2	-270.4	167.968	0.374	-221.78	0	0	0	0	0
11	3	416.507	292.17	-485.42	113.938	0	0	0	0	0
11	4	-262.14	136.318	0.402	-196.47	-31.063	48.944	91.975	-22.378	0
11	5	-536.07	162.362	0.46	-128.36	80.766	0	0	0	0
11	6	0	0	0	0	0	0	0	0	0
12	1	0	0	0	0	0	0	0	0	0
12	2	0	0	0	0	0	0	0	0	0
12	3	0	0	0	0	0	0	0	0	0
12	4	0	0	0	0	0	0	0	0	0
12	5	0	0	0	0	0	0	0	0	0
12	6	0	0	0	0	0	0	0	0	0

Table 2.6 continued

13	1	0	0	0	0	0	0	0	0	0
13	2	704.968	90.397	-112.28	-105.05	0	0	0	0	0
13	3	0	0	0	0	0	0	0	0	0
13	4	0	0	0	0	0	0	0	0	0
13	5	0	0	0	0	0	0	0	0	0
13	6	0	0	0	0	0	0	0	0	0
14	1	0	0	0	0	0	0	0	0	0
14	2	1344.73	-102.73	0	0	0	0	0	0	0
14	3	803.11	80.462	-163.17	-71.14	-38.369	27.901	-16.595	-2.973	853.448
14	4	411.44	118.601	0.053	-145.33	-78.835	-35.527	34.249	403.346	0
14	5	0	0	0	0	0	0	0	0	0
14	6	0	0	0	0	0	0	0	0	0

Table 2.6 continued

15	1	0	0	0	0	0	0	0	0	0
15	2	-251.616	105.433	0.463	-41.602	23.26	0	0	0	0
15	3	0	0	0	0	0	0	0	0	0
15	4	37.429	76.454	0.369	-56.019	18.258	0	0	0	0
15	5	-618.285	149.562	0.641	28.106	0	0	0	0	0
15	6	0	0	0	0	0	0	0	0	0

The CDF Mapping

As described above, the region- and PFT- specified plume-rise parameterization is based on reanalysis meteorology dataset (CFSR) and derived fire size and MFRP. When embedded this parameterization in coupled climate model, two things need attention. Firstly, there is a departure between Community Atmosphere Model output and reanalysis data in terms of meteorology parameters. Secondly, the fire parameters we used in parameterization is different from Community Land Model outputs.

To address the first issue, this study uses cumulative distribution function mapping (CDF mapping) method to reduce the departures. This method is effectively used in climate studies. Here we use specific humidity as example, by assuming the CFSR data and CAM5 outputs are both follow normal distribution, the CDF mapping method calculates the means and variances for both CFSR and CAM5 data for a certain fire region and PFT during this region's fire season. For a CAM5 specific humidity value, its CDF value can be determined by using pre-calculated mean and variance. By using this CAM5's CDF value and pre-calculated CFSR mean and variance, the corresponding specific humidity value is determined through follow the CFSR distribution map. Following similar process, the adjusted values of potential temperature difference and the wind speed for different layers are determined in the on-line calculation. As the planetary boundary layer height has significant variances during a day, we apply the CDF mapping for hourly data. The CFSR value against CAM5 value for meteorology parameters for Canada region forest (region 1 & PDF 1) are shown in **Fig.2.11**.

To determine the online fire initial plume velocity and temperature difference, the fire size, MFRP, surface temperature and pressure are needed. The surface temperature and pressure can be obtained from community atmosphere model and the MFRP as a prescribed file have been added in the model as same as in section 2.1.4. The online fire size data is from the burned area in each grid box in CLM and transfers to the CAM. However, this burned area is not the fire size we used to calculate the plume height, because this burned area is the average burned area in each grid box for each time step in CLM. Again, here we use the CDF mapping method to convert the burned area from CLM to the fire size. We use five years CLM burned area to calculate the CDF for the burned area for each region and PFT, while the nine years fire size from our off-line plume height dataset are used to calculate the CDF for each region and PFT. By using the two CDFs we map each online burned area value to the fire size value. The example of the fire size CDF in Canada region forest (region 1 & PDF 1) are shown in **Fig.2.12**.

Additionally, we added the diurnal cycle to the prescribed MFRP. We use the equation (2.10) and the prescribed parameters r, h, b and δ to determine the $MFRP_{peak}$, by assuming the MFRP value is observed at the 11:00 local time. Then by substituting the $MFRP_{peak}$, r, h, b and δ into equation (2.5), the MFRP value as a function of time can be determined.

By using the adjusted fire size, the MFRP with diurnal cycle, surface temperature and pressure, the initial velocity and temperature with diurnal cycle for a wildfire plume is determined. After meteorology parameters and fire parameters are determined, the plume heights are calculated through the simplified region- and PFT-specified plume-rise

parameterization in CAM5 (Fig.2.9). The comparison between online plume heights and MISR plume heights are presented in section 2.3.

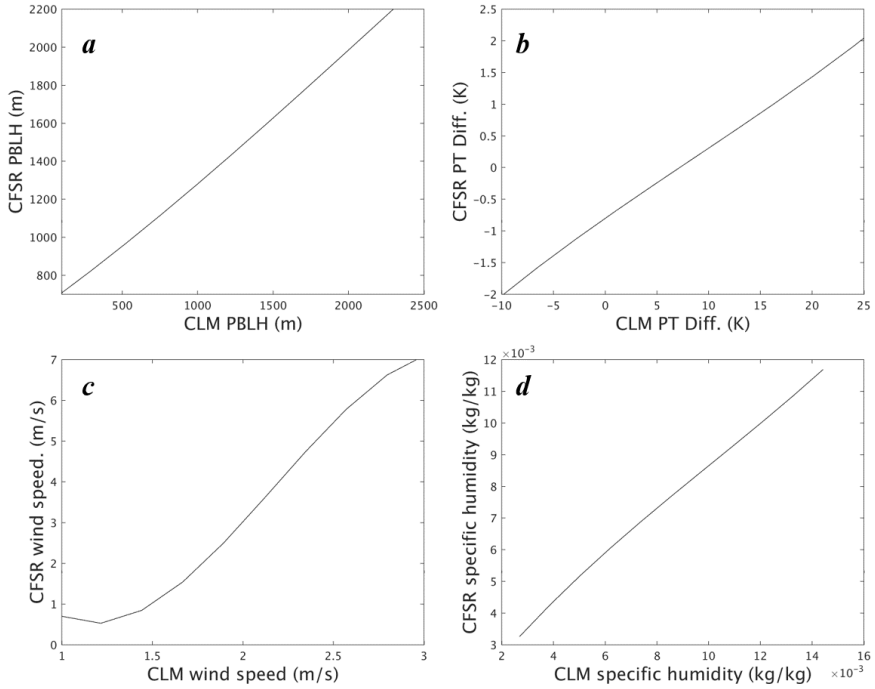

Figure 2. 11. The CLM parameters against CFSR parameters**.**

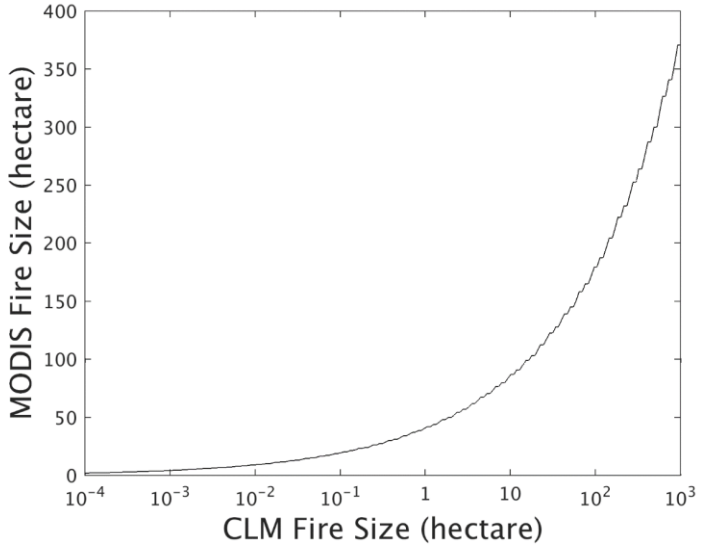

Figure 2. 12. The CLM fire size against MODIS fire size**.**

2.3 Results

The simulated plume heights

The MODIS detected hotspots, whose corresponding MISR plume heights have 'good' quality flag, were identified and then the plume heights of these hotspots were calculated by using modified 1D plume-rise model. These hotspots are defined as MISR hotspots in this study. The MISR plume heights are shown in Figure 2.13a. The MISR plume height dataset has higher sampling density over North America and Siberia, and lower sampling density over tropical region. In general, the plumes are higher than 1800 m over Alaska and Canada region and higher than 1300 m over Siberia region, while the plume heights are largely less than 1200 m over South America and Africa. This pattern can be summarized as low in low latitudes and high in high latitudes. The simulated plume

heights (Fig.2.13b) through modified 1D model largely agree with this high in high latitudes and low in low latitudes pattern, significant improved compared other studies (Sofiev et al., 2012, 2013; Val Martin et al., 2012). Because the tropical regions including South America, Africa and Southeastern Asia are most burned regions over the world, the agreement with MISR over these regions are important for accurately simulating the impact of wildfire emissions on climate and pollutants transport. Previous study greatly overestimate the plume heights in tropical area and underestimate the plume heights over high latitudes (Sofiev et al., 2012, 2013). The overestimate in tropics would affect the evaluation of black carbon's impact on tropic dynamics, such as Hadley Cell (Tosca et al., 2013b, 2015). The underestimate of plume heights in high latitudes would affect the evaluation of black carbon's impact on snow melting in over Arctic region (Keegan et al., 2014). The points-to-points comparison between MISR plume heights and 1D model simulation are shown in **Fig.2. 13c**. Considering there is 500 m uncertainty of MISR data, two-thirds data are in good correlation. There is a systematic lower bias of simulated heights when MISR heights over 3000 m. This is probably due to the insufficient latent heat release in the 1D plume-rise model when plumes above boundary layer. Also, it could be due to the inaccuracy of CFSR data in free troposphere. The histogram comparison is shown in **Fig.2.13d** for 500 m interval. The MISR heights (red) have highest counts in 1000 and 1500 m bins and then the frequency decrease toward both sides. The simulated heights well captured this pattern, but the distribution is less sharp than MISR. Again, the model simulated fewer heights over 3000 m. Overall, the 1D model results well captured the MISR plume heights pattern in terms of the global spatial distribution and the histogram distribution.

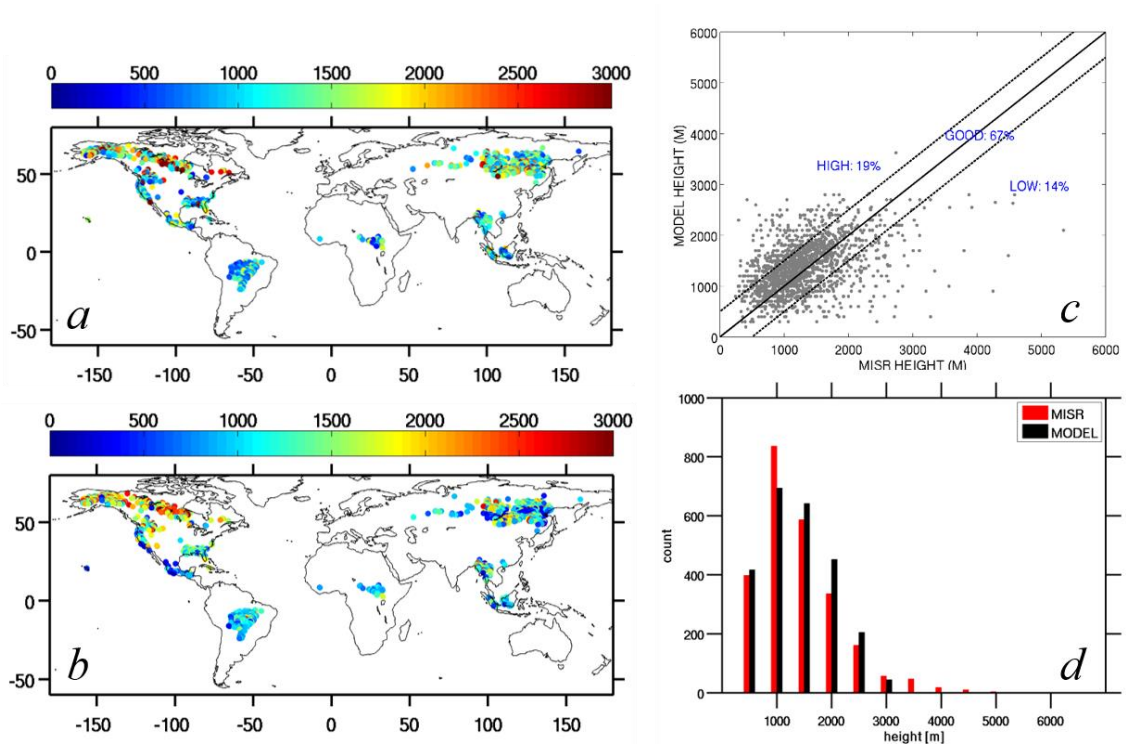

Figure 2. 13. The comparison between MISR and model simulated plume heights. Panel *a* is the MISR plume heights. Dots represent MISR plumes, and the color shading represents plume heights. Panel *b* is same as panel *a*, but for 1D plume-rise model simulated plumes. Panel *c* is plume-to-plume comparison between the MISR and the simulated heights. The *x* axis is the MISR heights and the *y* axis is the simulated plume heights. Panel *d* is the histogram comparison between the MISR plume heights (red) and the model simulated heights (black) in 500 m interval**.**

Through substituting FRP with diurnal variation and CFSR data into 1D model, the diurnal variation of plume heights of MISR hotspots were simulated and is shown in Fig2.1 4 (left). The bars represent standard deviations. The mean of MISR heights and standard deviation are shown in blue color. The corresponding simulated heights are shown in cyan (not in integer local time). The mean values of the simulated heights well agreed with MISR heights, with smaller standard deviation. The mean values of MISR heights also very close to the mean heights of all hotspots simulated around 11:00 am (local time). The simulated

diurnal cycle displays a Gaussian function shape with a peak around 14:00, around the Aqua Satellite overpass time. This feature is expected as the input FRP has similar diurnal cycle and has peak around 14:00. The mean value of peak heights is 2041 m, compared to the mean value of MISR heights is 1300 m. The results indicate that the diurnal cycle of MFRP are important to accurate simulate the diurnal variability of plume heights.

The penetration rate of the plumes means the percentage of plumes higher than corresponding boundary layer height. In this study, the boundary layer heights are from CFSR (Fig. 2.14a). The average values of boundary layer heights have similar diurnal pattern as plume heights. The calculated penetration rate in daytime are shown in Figure 4b. The penetration rate of MISR plume heights is around 19% agree with other study (Val Martin et al., 2012). The simulated penetration rate is 25%, slightly higher than MISR plume penetration rate (Fig. 2.14b). After 11:00 o'clock, the penetration rate keeps increasing till reaching the maximum 53% at 16:00 in late afternoon. This also can be seen in the increasing overlaps of plume heights and boundary layer heights within standard deviation since 11:00 and the decreasing trend in late afternoon (Fig. 2.14a). The higher penetration in the afternoon indicates that there would be more fire emissions released in the free troposphere than previous studies estimates (Val Martin et al., 2012) and suggest possible longer transport distance and lifetime of pollutants from wildfire emissions.

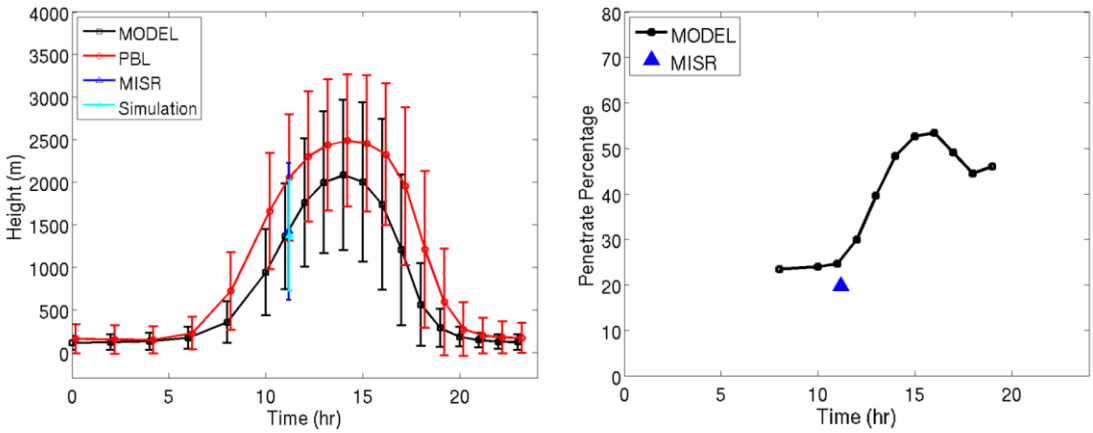

Figure 2. 14. The simulated diurnal variation of the plume heights. The left panel shows the model simulated plume heights (black) and corresponding planetary boundary layer heights (red) vary as a function of time. The dots represent means and the error bars represent the standard deviations. The MISR plume heights are shown in blue and corresponding simulated heights are shown in cyan. The right panel shows the penetration rates of each hour for the daytime. The simulated penetration rates are shown in black, while the MISR observed penetration rate is in blue

Through applying the processes described above (Fig.2.1) to the detected wildfire hotpots from 2002 to 2010, the global hourly plume height dataset were developed. Daily hotspots from MODIS Terra satellite with confidence level higher than 50 were chosen, as well as corresponding CFSR meteorology data and region- and PFT-specified MFRP. An overview of these results is shown in figure 2.15. The top panel (Fig. 2.15a) shows the averaged plume heights when Terra satellite overpassed. The long-term plume heights were averaged in CFSR grid cells during 2002 to 2010. The global pattern of these long-term means assembles the pattern shown in MISR plume heights: high in high latitudes and low in low latitudes. Alaska, Canada, and Siberia have relative higher plume heights from 1500 to 2000 m compared to tropical region where plume heights are from 500 to 1200 m largely. The west US mountains have highest plumes of world with a range from 2000 to 3000 m. This part is not detected by MISR plume heights data.

The middle panel (figure 2.15b) shows the long-term averaged plume heights at 2:00 pm in January. As mentioned before, the 2:00 pm plume height is the daily maximum. In January, the wildfires are focus on Southern Hemisphere. The middle panel shows high fire density in southern hemisphere and limited hotspots in northern hemisphere. The plume height peaks in northern hemisphere are largely less than 1000 m due to stable atmosphere condition (winter) and weak burn intensity. The peaks in southern hemisphere are much higher, surplus 3000 m at most places, probably due to unstable atmospheric conditions and strong burn intensity. The day maximum in July are shown in bottom panel (figure 2.15c). In boreal summer, the wildfires are vibrant in both hemispheres. The Alaska, Canada, and west US mountains have highest plumes in Northern hemisphere. The plumes in Siberia are moderate. The plumes in east US and most of European and eastern China are weak. In Southern Hemisphere, central South America and southern hemisphere Africa has highest plumes. The results are more reasonable than previous study (Sofiev et al., 2012).

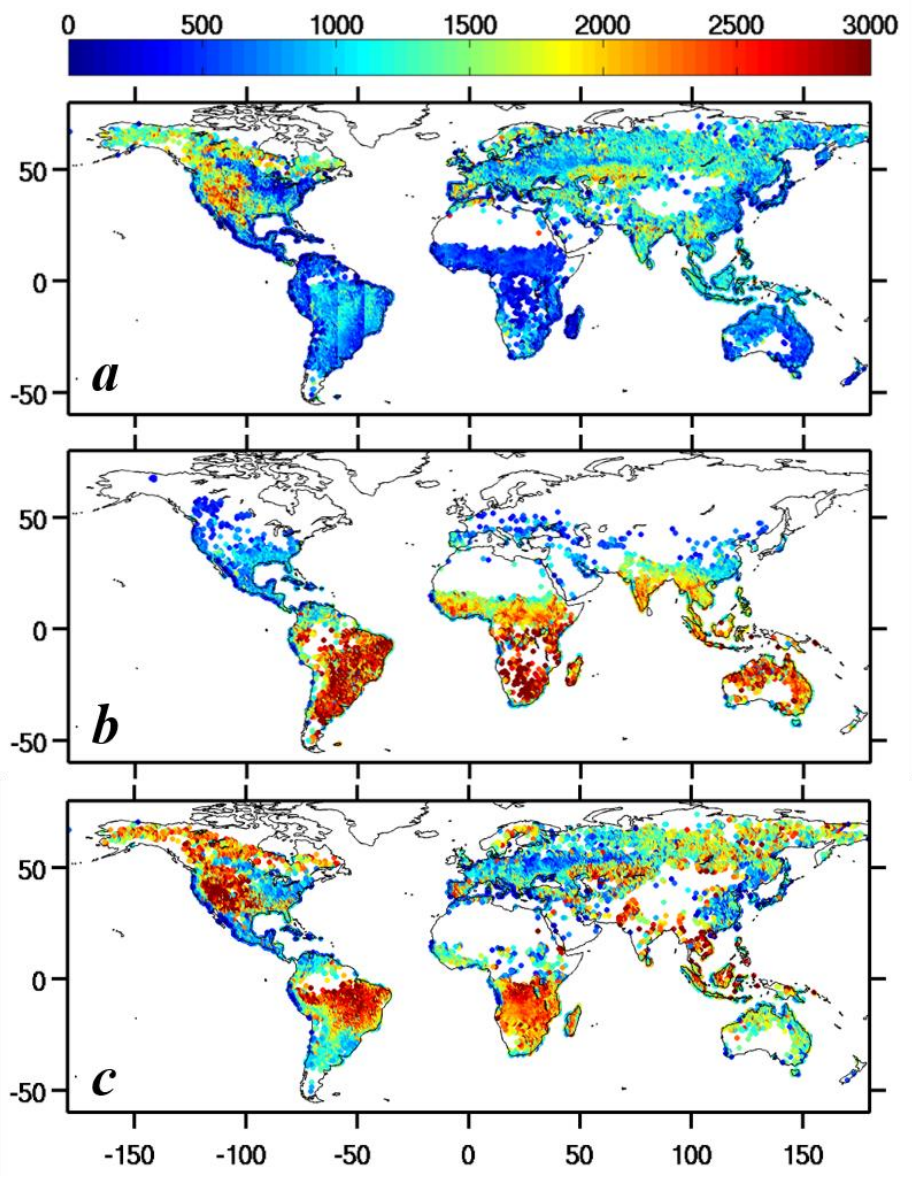

Figure 2. 15. The mean of model simulated plume heights from 2002 to 2010. The panel *a* is the mean of plume heights at 11:00 am local time. The panel *b* is the mean of plume heights at 2:00 pm in January. The panel *c* is same as panel *b*, but for July**.**

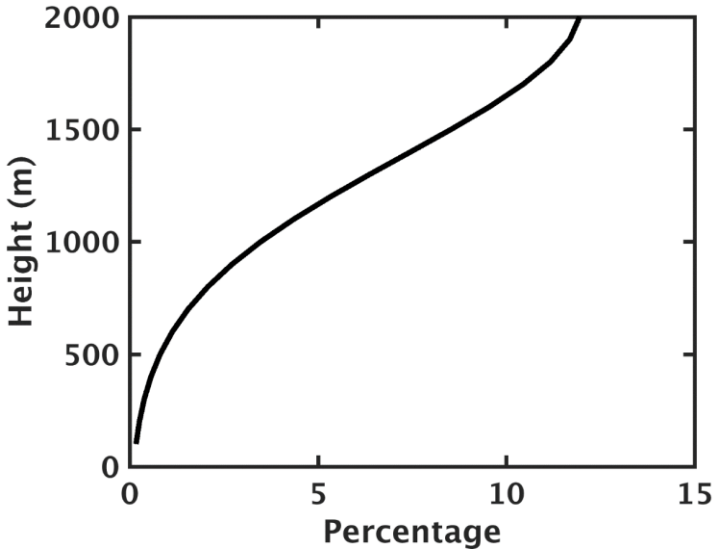

Figure 2. 16. The emission distribution of a 2000 m height plume. The x-axis is the percentage of the emission distributed at each 100 m interval. The y-axis is the height.

Above described the plume heights calculated by the 1D plume-rise model. As the height of a plume is determined, the vertical profile of the distribution of wildfire emission is determined by a half Gaussian curve. For the Gaussian curve (the probability density function), we assume the mean is zero and the sigma is one third of the height. Then we use the first half of this curve and distribute least at the ground and the most at the height of the plume. The distribution of a 2000 m height plume is shown in Fig.2.16, where the distribution is normalized to 1. Through this method, we calculated the zonal mean of the distribution weighted by individual fire's FRP along the latitude between 2002 and 2010. The cumulative emission distribution against height from surface at 14:00 local time, which is the peak emission time during a day in GFED hourly emission data (Mu et al., 2011), is shown in Figure 6 and 7 for January and July, respectively. In January, the wildfire mostly occurred in the Northern Hemisphere South America and the North Hemisphere Africa,

and most burned PFT are grass-savanna (PFT4) and forest (PFT2) (Giglio et al., 2013). Therefore, majority emission released at between 0~20^{o} N. In this region, the distribution height of the 50% emission for PFT2 and PFT4 is between 1500 ~ 2000 m, with the height of 75% reaching to 3000 m (Fig.**2.7**), compared to the 0 ~1000 m distribution setting in AeroCom protocol. Additionally, as January is the winter in Northern Hemisphere and the summer in Southern Hemisphere, the distribution height in Southern Hemisphere is higher than northern hemisphere, although it is not the fire season in Southern Hemisphere.

July is the most burned month and it is the fire season for eight fire regions from Northern Hemisphere to Southern Hemisphere: Boreal North America, Boreal Asia, West Temperate North America, Europe, Middle East, Central Asia, South Hemisphere South America and South Hemisphere Africa (Giglio et al., 2013). For the tropic region (30^{o} S ~ 30^{o} N) especially in the Southern Hemisphere (SHSA and SHAF), where release the most emission, the 50% distribution height of grass-savanna and forest, which are the most burned PFTs (Mu et al., 2011), is between the 1500 to 2500 m with 75% distribution height reaching to 2500 to 3000 m (**Fig.2.8**), compared to the 0 ~ 1000 m in AeroCom protocol. In the Northern Hemisphere temperate region (30 ~ 60^{o} N), the 50% distribution height of forest (PFT1 and PFT2) is between 2000 to 2500 m with 75% distribution height reaching to 3500 to 4000 m, while the 50% distribution height of the height of grass-savanna (PFT4) is between 2500 to 3000 m with 75% distribution height reaching to 4000 m. In comparison, the emission is released between 0 to 2000 m in this region according to AeroCom protocol.

Two comparisons are designed to investigate the impact of plume heights on global AOD. The first is to compare the CAM5 simulated wildfire related AOD with CALIPSO smoke AOD. This comparison is to test whether our simulations captured the main features of AOD associated with wildfire emissions. As mentioned before three CAM5 runs are performed to simulated the AOD under GEOS5 meteorology data constrain. We define the wildfire related AOD as the difference between the plume smoke run (GFED4s emission with plume-rise) and control run (no wildfire emissions). The AOD mean in January between 2006 to 2010 are shown in **Fig. 2.17** upper right panel, characterized as strong impact over northern Africa burning area transport with easterlies. The January mean of CALIPSO smoke AOD from 2006 to 2010 are shown in **Fig.2.17** upper left panel, with similar response over northern Africa but less intensity. There is strong signal over China and India in January from CALIPSO smoke AOD, while there is no such signal in CAM5 simulated wildfire related AOD. The GFED4s data does not have significant emissions in China and India during the winter and the winter is not the burning season in Asian. Therefore, we think this AOD signal in CALIPSO is noise probably caused by the industry emissions which are strongest during the winter in China and India.

The CAM5 simulated mean wildfire related AOD in July between 2006 to 2010 are shown in **Fig.2.17** lower right panel, while the CALIPSO counterpart are shown lower left panel. The strongest AOD signals are from south equator Africa, where the wildfires contribute to 0.3 AOD difference. The CAM5 also simulated the wildfire related AOD reaching 0.1 magnitude over South America transporting westward with easterlies. These patterns are validated by CALIPSO data. Over northern hemisphere, the CAM5 simulated wildfire AOD is less than 0.1 over North America and Siberia. Considering the background

AOD over same areas are small (around 0.1), these contributions are not negligible. Similar AOD patterns are shown in CALIPSO July data (**Fig.2.17**. lower left). Again, the China AOD signal in CALIPSO data are not captured by CAM5 runs.

The second comparison of AOD is to investigate the impact of plume heights on AOD difference. We define the contribution from the plume as the percentage values of the AOD departures between the plume smoke run and the surface smoke run relative to the no-fire climatology AOD, which is from the control run. Three typical months are shown in **Fig.2.18**. As the hypothesis is that the plume enhances the transport of the wildfire emissions, the plume should enhance the AOD at the downstream of the wind direction while reduce the AOD at the upstream compared to releasing the wildfire emission at the surface. In **Fig.2.18a**, the AOD are enhanced from 20 to 50 percent at the eastern Siberia while a little decrease the western Siberia in May 2006. The midlatitude eastward winds play a role in this transport. In **Fig.2.18b**, the plume's impact in July 2006 are shown. The AOD enhanced 20% over middle to eastern Canada while reduced 30% at western Canada. This is typical smoke transport during summer that western Canadian wildfire pollutants impact the east coast. The AOD also enhanced over 50% in high latitude Siberia and reduced more than 20% in central Siberia, linking to the summer black carbon increase in Arctic area. The AOD over Africa increased 30 to 50% between $10^o S$ to 20^oS but decreased 10 to 20% between equator to $10^o S$ and transport to eastward. There is a weak positive belt (~10%) between Africa to South America. This suggested that the plume enhanced the Africa wildfire pollutants transport over the Atlantics. In **Fig.2.18c**, the plume enhanced AOD 30% over the west coast of South America and slightly reduced the AOD over Amazon area in Sep.2007. Meanwhile, the AOD enhancement about 10% found over

northwest Siberia and reduced over central Siberia. Therefore, the plume heights significant enhanced the pollutants transport over downstream and reduced the pollutions over the wildfire location. This effect is profound especially for the big wildfire events and obvious over high latitudes as background AOD is low and obvious over Africa as emissions are strong enough.

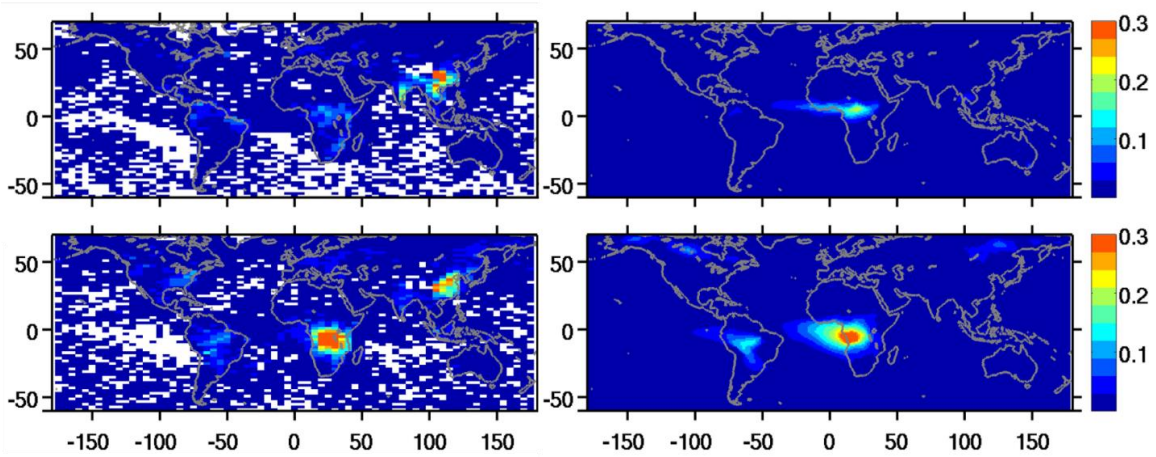

Figure 2. 17. The comparison of the CALIPSO and the CAM5 simulated AOD. The upper left is the averaged CALIPSO smoke related AOD in January while the bottom left is for the July. The upper right is the averaged CAM5 simulated wildfire related AOD in January while the bottom right is for the July**.**

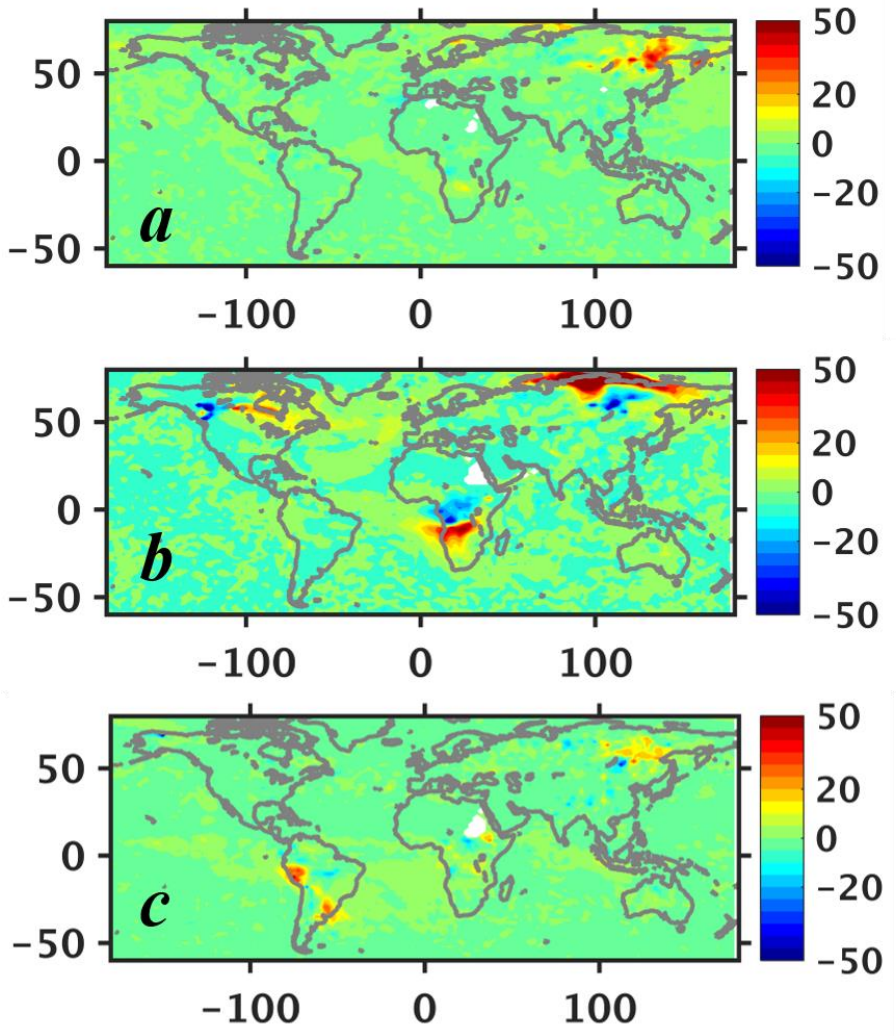

Figure 2. 18. The impact of plumes on monthly AOD. The impact is represented by the percentage values of the AOD departures between plume smoke run and surface smoke run relative to the no-fire climatology AOD. The panel a is for 2006.5, the panel b is for 2006.7 and the panel c is for the 2007.9.

the results of on-line plume-rise implementation

To verify this parameterization independently, we use this parameterization to simulate the plume heights for the MISR hotpots and compared to the MISR detected plume heights. The difference between the simulated heights and the MISR plume heights

is shown in Fig.2.19. Generally, the difference is well confined in 500 m especially in the tropics and North America, where previous study has most deviation (Sofiev et al., 2012), suggesting that our parameterization keeps the main features of MISR height, which is high in high latitudes and low in low latitudes. Also, our results have overestimated the plume heights in Siberia region and have underestimated the plumes in Canada for limited plumes, although the difference is below 1000 m. The point-to-point comparison has been shown in Fig 2.19b. Overall, the parameterization has reasonably well results when the MISR plume is under 3000 m. However, it tends to underestimate the plumes when the MISR plume height is above 3000 m. Again, this may be due to the lack of the representing the latent heat release process in our parameterization.

Through methods mentioned in section 2.2, the plume-rise parameterization with CDF mapping was implemented in CESM for full coupled runs. To evaluate the performance of this plume-rise implementation, we run the coupled CAM-CLM with improved fire scheme for one full year. As a full-coupled run, it is not possible to reproduce the meteorology conditions exactly like the conditions when MISR plumes measured. Therefore, we use the monthly mean plume heights instead of daily ones. The results are shown in Fig. 2.20. The pattern of coupled plumes is like MISR plume pattern: higher plumes in high latitudes and lower plumes in low latitudes. This results suggest that the online plume-rise implementation simulate the plume heights reasonable well, compared to the previous studies, which gives the high plumes in tropics and low plumes in high latitudes (Sofiev et al., 2012, 2013). The diurnal cycle of the plume heights in July are shown in Fig.2.21. The diurnal cycle resembles the simulate diurnal cycle in Fig2.14 (black line): has a peak at 14:00 local time and maximum height around 2000 m.

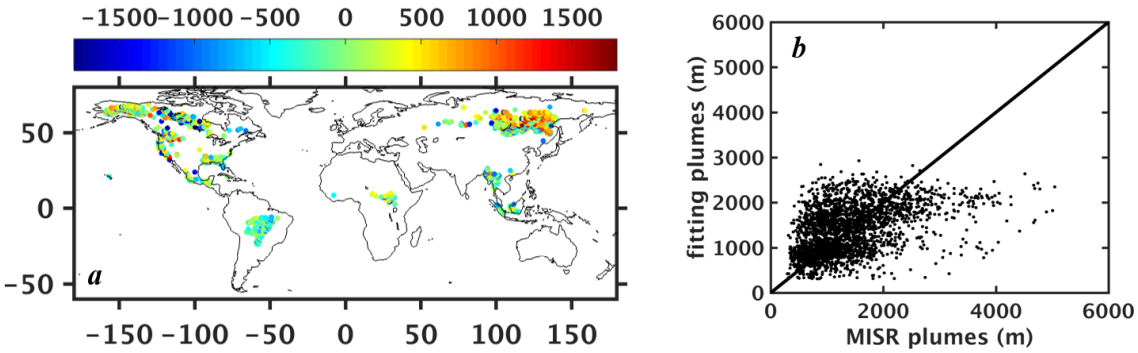

Figure 2. 19. The verification for linear parameterization. The panel *a* is the comparison between the simulated plume heights resulted from Stepwise simplified parameterization and the MISR plume heights. The color shading represents the value of the departure range from -1800 to 1800 m. The panel *b* is the plume to plume comparison between MISR heights and simulated results.

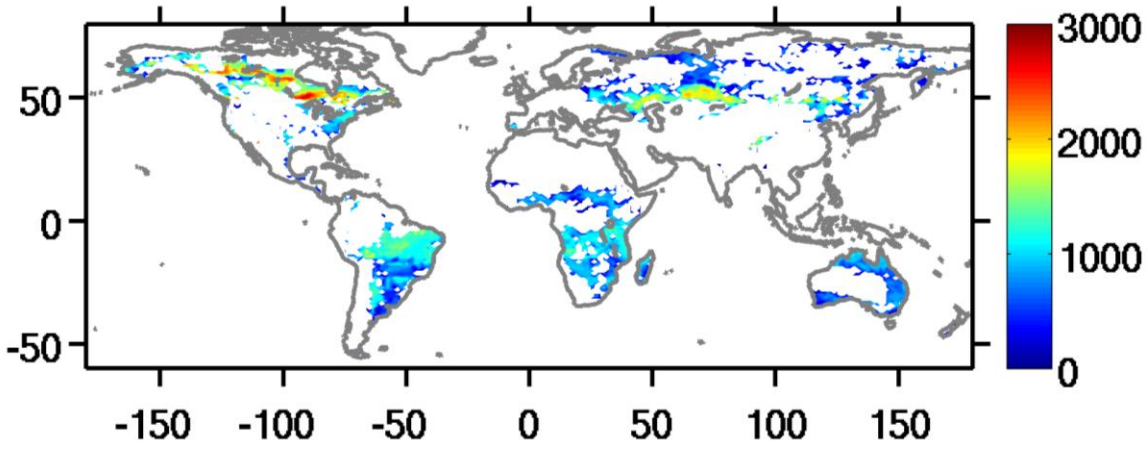

Figure 2. 20. The plume heights resulted from CAM5 plume-rise implementation. The *x*-axis is the longitude and the *y*-axis is the longitude. The color shading represents plume heights

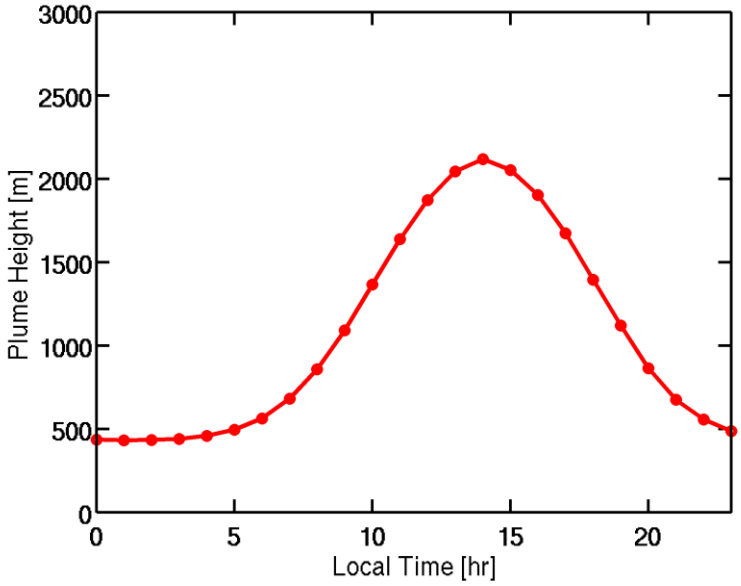

Figure 2. 21. The diurnal cycle of the averaged plume heights in July from CESM**.**

2.4 Conclusion

This study developed long-term plume heights dataset through using modified 1D plume-rise model and region- and PFT-specified MFRP and fire size data as inputs, as well as CFSR meteorology variables. By considering the diurnal variability of wildfire intensity, the simulated plume heights have reasonable diurnal cycle. The simulated plume heights well captured the MISR plume heights pattern: high in high latitudes and low in low latitudes. This is a significant improvement compared to previous studies, which produced high plumes in tropics and lower plumes in high latitudes (Sofiev et al., 2012, 2013). With adding in diurnal variability, the penetration rate of plumes increases from morning to late afternoon, from 20% to more than 50%, suggesting the increase of plume heights is faster than the increase of boundary layer heights. Based on the calculated plume heights, the

vertical wildfire emission distribution is calculated. The zonal mean of the distribution shows that the plume release the emission at much higher altitude in tropic and temperate regions compared to the AeroCom Protocol, which is widely used in the CESM simulations. Combined with GFED4s data, the impact of plume heights on AOD was evaluated through CAM5 simulations: control run, surface smoke run, and plume smoke run. The simulated wildfire related AOD well capture the main features of CALIPSO smoke AOD. The difference between plume smoke run and surface smoke run suggested 20 to 50% enhancement of increase of monthly AOD mean away from wildfire spots in both tropics and high latitudes region, suggesting the significant role of plumes in big wildfire events in understanding the pollutants transport and potential impact on radiation balance over tropics and high latitudes.

For on-line coupled simulation purpose, a plume-rise implementation has been developed. This implementation is based a parameterization of linear regression model, which reasonably reproduced the MISR plume heights via less than 9 parameters. Rely on CLM fire parameter and CAM meteorology variables and CDF mapping method, the plume heights resulted from the plume-rise implementation well captured the main features of MISR plume heights and this implementation is computational efficient.

For better understanding the role of plume heights in climate, more dedicated analysis and regional simulations are needed to discuss the impact of plume heights. For example, how much ice melting could be promoted if plume heights are taken into consideration over Artic region during summer. Or evaluate the impact of Canadian wildfires on Northeastern U.S. air quality, if the long-distance transport of fire pollutants is significantly promoted by plumes.

CHARPTER 3. PLUME HEIGHT DATASET APPLICATION: PERTURBATION OF NORTHEASTERN U.S. AIR QUALITY BY WILDFIRES OVER WEST CANADA DURING SUMMER

This chapter is the application of the plume height dataset. West Canada wildfires (WCWs) have been increasing in recent decades. Fire emitted aerosols can significantly affect air quality and increase the ratio of organic carbon (OC) to elemental carbon (EC) in downwind regions. The research domain is shown in Fig.3.1 and the region partition are shown in Table 3.1. Although the WCW (red box) is far from NEUS (cyan box), this study shows the WCW has strongest impact on NEUS in the summer compared to other fire regions. This strength of the impact depends on the fire intensity and atmosphere transport intensity.

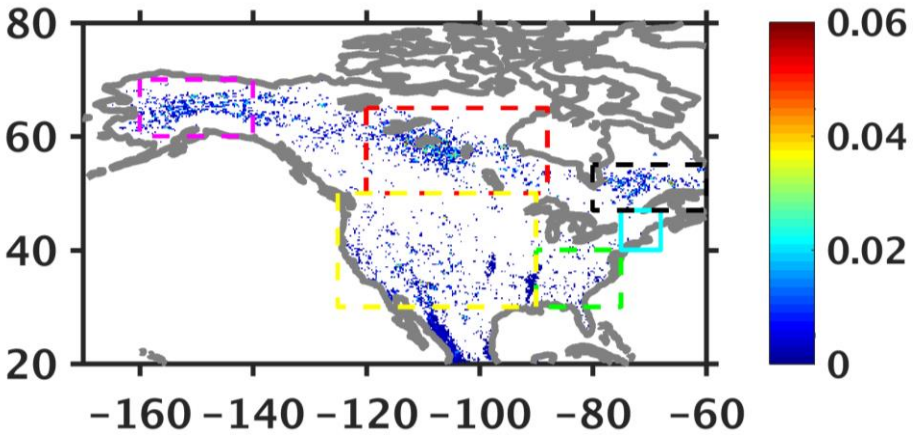

Figure 3. 1. The averaged June burn fraction in North America. The color shading represents the value of burn fraction for each grid. The red dashed box represents the WC region, while the cyan box represents the NEUS region.

Table 3. 1. The location of the regions shown in Fig. 3.1

Region Full Name	Abbreviation	Longitude Range	Latitude Range
Northeast U.S. region	NEUS	75~68 W	40~47 N
Alaska region	AK	160~140 W	60~70 N
West Canada region	WC	120~88 W	50~65 N
East Canada region	EC	80~60 W	47~55 N
West U.S. region	WU	125~90 W	30~50 N
Southeast U.S region	SU	90~75 W	30~40 N

3.1 Data and methods

The IMPROVE data and OC/EC ratio

The OC and EC mass concentration measurements are from the Interagency Monitoring of Protected Visual Environments (IMPROVE) network. Most of IMPROVE sites are located in the class I area, covering national parks and wildness areas defined by Clean Air Act in 1977, with small local emissions to present the background conditions (Zeng and Wang, 2011). Since 2001, an IMPROVE sample was collected at each site every three days instead of two days per week prior to 2001. A total of up to 11 samples could be collected in a one-month period, but at most sites, a few samples were missed. We calculated the monthly mean OC and EC for each site and excluded the monthly mean for a site if fewer than 4 samples were included in a month (Malm et al., 2004).

In general, there is a prominent OC and EC concentration decrease from IMPROVE data in North America in recent decades, especially in NEUS area (Fig. 3.2) due to the effort of the anthropogenic emission reduction (Fiore et al., 2014; Gégo et al., 2007; Saunders and Waugh, 2015). Particularly, this anthropogenic emission reduction leads to stronger EC reduction compared to the OC reduction, resulting in an increasing trend of the OC/EC ratio. This anthropogenic decadal variability is a 'noise' for this study and was attenuated by removing the linear trend in the OC and EC data before OC/EC ratio calculation, assuming this trend has little seasonally variability. We assume the trend is linear and can be expressed as equation 3.1.

$$y = ax + b \tag{3.1}$$

In equation S1, the x is the data number and the y is the trend of concentration. The a is the slope and the b is a constant. By using the least square method, the a and b can be determined. The original data subtract the trend (y) giving the detrend concentration. The detrend concentration pluses the mean concentration from 2001 to 2015 to keep the magnitude of the data. Both OC and EC data have been processed before analysis.

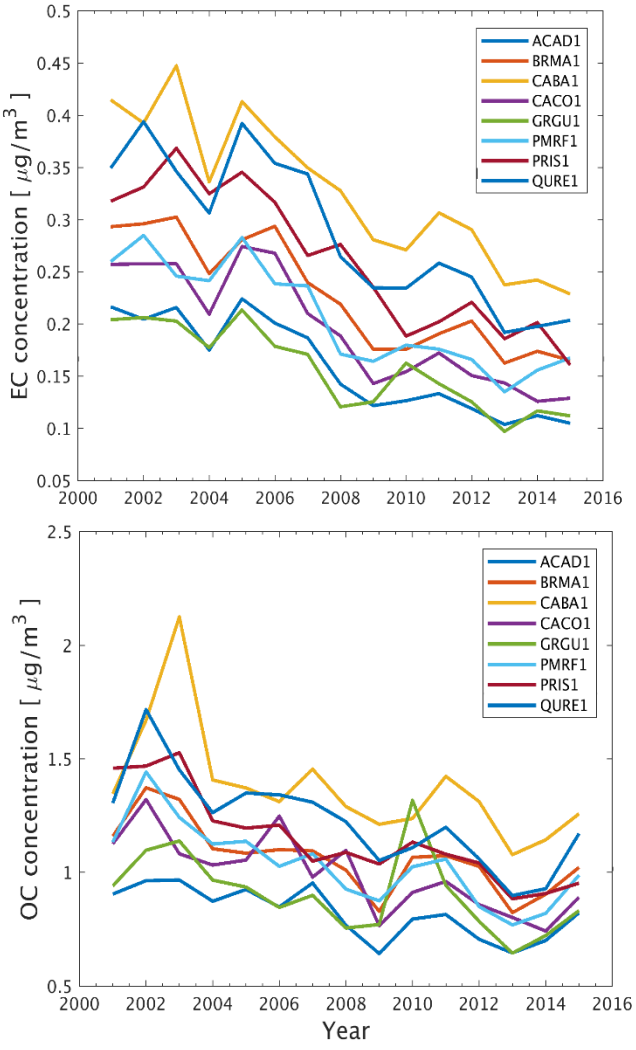

Figure 3. 2. The EC and OC trend in recent decade in NEUS sites. The x axis is the year and the y axis is the pollutant concentration. The legend shows the eight sites in NEUS. The upper panel is for the EC concentration and the bottom panel is for the OC centration.

The AOD data

The aerosol optical depth data used in this study is the monthly mean deep blue 550 nm product, which is the level 3 product from Aqua (MYD08_M3) with $1^o \times 1^o$ resolution (Levy et al., 2007). The Study suggested the MODIS AOD has better performance compared to CALIPSO AOD with higher resolution (Ma et al., 2013). This

study uses the MODIS MYD08_M3 deep blue AOD from 2003 to 2015, as it lacks the June data in 2001 and 2002.

The region partition, GFED data and wildfire index

In this research, the NEUS region is defined as the cyan box in **Fig.3.1**, whose range is from -75 ~ -68^{o} W and 40 ~ 47^{o} N, including big cities such as New York City, Boston, and Philadelphia. The west Canada region is from -120 ~ -88^{o} W and 50 ~ 65^{o} N. The averaged burned area in west Canada region in June from 2001 to 2015 is used as the WCWs index to quantify the intensity of wildfires.

Here we use the fourth version of the Global Fire Emission Database (GFED) burned area product (Giglio et al., 2013) with small fires (GFED4s, (Randerson et al., 2012)). This version combined active fires and burned area observations from the MODIS to provide better estimates of burned area compared to GFED3 version (Randerson et al., 2012) with 0.25x0.25 spatial resolution. For consistency purpose, we only use the monthly GFED4s data from 2001 to 2015, because the data from 1997 to 2001 were collected from Visible and Infrared Scanner and European Space Agency Advanced Along Track Scanning Radiometer with different approaches (Chen et al., 2016). In this study, we use the monthly GFED4s burned area and emission data instead of the daily data based on two reasons. Firstly, the uncertainty of the daily data is significant, 5 to 7 days in average in west Canada region and could up to 20 days under some circumstances (Giglio et al., 2013; van der Werf et al., 2017). Secondly, the daily distribution of burned area and emission are inconsistent. For the burned area, the daily distribution is from the MCD64A1(burn

scar) burn date information, while for the emission product, the distribution is from MCD14ML(hotspots) in the extratropical area (van der Werf et al., 2017).

The NCEP geopotential heights, geostrophic winds, EOF analysis

In this study, we use the NCEP/NCAR monthly reanalysis geopotential height data (Kalnay et al., 1996) to investigate the effect of atmospheric circulation on wildfire pollutants transport. The data is monthly mean data and has spatial resolution $2.5^o \times 2.5^o$ with 30 vertical layers. The geopotential height and the associated geostrophic winds at 850 mbar surface were examined and shown in Figure 2. The way to calculate the geostrophic wind is shown in supplementary materials.

Because the empirical orthogonal functions (EOF) analysis gives independent modes of variability, it is wildly used in atmospheric and oceanic studies (e.g., Fiore and Jacob, 2003; Yuan Zhang et al., 1997). In this study, the EOF analysis was performed on the NCEP geopotential height data to identify the atmospheric variability that promotes the long-range pollutants transport.

The climate model experiments

In this study, we use the Community Earth System Model (CESM) version 1.2, with the community atmosphere model version 5 (CAM5) (Neale et al., 2012) coupled with community land model version 4 (CLM4) (Oleson et al., 2010). The 3-mode Modal Aerosol Model (MAM3) is included in CAM5 to simulate the aerosol lifecycle. In the MAM3, the aerosol mass and number mixing ratio are included in three lognormal modes: Aitken, accumulation, and coarse mode. Particularly, the BC and primary organic matter

(POM) from both wildfires and anthropogenic sources are emitted into accumulation mode in the MAM3 and immediately mixed with any hygroscopic species in this mode (Liu et al., 2012).

The CAM5 was run in a resolution of 0.9^{o} latitude by 1.25^{o} longitude and 30 vertical levels globally and for the time period of the year 2000 to 2010 with prescribed SST and sea ice. The year 2000 is used for model spin-up, and the data from 2001 to 2010 are analyzed. The Global Fire Emission Database version 4 with small fires (GFED4s) daily emissions for BC, POM and sulfur dioxide are prescribed (Randerson et al., 2012). The vertical distribution is based on the prescribed hourly plume distribution with diurnal variations from the global plume heights dataset. The anthropogenic and biogenic emissions are from IPCC AR5 dataset (Lamarque et al., 2010). We performed the control experiment (WO-FIRE) with the GFED4s emission turned off, and a sensitivity experiment (W-FIRE) with the GFED4s emission turned on while all other emissions keep the same. The difference between the two experiments was used examine the impact of the wildfire emissions. Ten ensemble members are performed for each of these experiments, which are used to investigate the role of the atmospheric circulation in pollutants transport. A summary of these two experiments can be found in Table 3.2

Table 3. 2 The climate model experiments summary

Experiments	Members	Fire Emissions	Anthropogenic and Biogenic Emissions	Data Availability
WO-FIRE	10	off	on	2001~2010

W-FIRE	10	on	on	2001~2010

The surface OC concentration and the vertical integrated OC transport are used to analyze the wildfire pollutants transport in the model simulations because the OC is a major spacy emitted by wildfires (Van Der Werf et al., 2010). Here the OC concentration includes both POM and SOA in different aerosol modes. The vertical integrated OC transport vector, $\vec{Q}$, is defined as:

$$\vec{Q} = \sum_{i=1}^{N} c_i * \vec{u}_i * h_i \tag{3.2}$$

where the c_i, $\vec{u}_i$ and h_i are the concentration of OC, horizontal velocity vector and the depth for each vertical layer *i*, respectively. The vertical layers are from the surface (*i*=1) to the top of the troposphere (*i*=N). The unit is kg/ms. This variable is useful to measure the horizontal transport of pollutants by the wind field (Christoudias et al., 2012).

In order to identify the special pattern that promotes transport in the ensemble members, the projection of the identified NCEP special pattern on the model members is calculated. Linear regression method is used to make this projection. As there are 10 members for each simulated year in each ensemble, the member with the highest values of projection in a year minus this year's mean is defined as the transport effect caused by the special pattern in this year.

3.2 Results

The linkage between the WCWs and the NEUS OC/EC ratios

The total burn area in WCWs is nearly four times greater than the total burned area in East Canadian region (EC), 2.10e+11 m^2 per year compared to 5.4e+10 m^2 per year according to GFED4s data. The fire season in WC is between June to August, which contributes more than 85% burn area for an entire year. The major fire regions in North America are shown in Table 3.1. The correlation between WCW burned area and the OC/EC ratio in IMPROVE sites over the U.S. in June are shown in **Fig.3.3*a***. In most area of U.S., the IMPROVE measurements are not related to the WCWs index. The correlations in the Western U.S. are poor except few individual sites. This is agreed with the previous study (Malm et al., 2004) that reported the West U.S. air quality disturbance is highly related to the wildfires occurred in West U.S. At the east part of the U.S. the correlations improve but still not significant, because their OC/EC ratios are more related to the prescribed wildfires in the Southeast U.S. (Hu et al., 2008; Zeng and Wang, 2011). However, the WCWs are strongly related to the NEUS region (cyan box), as six out eight IMPROVE sites in this region have a significant correlation (Table 3.3), with correlation coefficients range from 0.50 to 0.81, implying a possible long-range transport from WC to the NEUS on the decadal timescale. The normalized temporal variability of the NEUS regional OC/EC ratio (black line) and the WCWs index (red line) are shown in **Fig. 3.3c**. The two variability is significantly correlated with a correlation coefficient value 0.69, suggesting that the WC wildfire modulates the NEUS OC/EC ratio in general. While the significant correlation between the NEUS and the WC region, there is no obvious correlation between the NEUS and other fire regions, implying that the long-range transport is the reason of this correlation, but not the concurrency with other wildfire regions that transport pollutants to the NEUS (Table 3.3). The MODIS AOD corroborates

this correlation (Fig. 3.3b). The highest correlation3 are within the west Canada region (red box), and this correlation extends southeastward. There are fair to good correlations among the east coast region similar to the panel *a*.

Therefore, it is reasonable to consider that the climatological meteorology condition could in favor of the transport from WC to the NEUS. The averaged geopotential height at 850 mbar surface in June from 2001 to 2015, and corresponding geostrophic wind fields are shown in Fig 3.4 upper panel. The geopotential height field can be characterized as a low-pressure system located at the Northeast and a high-pressure system located at the southeast, resulting in the strong northwest to southeast geopotential height gradient from WC region to NEUS, causing the winds blew southeastward to the NEUS. This geopotential height pattern and the corresponding wind field suggest a possible path to transport WCWs pollutants to the NEUS.

A linear regression model is built to reconstruct the OC/EC variability by using WCWs index, shown in equation (3.3). In this equation, the $\hat{y}$ represents the reconstructed NEUS regional OC/EC ratio,

$$\hat{y} = a_1 F + a_2 \tag{3.3}$$

The F represents the fire strength and the a_1 and a_2 are the coefficients. The $a_1 F$ term represents the effect of the WCWs intensity on NEUS through the atmospheric climatology transport. By using least square method, the a_1 is 0.69 and the a_2 is 0. The departure between the $\hat{y}$ and the original one is shown in Fig.3.5. Here we focus on four years 2002, 2006, 2010 and 2015, in which the WCWs has peaks, and the difference of these four years are -0.2, 0.8, -1.5 and 0.7, respectively. Except the reasonable value in 2002, the

reconstructed value over estimates the OC/EC ration in 2006 and 2015, and underestimates the value in 2010, implying that there could be another atmospheric pattern that plays role in the transport, which is named as the 'special pattern'.

In order to adapt to the transport effect caused by the special pattern, the linear regression model is rewritten as equation (4), where the a_1F is the same as in the equation

$$\hat{y} = a_1F + a_2T_2F + a_3 \quad (4)$$

(3) and the a_2T_2F represents the transport effect caused by the special pattern, where T_2 represents the strength of the special pattern. The a_1, a_2 and a_3 are the coefficients.

In order to find this special pattern, the EOF analysis has been performed on the geopotential anomalies at 850 mbar surface, and the fourth PC fits in the equation (3), which has low strength in 2006 and 2015, and high strength in 2010. The fourth EOF explained 9.2% variance and the variance explained by other EOFs are listed in Table 3.4. The reconstructed OC/EC ratio (Fig.3.3c, green triangles and dashed line) by equation (3) highly resembles the original one with a correlation coefficient value 0.91 and well reconstructs the value in four WC fire peaks. Almost all the reconstructed values fall in the 10th percentile to 90th percentile range, except a slight departure in 2005 when the wildfire intensity was very weak. The values of a_1, a_2 and a_3 are 0.68, 0.54, and 0.04, respectively. The WCWs index alone explains 48% variance (equation 3.3), and the combination of the fire intensity and transport pattern explains 83% variance of original OC/EC ratio. In other word, the transport effect due to the special pattern explains 35% variance. Although the wildfire intensity effect explained more variance than the transport effect, the two effects are comparable.

The fourth EOC of the geopotential height and corresponding geostrophic wind field are shown in Fig.3.4 bottom panel, featured as a low-pressure system centers at north of the NEUS, a high-pressure system in the center of U.S., and a high-pressure system in the southeast of U.S., resulting in near boundary layer winds from WC blow southeastward crossing the great lakes and then blow eastward to the NEUS. This transport pattern resembles the pattern determined by composite analysis (Fig. 3.6), suggesting that this is the pattern that causes the high OC/EC ratio in 2010 and low OC/EC ratio in 2006 and 2015.

It is worth to mention that the two effects are independent and can superimpose or offset each other. As in 2006 and 2015, the special pattern was in negative phase, which weakened the OC/EC ratio while the WC wildfire is strong by resulting northwestward winds anomalies blowing from NEUS to the WC, preventing the WC wildfire pollutants reaching NEUS. In 2010, the wildfire intensity was strong, and the special pattern was in positive phase, the two effects add together, resulting in extra wildfire pollutants reached NEUS and causing the maximum OC/EC ratio in NEUS.

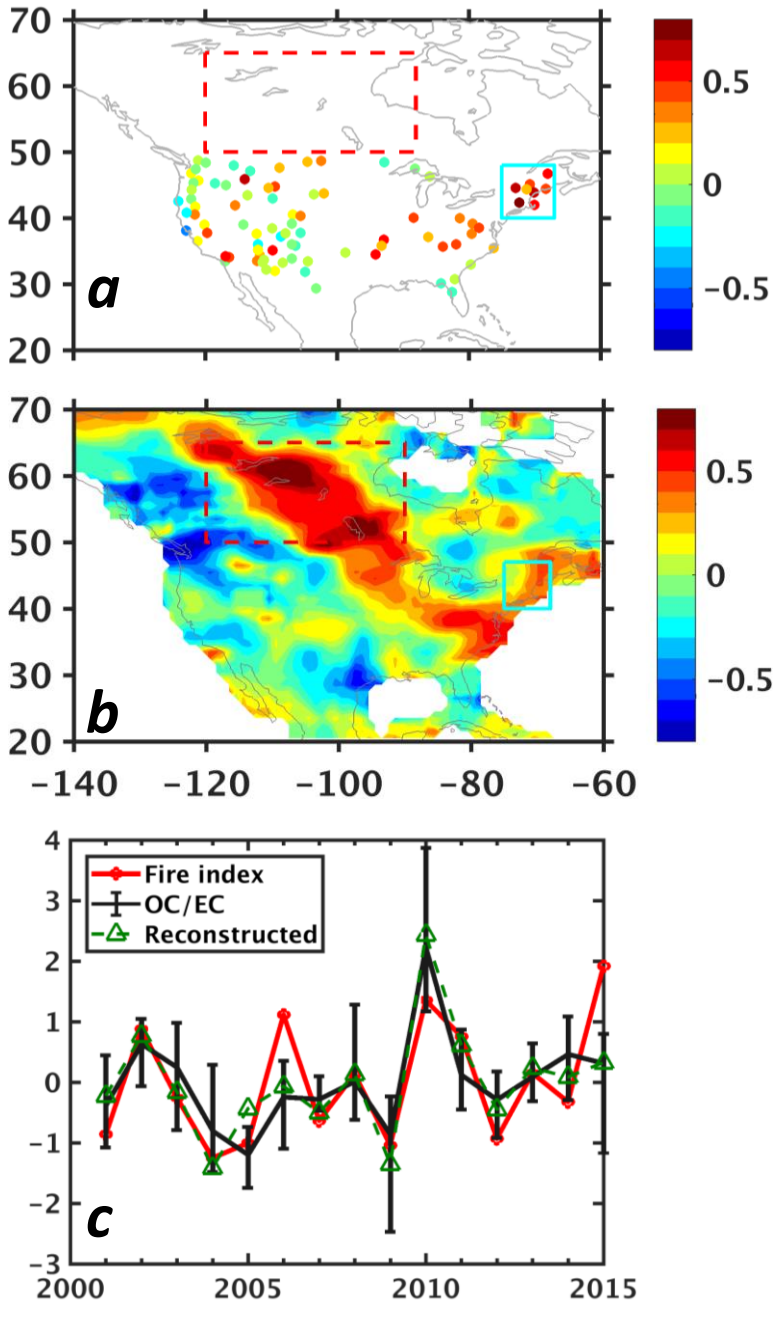
70
60
50
40
30
20
a
0.5
0
-0.5
70
60
50
40
30
20
b
0.5
0
-0.5
-140
-120
-100
-80
-60
4
3
2
1
0
-1
-2
-3
Fire index
OC/EC
Reconstructed
c
2000
2005
2010
2015

Figure 3. 3. The long-term link between the WC wildfires and NEUS air quality in June from 2001 to 2015. The panel *a* is the correlation coefficients between the WC fire index and the OC/EC ratios of IMPROVE sites. The WC region is shown in red dashed box while the NEUS are shown in cyan solid box. The panel b is the correlation between the MODIS AOD and the WCW index. The panel *c* is the normalized temporal variability of the WC fire index, the NEUS regional OC/EC ratio, and the reconstructed OC/EC index. The black line shows the NEUS regional OC/EC ratio (medium) and the upper and the lower bars represent the 10^{th} and the 90^{th} percentile value of OC/EC ratio. The red line is the WC fire index and the green dash line is the reconstructed OC/EC ratio based linear regression model. The correlation coefficient (*R1*) between the WC fire index and the NEUS regional OC/EC ratio is 0.69 and the correlation coefficient (*R2*) between the reconstructed OC/EC ratio and the NEUS regional OC/EC is 0.91.

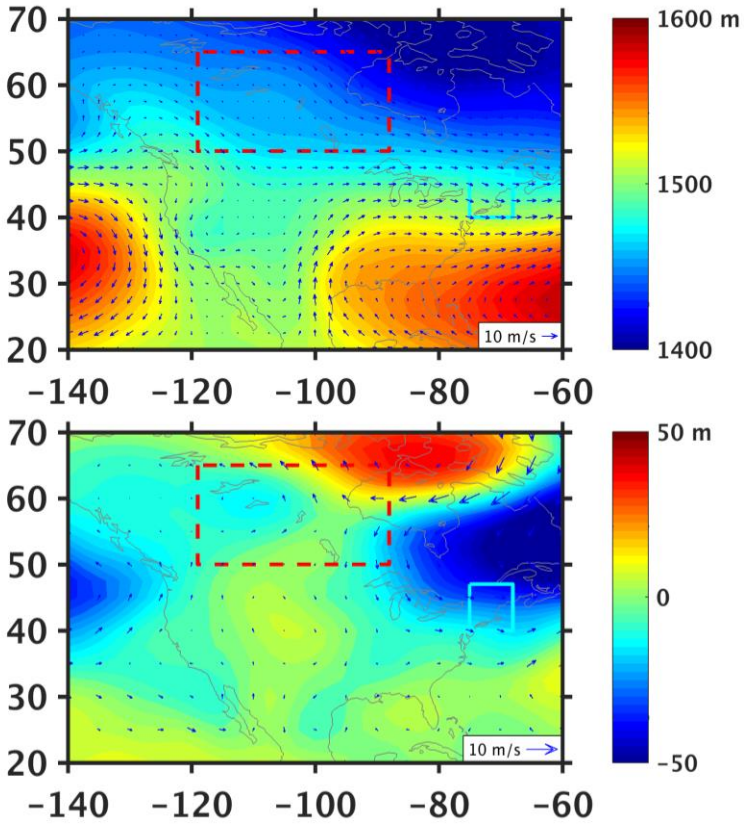

Figure 3. 4. The atmospheric circulation patterns associated with the transport of the WC wildfire pollutants to the NEUS region. The upper panel is the climatology of the geopotential height at 850 mbar level and corresponding geostrophic winds. The color shading represents the geopotential height and the blue arrows represent the winds. The reference of the wind vectors is shown in white box. The bottom panel is the special pattern, which is the fourth EOF of the geopotential height

anomalies at 850 mbar level. The geopotential high anomalies are shown in color and the corresponding winds are shown in blue arrows.

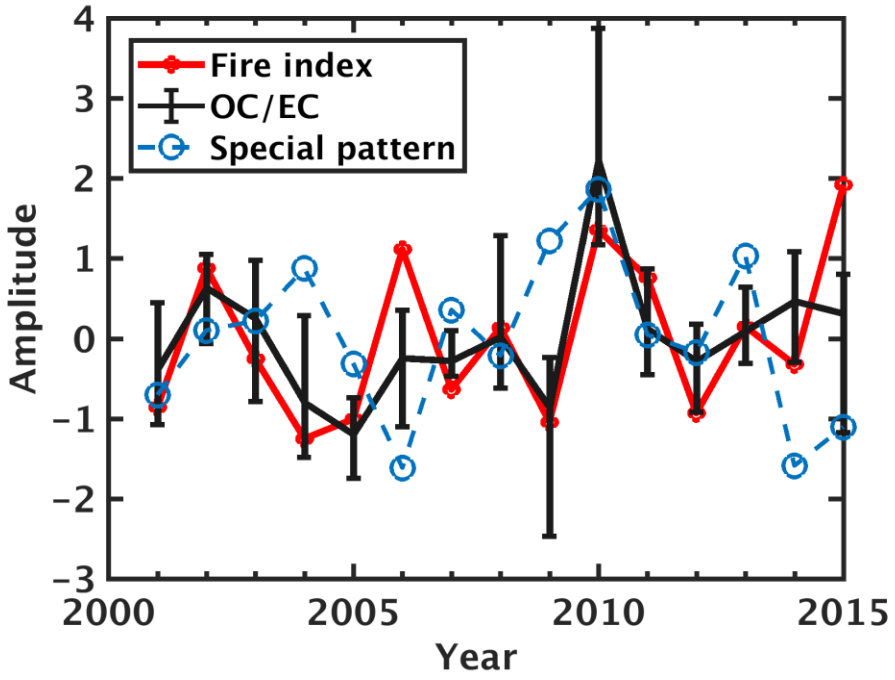

Figure 3. 5. The link between WC fire index, OC/EC ratio and special transport pattern. The x axis is the year and the y axis is the amplitude. The Fire index is normalized.

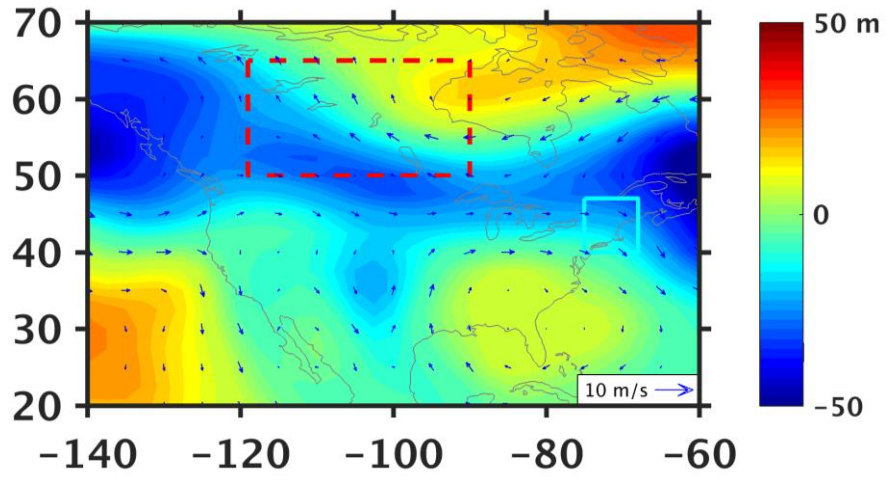

Figure 3. 6. The special transport pattern derived from the composite analysis. The x axis represents longitude while the y axis represents the latitude. The color shading represents the geopotential height anomalies in meter at the 850 mbar level. The red dashed box represents the WC region, while the cyan box represents the NEUS region. The arrows show the geostrophic wind vectors at the same pressure level.

Table 3. 3. The values of correlation coefficients between OC/EC ratios of IMPROVE NEUS sites and regional wildfire indices.

	WC	EC	AK	SU	WU	NEUS
ACAD1	0.44	-0.06	0.22	-0.43	-0.24	0.01
BRMA1	0.50	-0.07	0.02	-0.03	-0.17	-0.19
CABA1	0.62	-0.17	0.02	-0.46	-0.34	-0.38
CACO1	0.59	0.01	0.04	0.2	-0.29	-0.16
GRGU1	0.28	-0.09	-0.41	0.06	-0.07	-0.17
PMRF1	0.64	-0.2	-0.3	0.23	0.02	-0.57
PRIS1	0.52	0.02	-0.19	-0.16	-0.02	-0.18
QURE1	0.81	-0.2	0.01	-0.04	-0.18	-0.56
Medium OC/EC	0.69	-0.12	-0.07	-0.11	-0.19	-0.38

	1	**2**	**3**	**4**	**5**	**6**	**7**	**8**	**9**	**10**
2001	0.58	-0.44	-0.41	-0.11	0.48	-0.63	-0.31	0.47	-0.45	-0.19
2002	0.35	-0.48	0.46	0.14	-0.08	0.28	0.09	-0.38	0.25	0.53
2003	-0.48	0.1	-0.13	0.35	0.23	-0.28	-0.19	-0.19	-0.39	0.19
2004	0.5	0.68	-0.39	-0.37	0.48	-0.27	-0.42	-0.24	0.31	0.23
2005	0.21	-0.39	-0.21	-0.36	-0.35	-0.05	0.78	0.11	-0.43	-0.53

2006	-0.04	0.18	0.19	-0.01	0.24	0.44	0.11	0.2	-0.18	-0.48
2007	0.22	0.51	-0.4	0.15	0.3	-0.26	-0.46	-0.16	0.31	0.03
2008	-0.05	0.3	0.26	0.19	-0.02	-0.13	-0.22	0.23	-0.3	-0.34
2009	0.18	-0.26	-0.42	0.11	0.04	-0.3	0.51	-0.03	0.57	-0.27
2010	-0.39	-0.17	0.41	-0.13	-0.05	0.18	0.09	0.49	-0.26	0

Table 3. 4. The projection values for each member of W-FIRE ensemble

The CAM5 simulation results

Two CAM5 ensemble runs, WO-FIRE and W-FIRE, have been performed to verify the transport caused by the climatology and the special pattern. The simulated ensemble climatology resembles the NCEP climatology featured as the pressure gradient from the WC to the NEUS, resulting geostrophic wind blowing southeastward from the WC to the NEUS (Fig. 3.7). In order to minimize the impact of the east Canada wildfires, seven out of ten years simulation have been analyzed when the east Canada wildfires are weak. The seven selected years are 2001, 2002, 2003, 2004, 2006, 2008 and 2009.

The Fig.3.8 displays the difference between the two ensemble means (W-FIRE – WO-FIRE) of the surface OC concentration and the vertical integrated OC transport. The wildfire emission is the reason to cause the difference. At the WC region, the surface OC concentration is strongest while the concentration at Southeast U.S. and east Canada is weaker. This is caused by the strong biomass burning in WC region and relatively weak burning in Southeast U.S. and east Canada (Fig. 1). The vertical integrated OC transport vectors (Fig. 3.8a arrows) indicated that the wildfire OC emitted from the WC region transport southeastward follow the climatology wind (Fig. 3.7) to the NEUS region, as the transport strength was attenuated alone the distance increase. The surface OC concentration agreed with this feature by showing the enhanced surface OC belt from WC to the NEUS,

implying that it is the primary reason that cause the OC enhanced in the NEUS. The vertical integrated transport arrows show that the vectors are very small from the Southeast U.S. to the NEUS, suggesting the impact of the Southeast wildfires on NEUS is limited compared to the transport from the WCWs. The vectors also shows that the majority of the transport from the east Canada blow to the east coast of Canada while a few could impact the north part of the NEUS, agree with previous studies (e.g. Dreessen et al., 2016; Fiore et al., 2014; Gégo et al., 2007). Overall, the wildfire emission enhanced the OC concentration by 0.95 $\mu g/m^3$ (Table 3.5).

It is worth to mention that this simulation used the original GFED4s emission data, because the purpose of this climate model experiments is to qualitatively verify the effects associated with the WCWs intensity and the special pattern. As suggested by studies, the GFED data underestimates the wildfire emission by 2 to 5 times over North America. Additionally, the MAM3 tends to underestimate the OC and BC transport due to the fast mixing with soluble particles and strong wet deposition process (Liu et al., 2012). Therefore, our simulated OC enhancement are likely to be underestimated.

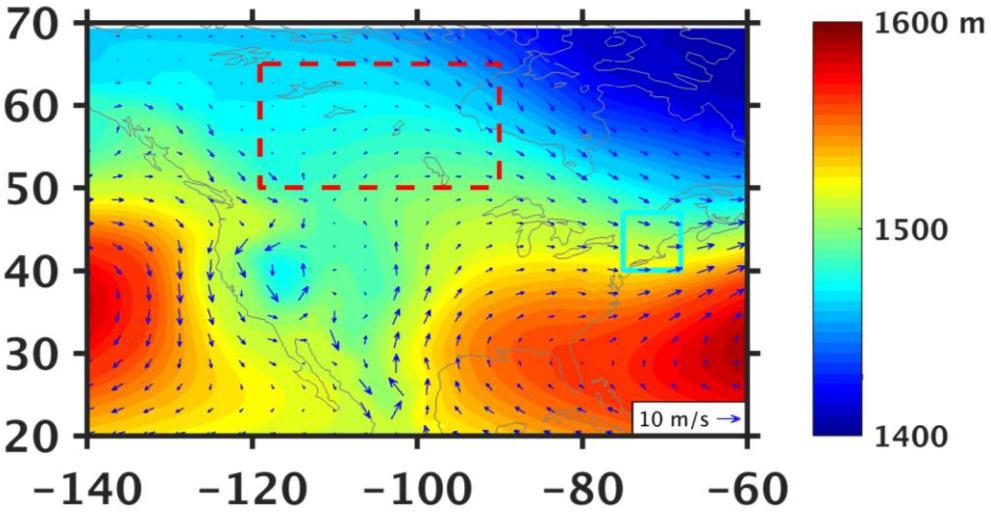

Figure 3.7. The geopotential height at 850 mbar of the ensemble mean of the W-FIRE experiment. The x axis represents longitude while the y axis represents the latitude. The color shading represents the geopotential height and the arrow represents the geostrophic wind at the same pressure level.

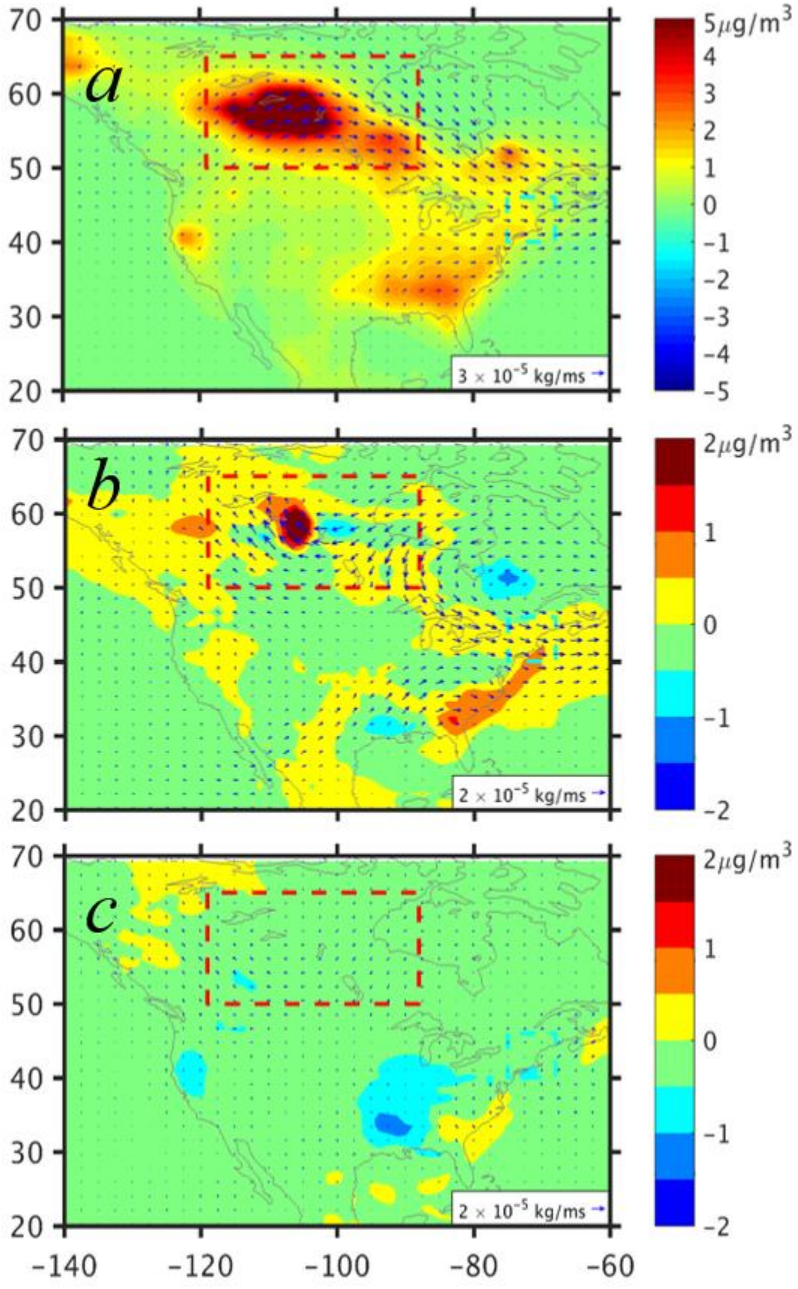

Figure 3. 8. The impacts of atmospheric circulation patterns on wildfire OC transport. The color shading represents surface OC concentration and the values are shown in color bar. The arrows show the vertical integrated OC transport vectors and the references are shown in white boxes. The panel *a* is the OC surface concentration and vertical integrated transport difference between two ensemble means, the W-FIRE ensemble and the WO-FIRE ensemble. The panel *b* is the averaged OC surface concentration and vertical integrated transport anomalies associated with the special pattern for W-FIRE ensemble. The panel c is same as panel *b* but for WO-FIRE ensemble.

Table 3. 5. The surface OC enhancement in NEUS.

	The surface OC enhancement in NEUS ($\mu g/m^3$)
Wildfire emission	0.95
Transport due to the special pattern	0.43

3.3 Conclusion

This study illustrates the significant decadal scale link between WC fire and NEUS OC/EC ratio based on the data from IMPROVE sites and GFED4s burn area in June from 2001 to 2015. Satellite observations of aerosol optical depth (AOD) corroborates this link. Analysis show that the climatology condition of the geopotential height at 850 mbar and corresponding geostrophic wind fields primarily caused this long-range transport. Beside the generally correlated temporal variability between WC fire index and the regional OC/EC ratio indices, a few exceptions motivated the investigation of a special transport pattern, which is the fourth EOF resulted from the EOF analysis of the geopotential height anomalies. Importantly, if the two effects add together, like in 2010, The OC/EC ratio could have a dominant peak. In general, the WCWs intensity explained 48% variance of OC/EC ratio in NEUS, while the transport due to the special pattern explained another 35%. The CAM5 ensemble runs have been performed to verify the two effects. The results clearly show that the OC was transported to the NEUS from the WC region and the surface OC concentration in NEUS increased by 0.95 and 0.48 $\mu g/m^3$, respectively due to the two

effects. Overall, the WCWs intensity has stronger impact on NEUS, while effect due to the transport of the special pattern still comparable to the impact of the wildfire intensity.

Future study is needed to accurately identify the impact of WC on NEUS surface PM2.5 concentration and to evaluate the impact of the climate change on transport effects under changing wildfire emission and climate variability.

CHARPTER4. THE DRIVER OF THE AFRICA WILDFIRE VARIABILITY

The Africa wildfire is responsible for 70% of global burned area and 50% of fire-related carbon emissions (Giglio et al., 2013; Van Der Werf et al., 2010). Therefore, the driver of the Africa wildfire variability obtains research community attentions. Previous studies link the Africa wildfire variability to precipitation change and anthropogenic cropland expansion (Andela et al., 2017; Andela and van der Werf, 2014b; Chen et al., 2016b; Van Der Werf et al., 2008). This study examines the relationships between precipitation, vegetation growth and wildfire, through divided the NHAF and SHAF into arid, intermediate, and mesic regions, suggesting that the fuel availability is an important factor that drives the wildfire variability in most of area of Africa.

4.1 Data and methods

4.1.1 Data

Here we use the fourth version of the Global Fire Emission Database (GFED) burned area product (Giglio et al., 2013) with small fires (GFED4s, (Randerson et al., 2012)). This version combined active fires and burned area observations from the MODIS to provide better estimates of burned area compared to GFED3 version (Randerson et al., 2012) with 0.25x0.25 spatial resolution. For consistency purpose, we only use the monthly GFED4s data from 2001 to 2016, because the data from 1997 to 2001 were collected from

Visible and Infrared Scanner and European Space Agency Advanced Along Track Scanning Radiometer with different approaches (Giglio et al., 2006).

In this study, we define the fire season as the top six most burned months during 2001 to 2016. The fire season in NHAF and SHAF are shown in Fig. 4.1. In NHAF, the fire season is from October to Match in next year, while the fire season is between May to October in SHAF. We define the burned area in a fire season as the mean burned areas in this season. For example, the burned area of 2010 in NHAF is determined by the mean burn from Oct. 2010 to the Match 2011. The six months before the fire season are defined as the preceding wet season, which is used to determine the preceding wet season LAI and precipitation.

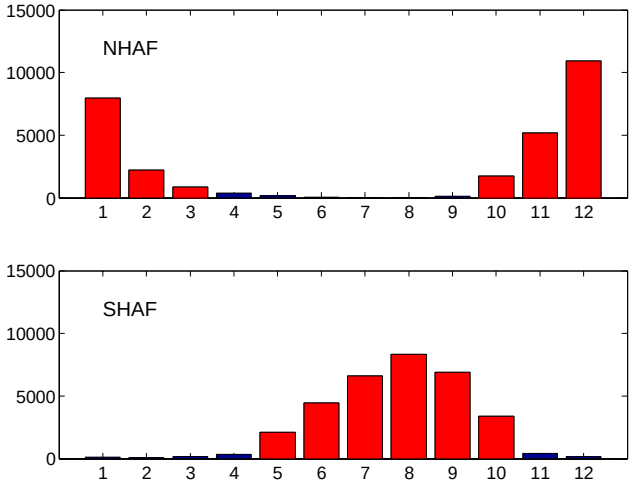

Figure 4. 1. the seasonality in Africa. The x-axis is the calendar months and the y-axis is the burned area in km^2. The upper panel is for NHAF while the lower is for SHAF. The fire season is marked as red**.**

In this study the precipitation data is from the low-earth orbiting Tropical Rainfall Measuring Mission (TRMM) 3B42 product version 7, which provide the daily precipitation

with 0.25-degree spatial resolution (Huffman et al., 2010). The daily precipitation is averaged into monthly time interval.

To represent the vegetation variability, the MOD15A2 MODIS/Terra global Leaf Area Index (LAI) are used. This product has 8-day temporal resolution and 1-km spatial resolution (Tan et al., 2009). The data is first averaged into monthly time interval and then averaged into 0.25-degree GFED4s grids. The LAI in the preceding wet season of each year is calculated to investigate its relationship with precipitation and wildfires in following fire season.

Cloudiness data were from the Climate Forecast System Reanalysis (CFSR) monthly product, with 0.5^{o} x 0.5^{o} horizontal resolution (Saha et al., 2014). The data is linearly interpolated into the GFED4s grid from comparation purpose.

4.1.2 Research domain and region partition

As this paper is discuss the relationship between the wildfire, climate and ecosystem at savanna area in interannually time scale, we remove the grids with low burn fraction (annual burn fraction smaller than 0.01, usually related to forest area) and low relative fire variability. The 'relative variability' is defined as the ratio of standard deviation of annual burn fraction to its annual mean in the period from 2001 to 2016. The results are shown in Fig.4.2. To be noticed, the grid with annual burn fraction small than 0.01 are removed. The Fig.4.2 display that in the most of area of Africa (>90% of effective grids) the relative variability are greater than 0.5. In the north edge of NHAF and south of SHAF, the relative variability is in 2 to 4 range and in the majority of the burned area, the relative variability is between 0.5 to 1.5. Therefore, we set our research domain as the area

where relative variability great than 0.5. Importantly, our research domain includes the area with significant fire trends (Andela and van der Werf, 2014a). The excluded area are central Africa rainforest region, where fire is rare, the regions in SHAF and NHAF, where relative variability is low.

In the defined domain, the mean annual precipitation (MAP) is calculated to separate domain into three regions: arid, intermediate, and mesic regions. When the MAP is small than 516 mm, it belongs to arid region, while when the MAP is greater than 784 mm, it belongs to mesic region. During the 516 to 784 mm, the region is recognized as intermediate region. This partition is based on (Sankaran et al., 2005). From Fig. 4.3, the arid area is located at the north edge of the NHAF and the South of the SHAF, coincident with the area where relative variability value is high.

Though divided NHAF and SHAF into arid, intermediate and mesic regions, the Africa domain are separated as six regions. In each region, wildfire is represented by mean monthly burn fraction during fire season of each year. In NHAF, the fire season is from October to Match, while it is May to October in SHAF. The preceding wet season is defined as the six months before the corresponding fire season. The preceding wet season LAI is the mean monthly LAI in the wet season to represent the ecosystem productivity. The fire season precipitation is the mean daily precipitation in fire season used to represent the fire weather in the fire season, while the wet season precipitation is the mean daily precipitation in the wet season used to represent the water availability in the season when ecosystem growth.

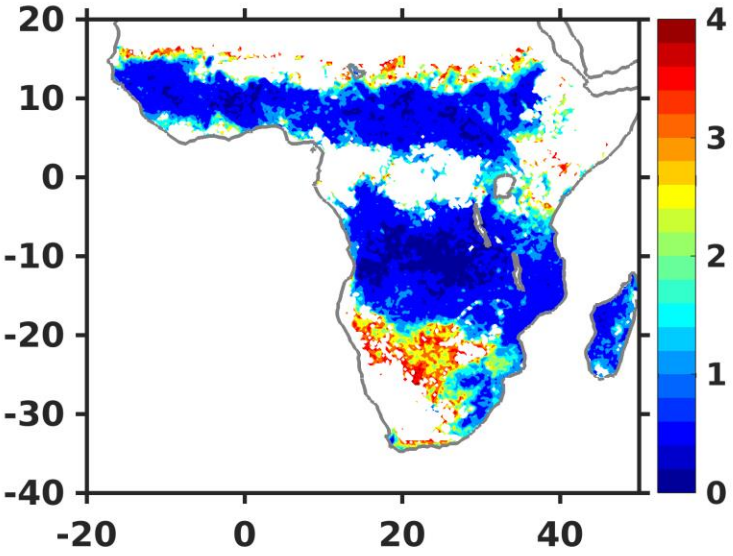

Figure 4. 2. The wildfire variability in Africa from 2001 to 2016. The color shading represents the ratio of the wildfire annual burned fraction standard deviation to its annual.

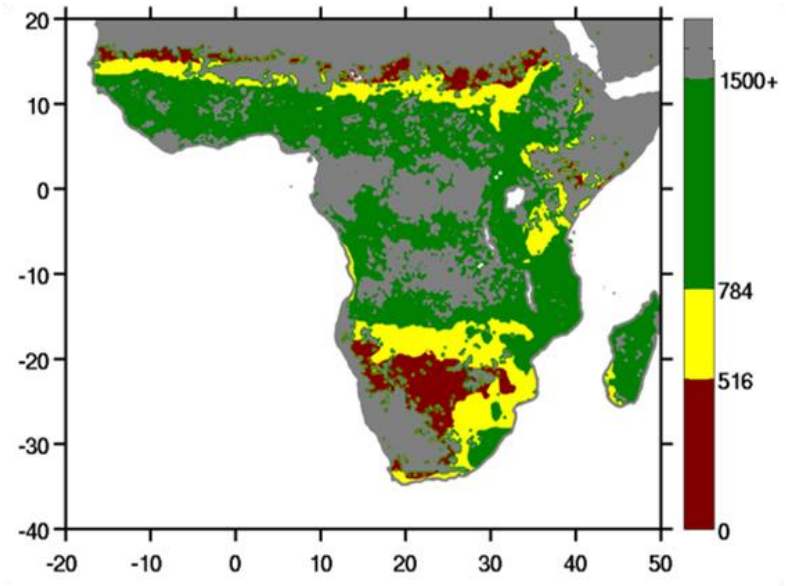

Figure 4. 3. The annual precipitation in Africa**.**

4.2. Results

The timeseries of wildfire, preceding wet season precipitation and preceding wet season LAI are shown in NHAF are shown in **Fig.4.4**. In arid region (Fig.4.4 upper panel), the LAI is tightly related to precipitation with correlation coefficient 0.75 (Table 4.1). This good correlation is expected, because the water is the limitation of the vegetation growth in these region (Sankaran et al., 2005). Also, the wildfire is well related to the LAI with correlation coefficient 0.69 (Table 4.1), suggesting this area is fuel limited. This is agree with previous studies that the increase of precipitations promotes the vegetation growth and then increase the fuel supply, resulting in more fire (Andela and van der Werf, 2014a; Van Der Werf et al., 2008). In mesic region, the water is no longer a limitation of vegetation growth, thus a low correlation between LAI and precipitation is reasonable, 0.32 (Table 4.1). It is interesting that both wet season precipitation and fire season precipitation are not significantly related to wildfire, with correlation coefficients 0.32 and -0.33 (Fig 4. bottom panel and Table 1), suggesting the weak influence of precipitation to the wildfire, similar as previous study (Andela and van der Werf, 2014b). However, the wildfire is significantly related the LAI in this region (correlation coefficient 0.67), suggesting the fuel-limitation still controls the wildfire trend in mesic area.

In SHAF, the relationship between LAI and wildfire are tighter (Fig.4.5). In arid region, the precipitation increase from 2001 to 2011 and then decrease from 2012 to 2016, which is related to the ENSO effect (Andela and van der Werf, 2014b; Chen et al., 2016a). The LAI follow precipitation with correlation coefficient 0.76. Also, the correlation between wildfire and LAI is significant (0.81). In the mesic region, the wet season precipitation is no long impact the LAI and wildfire and the fire season precipitation also

has little impact on wildfire. However, the wildfire still tightly related to LAI, with correlation coefficient 0.80.

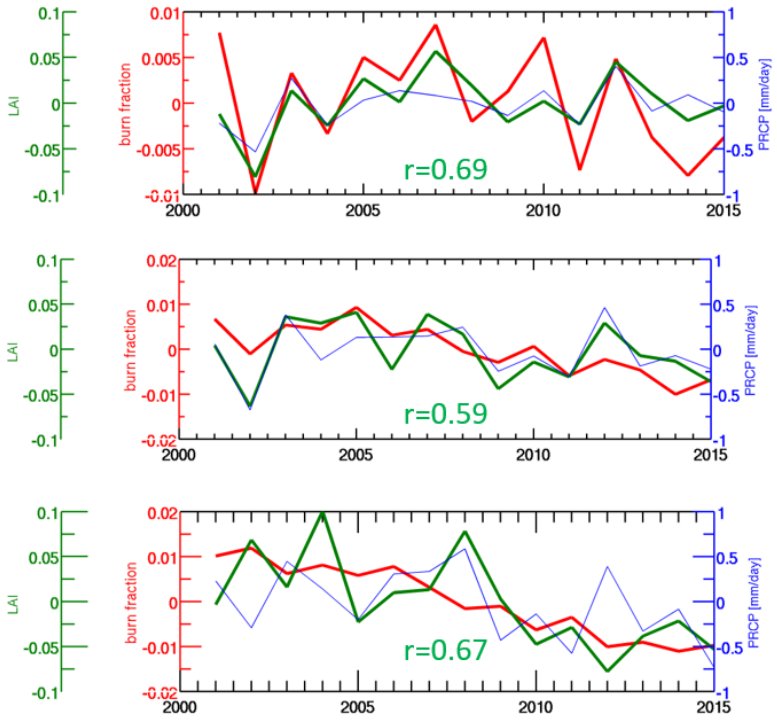

Figure 4. 4. The wildfire, wet season LAI, and wet season precipitation timeseries in three regions in NHAF: arid, intermediate, and mesic from top to bottom. The red, green and blue lines represent averaged burn fraction, LAI, and precipitation, respectively.The climatology mean of the variables are removed.

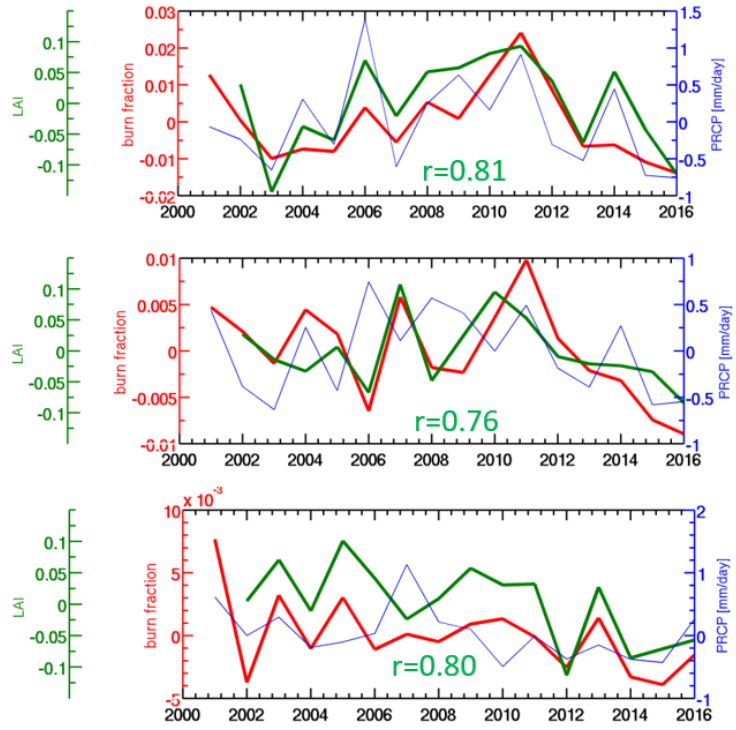

Figure 4. 5. Same as Fig 4.4 but for SHAF.

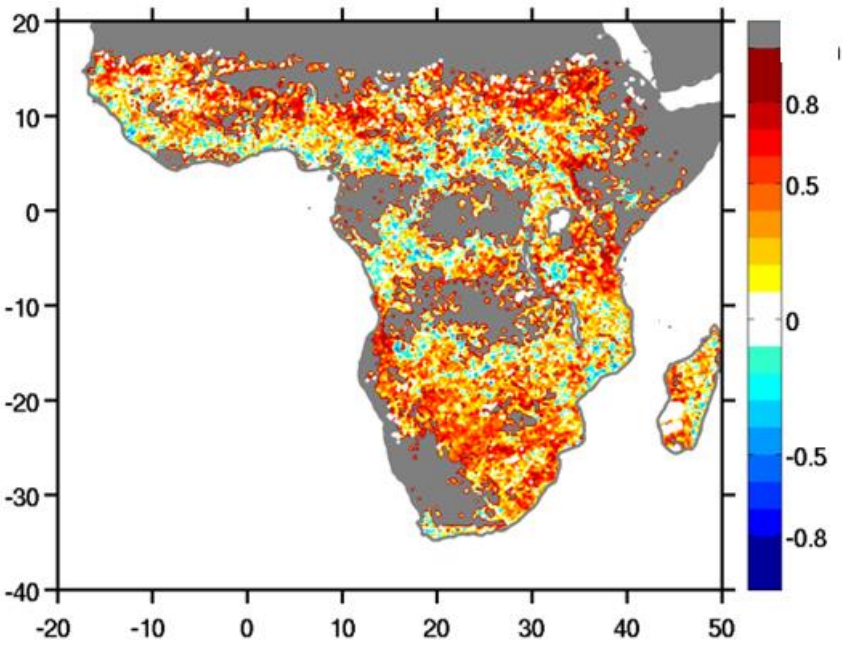

Figure 4. 6. The correlation between LAI and wildfire.

Table 4. 1. The correlation coefficients between wildfire, LAI, and climate factors. The N1, N2 and N3 represents arid, intermediate, and mesic regions in NHAF. The S1, S2 and S3 represents arid, intermediate, and mesic regions in SHAF.

Correlation	**N1**	**N2**	**N3**	**S1**	**S2**	**S3**
Fire vs. PRCP in wet season	0.57	0.41	0.32	0.62	0.24	0.27
Fire vs. PRCP in dry season	-0.50	-0.29	-0.33	0.07	0.17	-0.12
Fire vs. LAI in wet season	0.69	0.59	0.67	0.81	0.76	0.80
LAI vs. PRCP in wet season	0.75	0.82	0.35	0.76	0.08	0.19
LAI vs. cloudiness in wet season	0.33	0.09	-0.52	0.48	-0.10	-0.55

4.3 Conclusion

In summary, the LAI significantly related to the wildfire in all three regions in both NHAF and SHAF (Table 4.1 and Fig.4.6), suggesting fuel limitation is the key factor to

control wildfire in Africa. This is agreed with previous study (Griffin et al., 1983). It is easy to understand in the arid area, where vegetation growth is limited by precipitation. In the mesic regions, the weak correlations between LAI and precipitation are expected by the definition of mesic region. A possible factor to impact the LAI is the cloudiness. The correlation between LAI and the cloudiness in mesic area in NHAF and SHAF are all significant -0.52 and -0.55. The long-term satellite observation since 1982 show the vegetation growth in Africa mesic region is primarily related to the cloudiness (Neami et al., 2003; Seddon et al., 2016). In the wet season, the increasing cloudiness could attenuate the strength of surface solar radiation and then reduce the photosynthesis of plant. The similar effect on LAI was also observed in Amazon (Myneni et al., 2007).

CHARPTER5. THE WILDFIRE'S FEED BACK TO LANDCOVER CHANGE

This study present new evidence about the fire-forest interaction, by analyzing the MODIS landcover data and the GFED burned area data. The results show significant lag correlations between the burned area and the forest amount in both hemisphere Africa savanna area during 2001 to 2012, with correlation coefficients -0.56 and -0.75. It motivates the investigation to what extent the fire suppression could promote the reforestation and reach the RCP4.5 forest landcover target in Africa by 2100. An ecosystem model (Staver-2011, see section 1.4) has been modified to include the fire-forest feedback explicitly, the land patch interaction and capable to be driven by the change of the fire. The model forced by current fire reproduced the current landcover in Africa with correlation coefficient value 0.8. Ensemble runs have been performed with broad range of parameter values, suggesting that 90% of the fire needs to be reduced compared to 2005 level to reach the RCP4.5 forest landcover target in 2100.

5.1 Data and methods

5.1.1 Research domain

Our first research domain is the mesic region in Africa where the bistability can be support. The MAP is between 1000~2000 mm and the elevation is small than 1000 m (Staver et al., 2011a). The precipitation data used in this study is form the Climate Forecast System Reanalysis (CFSR) products, which are atmosphere-ocean`-land surface-sea ice coupled reanalysis datasets developed by National Centers for Environment Prediction

(NCEP) for climate studies, featured as high spatial (0.25^o x 0.25^o) and temporal resolutions (6-h) from 1979 to present (Saha, et al., 2010; Trenberth et al., 2010). For this study, we choose the monthly mean total precipitation data from 2001 to 2014 to calculate the MAP. The elevation data is also from CFSR with same spatial resolution. The research domain is shown in Fig. 5.1. As shown the domain includes the mesic area in both north and south hemisphere Africa but excludes the equator rainforest area. Additionally, the cropland identified by MODIS land cover data are excluded, the details about the land cover data are described in section 5.1.3.

5.1.2 Burned fraction

In this study we use the fourth version of the Global Fire Emission Database (GFED4) burned area product (Giglio et al., 2013) with monthly temporary resolution and 0.25^o spatial resolution. This product is derived from 500 m Collection 5.1 MODIS direct broadcast burned area product (MCD61A1) since 1997.

We calculate the total wildfire burned area during its fire season for each grid in the domain determined by the MAP and elevation. The fire season is the top six most burned months based on the 1997-2012 monthly burning climatology. The fire season in North Hemisphere Africa (NHAF) is from October to March in next year and is from May to October in South Hemisphere Africa (SHAF). By adding up the burned fraction during the fire season, the annual burned fraction is obtained in each grid box. The linear trend of the annual burned fraction of each grid box is calculated. Chosen this period is because the available landcover data is from 2001 to 2012 and there may be a time lag of the forest respond to the fire. The trend is shown in Fig.5.1. As shown, there is a clear negative trend

in the north hemisphere part while the trend is positive in the south hemisphere Africa. These trends are consistent with the previous studies (Andela and van der Werf, 2014b; Van Der Werf et al., 2010). The relationship between the burn fraction and the forest amount is described in section 5.2.

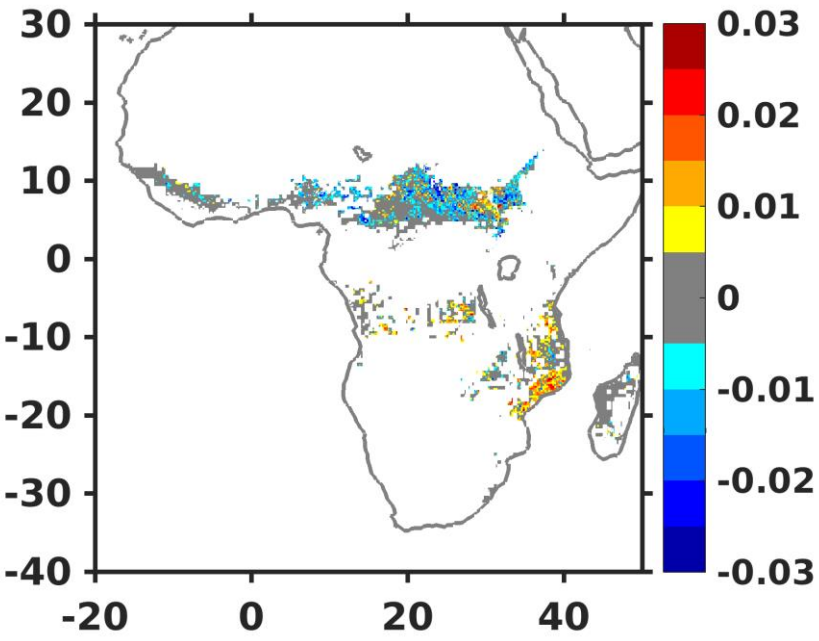

Figure 5. 1. The burned fraction trend in bistability domain. The x-axis is the longitude and the y-axis is the latitude. The color shading represents the trend in unit fraction per year. The absolute trend values less than 0.005 are marked as gray.

5.1.3 Land cover data

The MODIS Collection 5 Land Cover product MCD12Q1 in the IGBP (International Geosphere-Biosphere Program) classification provide the annual land cover information from 2001 to 2012. This data is reprojected into geographic coordinates of latitude and longitude on the WGS 1984 reference system with 5' x 5' resolution (Channan et al., 2014). The data provides 17 landcover types including five forest classes (evergreen

needleleaf, ever- green broadleaf, deciduous needleleaf, deciduous broadleaf, and mixed forests), two savanna classes (woody savannas, savannas), one grassland class, and one cropland/natural mixed vegetation mosaic. The forest classes are grouped together to define the “forest”, as they all have the woody vegetation with stature greater than 2m (Li et al., 2017). The savanna, grassland and the cropland/natural mixed classes are grouped together to define the “savanna” in this study. As we focus on the relationship between the fire and the forests, the annual forest area in the domain are counted by using the forest pixels multiplying the pixel area. The mean landcover types (forest and savanna) between 2001 to 2012 are shown in Fig. 5.2. As shown, the domain are mostly covered by the savanna with a little forest in each hemisphere.

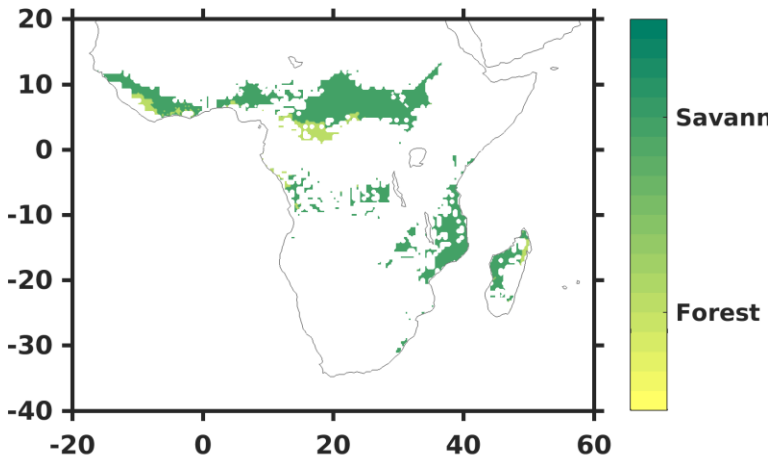

Figure 5. 2. The mean landcover type between 2001 to 2012 in domain as Fig.5.1

5.1.4 Model modification

To drive the Staver-2011 (see section 1.4) model by using fire burned fraction, the $\omega(G)$ function are converted to $\omega(f)$, where f is the burned fraction in each grid. In equation (5), the ω_3 and ω_4 are the tree sapling

$$\omega(f) = \omega_3 + \frac{\omega_4 - \omega_3}{1+e^{-(f-\theta_2)/s_2}} \tag{5.1}$$

recruitment rate at high fire region and low fire region, respectively. The θ_2 is the burned fraction threshold to separate the two regions. Here we assume that the majority of the lands are forests under the threshold value while the majority shifts to savanna when the fire is above the threshold. Therefore, the model domain is defined as the MAP above 1000 mm and the elevation smaller than 1000 m in Africa. The landcover based on the MODIS landcover data average in this domain is shown in Fig. 5.3. As shown, this domain includes the previous bistability domain and the equator rainforest area.

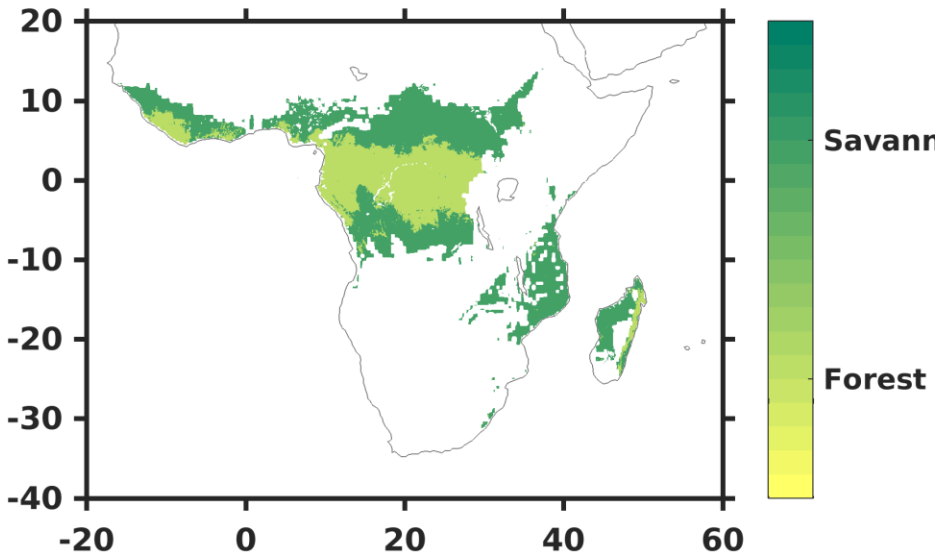

Figure 5. 3. The landcover in the model domain**.**

We calculate the correlation relationship between the landcover shown in Fig.5.3 and the 'assumed' landcover determined by the threshold value θ_2. By moving the θ_2 from 0.001 to the 0.5, the correlation coefficients against the θ_2 are shown in Fig. 5.4. As shown, the correlation coefficients have a peak when θ_2 equals 0.01. This also keeps consistency with the Staver-2011 model, which set the forest-savanna threshold at grass fraction equals to 0.4, means 40% grass and 60% trees. This is also the value in MODIS landcover data to determine the forest pixels. In other words, there is little fire effect in the forest while fire's impact on ω is significant in non-forest grids. Therefore, our $\omega(f)$ (equation 5.1) can be shown in similar manner and is displayed in Fig. 5.5. The ω value is higher when f smaller than 0.01 while the value decrease sharply when f is above 0.01. Through equation (5.1), the

Staver-2011 model can be driven through the burn fraction instead of the grass fraction *G*. Through this change, the fire is explicitly represented in the model as an independent variable instead implicitly as the grass fraction's side effect in Staver-2011. Studies through the worldwide wildfire regions has shown the wildfires are driven by climate factors (Chen et al., 2016c; Pechony and Shindell, 2010; Randerson et al., 2012) and human impacts (Andela et al., 2017; Andela and van der Werf, 2014b), rather than determined by the grass fraction. The advantage of this modification is that the new model is capable to investigate the landcover change resulted from the wildfire variability no matter the causes of the changes. Here we define the modified model as 'fire-forest model', including equation (1.1), (1.2), (1.3) and (5.1).

Through modifying $\omega(G)$ to $\omega(f)$ described above and applying the fire-forest model to the two-dimension gridded domain as shown in Fig 5.3. The model could be used to study the landcover in Africa mesic region. The equations are rewrite as (5.2)~(5.5). This is our fire-forest model without patch interactions.

$$\omega(f) = \omega_1 + \frac{\omega_1 - \omega_2}{1 + e^{-(f-\theta_2)/s_2}} \tag{5.2}$$

$$\frac{dG}{dt} = \mu s + \nu T - \beta G T \tag{5.3}$$

$$\frac{dS}{dt} = \beta G T - \omega(f) S - \mu s \tag{5.4}$$

$$\frac{dT}{dt} = \omega(f) S - \nu T \tag{5.5}$$

However, the interactions between the adjacent patches are also important (Staal et al., 2016; Wuyts et al., 2017b) to determine the landcover in local and continental scales. If a grass dominant patch is close to a tree dominant patch, the tree seeds can transport between the patches and enhance the tree sapling birth rate in the grass dominant patch. In the other side, the grass patch with high fire activity can increase the fire activity in the tree dominant patch to decrease the tree sapling recruitment. Therefore, the patch interaction can be expressed as the tree and fire gradient between adjacent patches. The modified equations (5.6) to (5.10) are shown below and the equation (5.2) are shown again for the reading convenience:

$$\frac{dG}{dt} = \mu s + \nu T - \beta G T' \tag{5.6}$$

$$\frac{dS}{dt} = \beta G T' - \omega(f')S - \mu s \tag{5.7}$$

$$\frac{dT}{dt} = \omega(f')S - \nu T \tag{5.8}$$

$$T' = d\nabla T + T \tag{5.9}$$

$$f' = d\nabla f + f \tag{5.10}$$

$$\omega(f) = \omega_1 + \frac{\omega_1 - \omega_2}{1 + e^{-(f-\theta_2)/s_2}} \tag{5.2}$$

In the equations above, the tree sapling birth is impacted by T', which is determined by the tree gradient in adjacent grids $d\nabla T$ and the original T and the recruitment function $\omega(f')$ is impacted by the f', which is determined by the fire gradient $d\nabla f$ and original f in this grid. The value d is suggested as 0.1 by Wuyts et al. (2017b) through an semi-empirical

model tested in Amazon. Here we have the option in the fire-forest model with and without interactions. We define this model as fire-forest model with patch interactions.

5.1.5 Numerical experiment design

Because our observational results display the suppressed fire activity could promote the forest amount in continental scale, it motivates the following investigation, by using the ecosystem model that explicitly including the fire-forest feedback, about the extent of the forest management (fire suppression) by which the forest growth could reach the RCP4.5 target in Africa by 2100. To reach the goal, we firstly modified the Staver-2011 model to convert it to be driven by fire forcing. Although this model is computational effective with clear fire-forest mechanism, the parameter values are unclear. As we focus on the forest growth in savannas, we only focus on the parameter sets, which could support the both grasses and forests. Parameter sets are tested in three experiments with different model configuration. The first experiment is configured as original Staver-2011 model. The second experiment tests the parameter sets by using the fire-forest model modified from the Staver-2011 model, which can be directly forced by the fire. The third experiment tests the parameter sets by using the fire-forest model with patch-interaction included. After obtained appropriate parameter values, we perform the model under different fire reduction scenarios to determine which scenario can best match the RCP4.5 forest pathway in Africa.

In equations discussed above, the parameter β, ν, μ, ω_1, and ω_2 are undetermined, and the nonlinear effect and burfication effect increase the complexity of the model (Touboul et al., 2017). As there is no literature gives the recommend parameter values, three experiments are designed to determine the parameter sets that could support the

bistability in the Africa and experiment results are used discuss the bistability's dependence on the parameter values. Because these parameters are a ratio of a certain subject, this study give each parameter a value range from 0.01 to 0.91 with a 0.1 interval. Therefore, each parameter has ten values and the total combination number is 10,000. Also, the ω_1 value has to be greater than ω_2, that reduces total combination to 45,000. All these 45,000 parameter sets are applied to each ensemble experiments.

The first experiment is to apply all the 45,000 parameter sets to Staver-2011 model, equation (1.1)-(1.4) over Africa model domain shown in Fig.5.3. The spatial resolution is 0.25 degree as GFED4 resolution and the temporal resolution is 1 year. The model initial condition is the random grass fractions over all the domain grids and the Staver-2011 equations are calculated in each grid independently. It worth to note that all the members have the same initial condition. Every member performs the calculation for 2000 years to reach the equilibrium state. For each grid, we define the forest is the tree plus the sapling fraction greater than 60%, otherwise the grid is defined as the grass. The definition is same as in (Touboul et al., 2017). If the whole domain are all forests, we defined the result as forestland. If the whole domain are all grasses grids, we define result as grassland. If the whole domain contains both grass and forest grids, we define it as bistability land. By adding up all 45,000 results, we could discuss which parameter sets led to which states. The results are shown in section 5.2.

The second experiment is similar as the first one, but applies the parameter sets to equations (5.2)~(5.5), the fire-forest model without interaction. The initial condition, domain and parameter sets are as same as the first experiment, but the model is forced by the fixed fire, which is the annual mean burned fraction of each grids from 2001 to 2012

period. Each member also performs 2000 years to reach equilibrium. The results are used to compared to the first experiments to characterize the impact of the fire forcing on their final states. The results are shown in section 5.2.

The third experiment is designed to understand the impact of the interaction. The parameter sets, initial condition, domain, and fire forcing are same as second experiment, but are applied to the equation (5.6) to (5.10). The effect of the patch interactions can be discussed by the comparison between the second and third experiment results.

The four RCP scenarios give the pathway of the landcover change in tropical forests and the RCP4.5 is the only pathway requires the forest increase through forest management. By assuming the forest management can effectively suppress the fire in the Africa, which is true over North America and East Asia (Li et al., 2017; Liu et al., 2010), here we design experiments to investigate what extent of the fire suppression could increase the forest coverage to reach the RCP4.5 target at the end of the 21st century. As recent burned area decrease, around 30% in total from 1997 to 2016, did not lift up significant forest amount, we design three scenarios that reduce the forest amount by 70%, 80% and 90% in ten years and compared the results with the RCP4.5 forest pathway. These three scenarios are applied to both fire-forest model without and with the interactions. The fire-forest model is forced by the 2005-fire burn fraction for 2004 model years to reach the steady state and then forced by the fast reducing fire from 2005 to 2014 in model years and keep the reduced fire forcing from 2016 to the 2100 model year. The parameter sets are obtained from the experiment 2 and 3, which can obtain the bistability in both model results. The six ensemble results from two models configurations (with and without

interaction) and three scenarios (70%, 80% and 90% reduction) are presented in section 5.2. All the experiments are summarized in table 5.1.

Table 5. 1. The Numerical Experiments Summary

Experiment Name	Configuration
Parameter test1(PT1)	Test all parameter sets by using Staver-2011 model
Parameter test2(PT2)	Test all parameter sets by using Fire-Forest (FF) model
Parameter test3(PT3)	Test all parameter sets by using Fire-Forest-Interaction (FFI) model
RCP70	Reduce fire by 70% in first ten years (FF and FFI models)
RCP80	Reduce fire by 80% in first ten years (FF and FFI models)
RCP90	Reduce fire by 90% in first ten years (FF and FFI models)

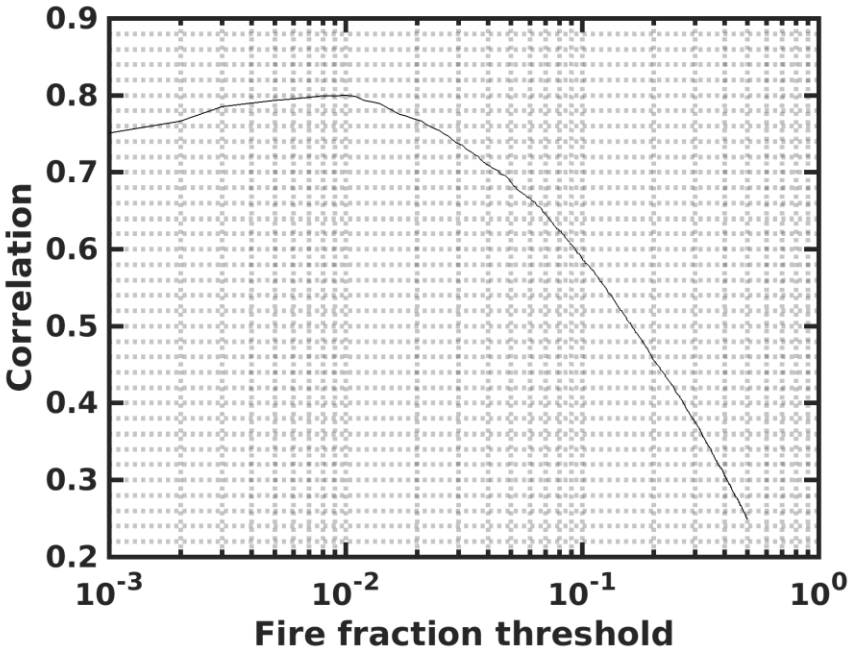

Figure 5. 4. The correlation between the MODIS landcover and the assumed landcover determined by the $\boldsymbol{\theta_2}$. The x axis is the $\boldsymbol{\theta_2}$ value and the y axis is the correlation coefficient.

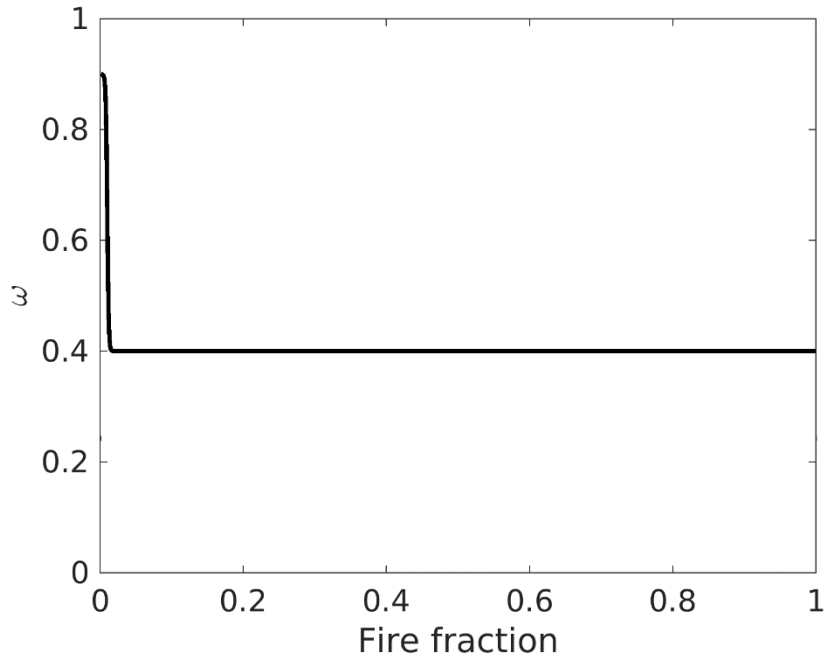

Figure 5. 5. The $\boldsymbol{\omega}$ value as a function of fire fraction. In this case, the $\boldsymbol{\omega_3}$ and $\boldsymbol{\omega_4}$ are 0.9 and 0.4, respectively, as same as in Fig.1 and the s_2 value is 0.001.

5.2 Results

5.2.1 The relationship between observed wildfires and forests

As shown in Fig.5.1, the fires in Africa displays different trend in different hemispheres. In NHAF, the mesic region with fire activities distributes along the latitude between 5 to 13 N^o. This agrees with the view that the NHAF precipitation has strong gradient along latitudes (Sankaran et al., 2008). In this region, most grids show the negative trends except a little exceptions in the east part, while in the SHAF, the region distribution is less regular and shows positive trends, agreeing with previous studies (Andela and van der Werf, 2014b; Van Der Werf et al., 2010). In these regions, climate condition can support forests growth, but it does not reach its maximum, probably due the fire-forest feedback (Staver et al., 2011c).

We investigate the relationship between fires and forests by calculating their correlation coefficients in NHAF and SHAF. As there is time lag between the fire activity and its impact on forest growth, the lag correlations are calculated from fire led 4 years, which is 1997-2008 fire vs. 2001-2012 forest, to fire behind 2 years, which is 2003-2014 fire vs. 2001-2012 forest. The results are shown in Table 5.2. In the NHAF the fire is clearly led four years while in the SHAF the fire is more likely led by 1 year. In NHAF, the burned area is calculated from October to Match of the next year, thus the actual fire led is less than 4 years. The timeseries of the two best lag correlations are shown in Fig.5.6. In the Fig.5.6, the NHAF total burned area shows a negative trend reducing from 6.3 to 5.8 $x10^{11}$ km^2, while the forest area shows a positive trend increasing from 1.26 to 1.32 $x10^{11}$ km^2.

In the contrast, in the SHAF region the total burned area shows a positive trend increasing from 2.2 to 2.7 x10^{11} km^2, while the forest area shows a negative trend reducing from 7.4 to 5.1 x10^{10} km^2. In summary, the fire and the forest display opposite trends in both region and the correlation coefficients are both negative and significant. Because studies show the savanna trees are fire tolerant and fire rarely kill savanna trees and saplings (Bond and Midgley 2001, Hoffmann et al. 2009, Schutz et al. 2009), the negative correlations are caused by the fire-forest feedback. Importantly, this result gives new evidence of the fire-forest feedback in continental scale and suggests that it may be detected in interannually time scale.

Table 5. 2. The lag correlation between fires burned area and forest area in NHAF and SHAF. The positive time lag means fire led while the negative lag means forest led. The red color means correlation coefficients are significant.

Time Lag	4	3	2	1	0	-1	-2
NHAF	-0.56	-0.25	-0.42	-0.1	-0.44	-0.2	-0.37
SHAF	-0.23	-0.56	-0.49	-0.75	-0.31	-0.49	0.19

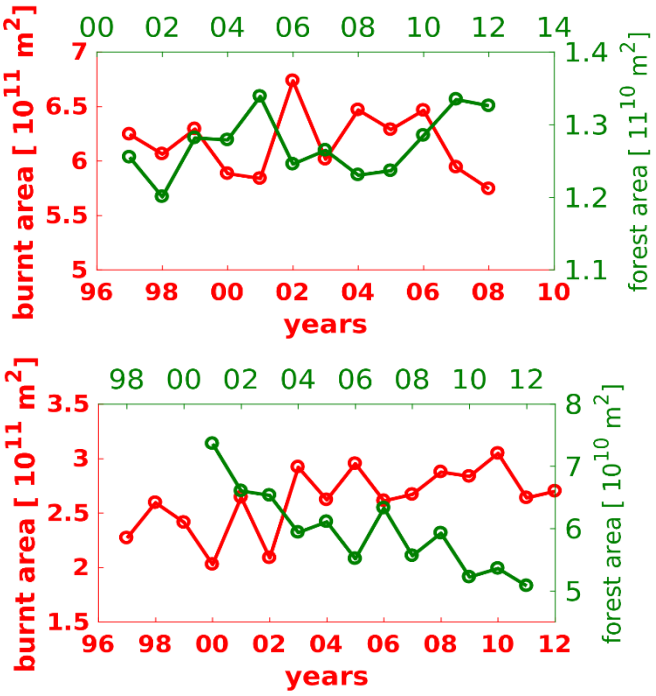

Figure 5. 6. The observed relationship between the wildfires and forests in Africa mesic region. The red x-axis represents the year of the fire and the red-axis represents the burned area. The green x-axis represents the year of forest detected and the green y-axis represents the forest area amount. The upper panel is the results of NHAF and the bottom panel is the results of SHAF area.

5.2.2 The model results

The observational results display the suppressed fire activity could promote the forest amount in continental scale. This motivates the following investigation, by using the ecosystem model that explicitly including the fire-forest feedback, about the extent of the forest management (fire suppression) by which the forest growth could reach the RCP4.5 target in Africa by 2100. To reach the goal, we firstly modified the Staver-2011 model to convert it to be driven by fire forcing. Although this model is computational effective with clear fire-forest mechanism, the parameter values are unclear. As we focus on the forest

growth in savannas, we only focus on the parameter sets, which could support the both grasses and forests. The way to generate the parameter sets is described in section 5.1.5. In general, 45,000 parameter sets are tested in three experiments with different model configuration. The first experiment is configured as original Staver-2011 model. The second experiment tests the parameter sets by using the fire-forest (FF) model modified from the Staver-2011 model, which can be directly forced by the fire. The third experiment tests the parameter sets by using the fire-forest model with patch-interaction (FFI).

The number of parameter sets that supports different states from three experiments are shown in Table 5.3. From Table 5.3, there is no significant difference between the three experiments. Around 85% parameter sets results in grassland, 10% goes to forests and only around 5% parameter sets support the savanna, the bistability. The numbers in the parentheses are results without significant burfication disturbance. We calculate the standard deviation for the last 100 years of each member and compared the value to its mean during the same 100 years period. If the ratio is small than 0.01, this member is defined as no significant disturbance. Because the nonlinear effect in the model equations, diverse cyclic behavers of the Staver-2011 model are detected and the causes and consequences of these behavers are still unclear (Touboul et al., 2017). As the purpose of this study is not to discuss these nonlinear effects, the members with significant disturbance are excluded. After this process, 1945, 2135 and 2272 members with little disturbance impact are chosen for the three experiments, Staver-2011, FF, and FFI, respectively. This impact is not significant, because less than 10% members are excluded.

Table 5. 3. The number of the parameter sets supporting different final states

Exp. Name	Forest	bistability	Grassland
Staver-2011	4688	2174(1945)	38138
FF	4604	2251(2135)	38145
FFI	4703	2361(2272)	37936

The mean of the final tree cover ratios of three states from three experiments are shown in Fig. 5.7. It is worth to mention that the initial condition for three experiments are the same: the grass ratios in the domain is random distributed. The models are driven into three states category due the prescribed parameter values, which is agreed with previous studies (Staver et al., 2011c; Staver and Levin, 2012; Touboul et al., 2017). Through all three models, the results can be categorized into grasslands, bistability and forests. In Fig.5.7 (a, d and g), all the grassland means have low tree cover ratio, less than 0.2, while the forests category (Fig.5.7c, Fig5.7f, and Fig5.7i) shows high tree cover ratios, over 0.8. In the bistability category (Fig.5.7b, Fig5.7e, and Fig5.7h), both forests and savanna lands can be supported, which has an intermediate tree cover ratio between 0.3 to 0.4. These values are agreed with the observations of tree cover in Africa (Aleman et al., 2018; Staver

et al., 2011b). As this paper focus on the bistability in Africa, which is the current Africa state, our discussion will narrow to the bistability category.

Because the random initial condition and there is no spatial climate attractor in all the models, the Staver-2011 model keeps the random feature in its final mean, which is evident in the Fig.8b. In this plot, the high tree cover, 0.8 to 1, mixed with the intermediate tree cover, 0.3 to 0.4, randomly (Fig. 8b). This caused by the implicit fire mechanism is the Staver-2011 mode, where fire strength is determined by the grass fraction in each individual grid. Unlike the Staver-2011 model results, the Fire-Forest model, with and without interaction, gives the clear savanna and forest boundary (Fig.5.7e and h), with correlation coefficient around 0.8 compared with the MODIS land cover data in same domain (Fig. 5.3). In FF model results, the central Africa rainforest has a tree cover ratio at 0.78 while the savanna tree cover ratio is 0.41 (Fig.5.7e). When the interaction between the patches are added in, the two ratios are 0.75 and 0.40. This suggests that the fire forcing separates the rainforest and the savanna in Africa effectively, giving the evidence that the potential of the fire to shape the Africa landscape. In the FF result, there is some high tree cover spots, above 0.7, random distributed in the savanna region in both north and south hemisphere (Fig.5.7e), while these high tree cover hot spots disappeared in the FFI bistability category results (Fig.5.7f). This suggests that interactions between the patches driving the results to the more dominant direction and making the savanna and the forest boundary shaper by reducing the local scale bistability condition (Staal et al., 2016).

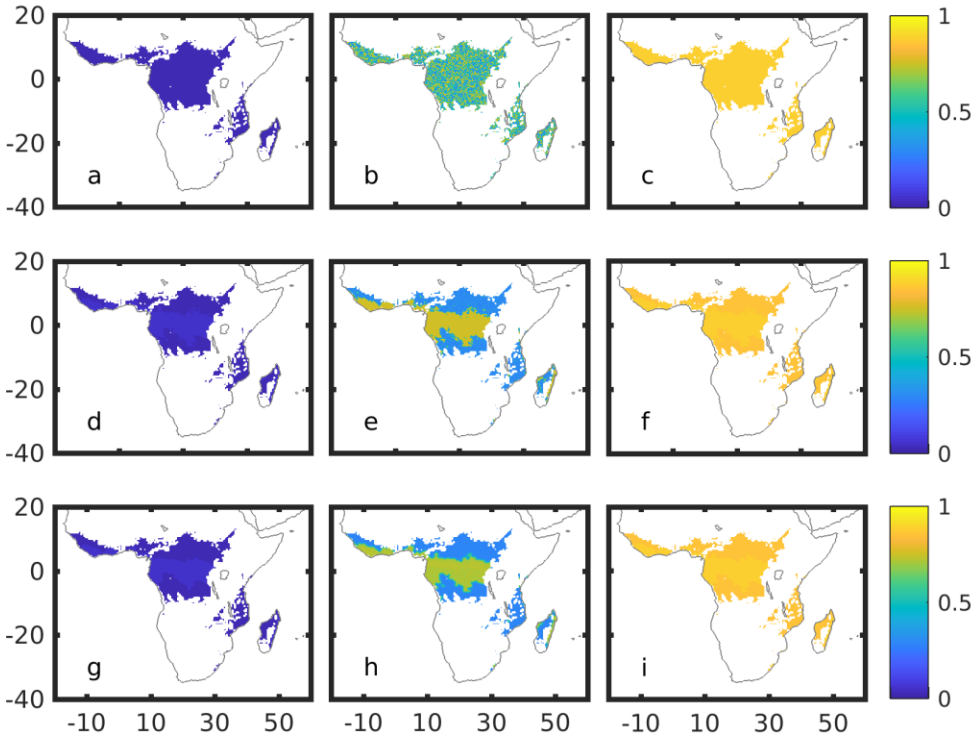

Figure 5. 7. The mean of the final tree cover ratios for three states from three experiments. The first column is the mean of the members resulting in grassland, the second column is the mean of members resulting in bistability, and the third column is the mean of the members resulting in forests. The a to c is the results from Staver-2011 model, the d to f is the results from the Fire-Forest model, the g to i is the results from the Fire-Forest-Interaction model.

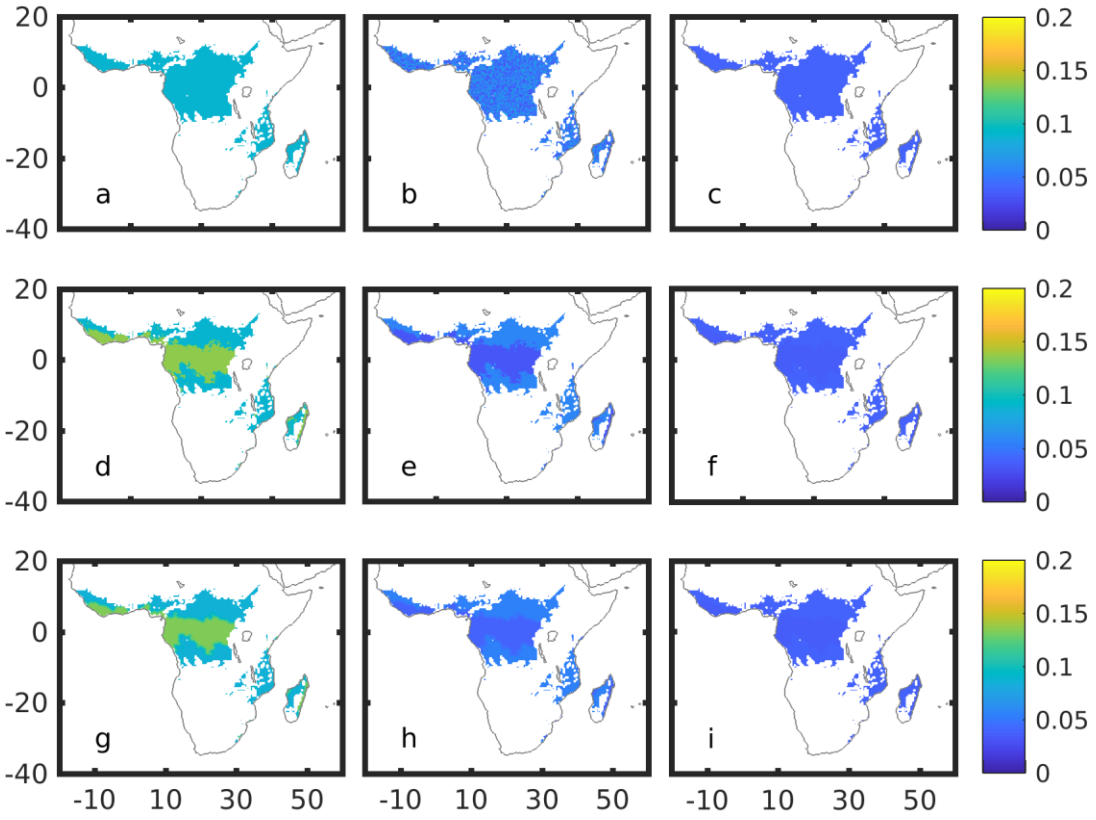

Figure 5. 8. Same as Fig.5.7 but for the standard deviation.

For each model, we tested 45,000 parameter sets based on five parameters: β, ν, μ, ω_1 and ω_2, as well as the $\omega_1 - \omega_2$ value to test if the difference of the two recruitment rates could impact the bistability. The tested value for each parameter is from 0.01 to 0.91, with 0.1 interval. The parameter's dependence of the three models in the bistability category is shown in Fig. 5.9~5.11. In general, all the three models have the similar parameter dependence. The most important parameter is ν, the death rate of the trees. When

b is over 0.4, there is no member results fall in bistability category and the majority bistability members fall in 0 to 0.2. Only less than 500 members produce bistability in total 2174 members. This is reasonable that when tree death rate is high, the forest is hard to form and the whole domain drives to the grassland. The second parameter limits the bistability is the ω_2, which is the recruitment of the sapling trees in the low grass region (G>0.4). When it is greater than 0.7, there is no bistability results and more than half of the members appear in when ω_2 smaller than 0.1. The possible explanation is that when the ω_2 value is big, the system, especially the savanna area, recruit too many trees, resulting in the whole domain shift to the forest only situation. Another parameter clearly impacts on bistability is the ω_1, the recruitment rate of the sapling tree in the low grass region. Higher the ω_1 value, higher possibility to produce the bistability case. This higher ω_1 value can yield more trees, which makes the bistability more possible especially when the ω_2 value is low. The impact of the difference between the two recruitment rates was shown in Fig7.f, there is no significant dependence on the difference of the two values. The parameter β, the birth rate of the tree saplings, increase the possibility of bistability when its value grows greater. There is no clear dependence on the death rate of the sapling trees, μ, unless it is very small (<0.1), it could lead to the forest state. In summary, the ν is most important, and the β, ω_1 and ω_2 also influence the possibility, while the μ, and the difference between the two recruitment rates have no clear impact on the bistability.

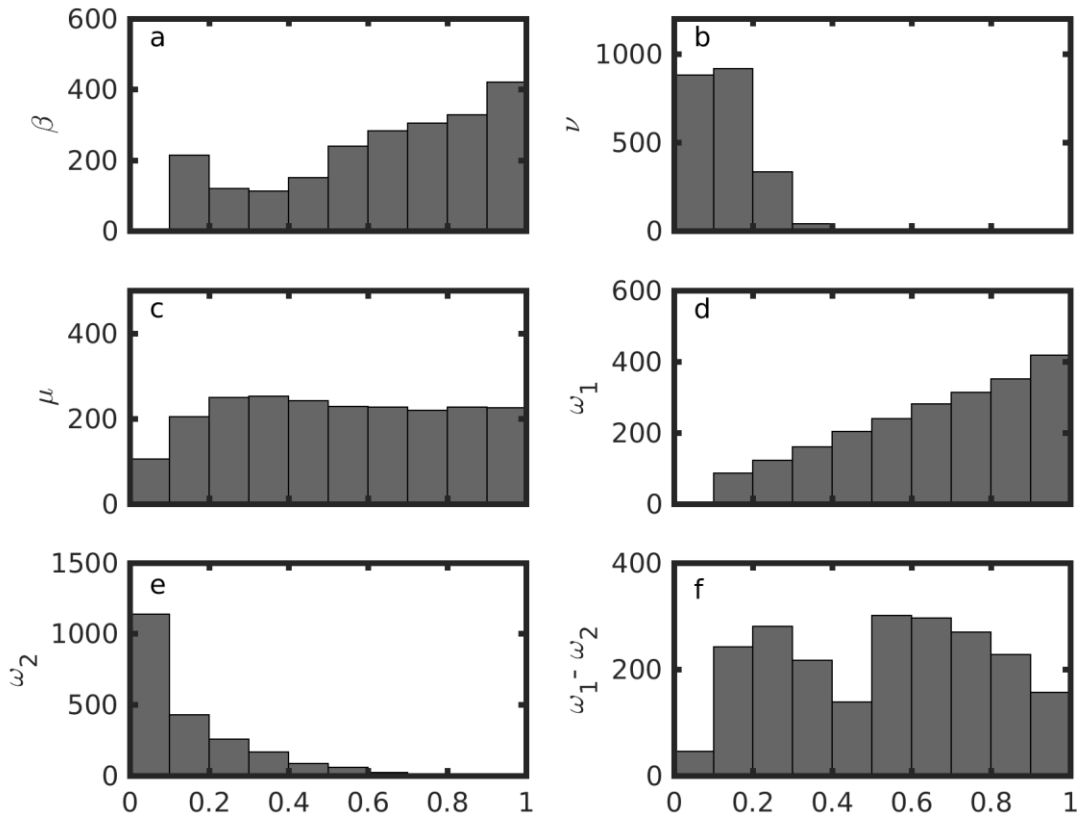

Figure 5. 9. The parameter dependence of the bistability category for the Staver-2011 model results. The panel a is the number of the members fall in the bistability category as the value of the parameter $\boldsymbol{\beta}$. The panel b, c, d, e, and f are the same but for the parameter $\boldsymbol{\nu}$, $\boldsymbol{\mu}$, $\boldsymbol{\omega_1}$, $\boldsymbol{\omega_2}$ and $\boldsymbol{\omega_1 - \omega_2}$.

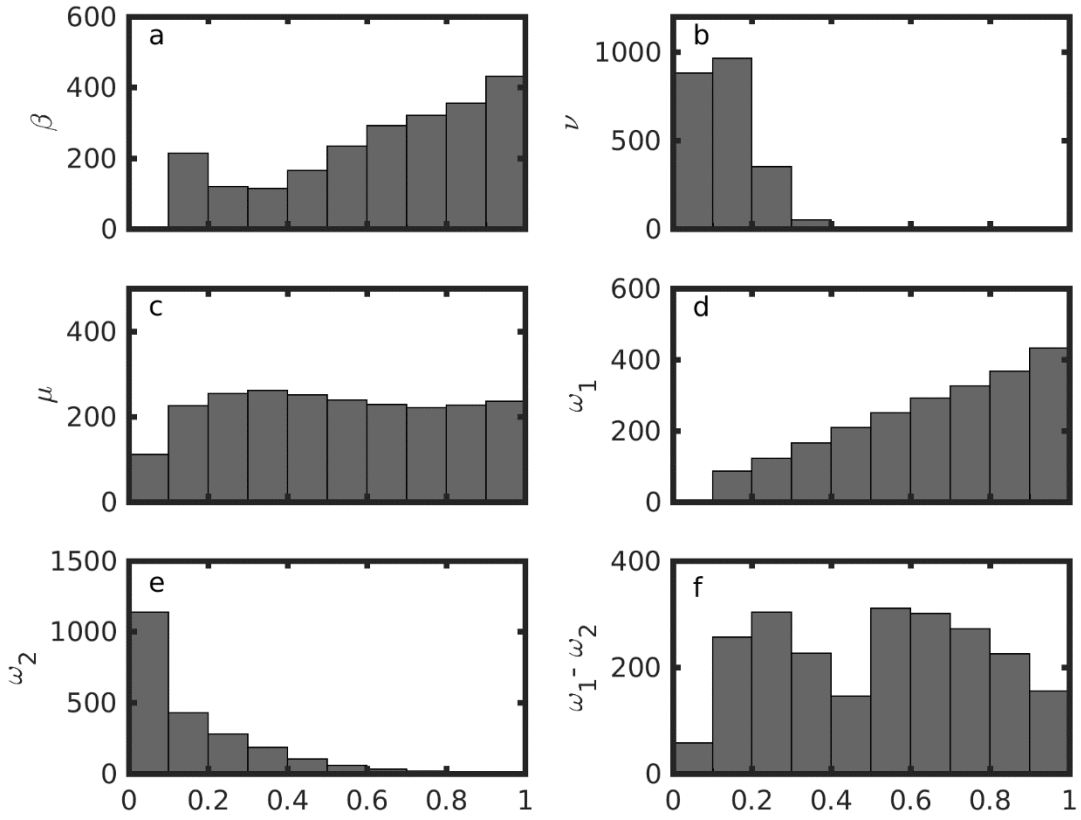

Figure 5. 10. Same as Fig.9 but for the Fire-Forest model results in bistability category.

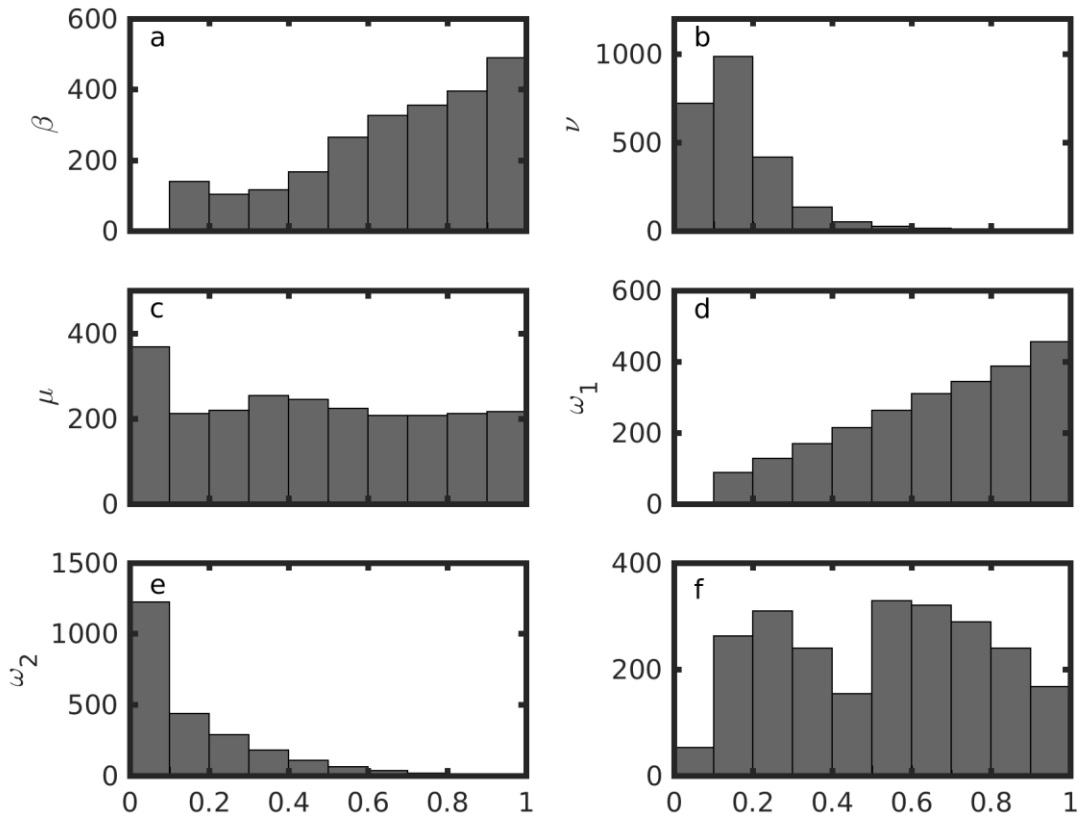

Figure 5. 11. Same as Fig.9 but for the Fire-Forest-Interaction model results in bistability category.

After examined the parameter dependence to the bistability, the common parameter sets that lead to the bistability in both FF and FFI cases (1969) are chosen to perform the RCP4.5 experiments. Choosing a broad range of parameter is to obtain the ensemble means that is under a varying range of climate conditions. A drier climate situation that leads more tree mortality and less birth of tree sapling could result in more savanna than forest, while a wet climate could leads more tree than savanna by suppress the tree mortality and increase the tree sapling birth rate. These climate oscillations can be represented by the different parameter sets. The ensemble mean under a broad range of parameter sets can give valid results that immunes the climate fluctuations, when it still in the range to support the bistability in Africa.

The RCP4.5 is the only pathway that requires the increase of the forest in Africa to reduce the atmospheric CO_2 concentration through the forest management (LAWRENCE et al., 2012). Fire suppression is one of the forest management method to increase the forest amount (Liu et al., 2014). Recently, Africa experiences around 30% fire reduction in 20 years (Andela et al., 2017), but the forest amount has no significant increase (Aleman et al., 2017), suggesting current fire decrease is not strong enough to promote the forest amount. Therefore, three wildfire suppress pathways are designed to discover which could be best to increase the forest amount to the RCP4.5 target. The proposed pathways require to reduce the fire by 70%, 80% and 90% in ten years, respectively. The three pathways are examined in FF and FFI models.

Before running the six experiments, we need to check the models' capability of detecting the forest variability in multi-decadal time scale. We examined the mean correlation coefficients between the mean MODIS landcover data and the simulated landcover in each time step of each member in bistability category for both FF and FFI experiments. The results are shown in Fig.5.12. As the model initial landcover is random distributed, the mean correlation at the beginning is zero. However, the correlation increases sharply to 0.5 in first 20 years in both experiments, suggesting the significant role of fire to shaping the landscape. After that, the correlation increase gradually and reach the peak around 0.8 in less than 110 years. Because this process is an exponential process, we define a variable as 'resembling time' by using the radiation lift time definition. Thus the 'resembling time' is defined as the time that the model results reach the half of their peak correlation. The resembling time for the FF model mean is around 23.4 years while it is 19.2 years for FFI model mean. This means the FF and FFI model are both capable to capture the response of landcover in multi-decadal time scale, and the FFI model has quicker response than the FF model.

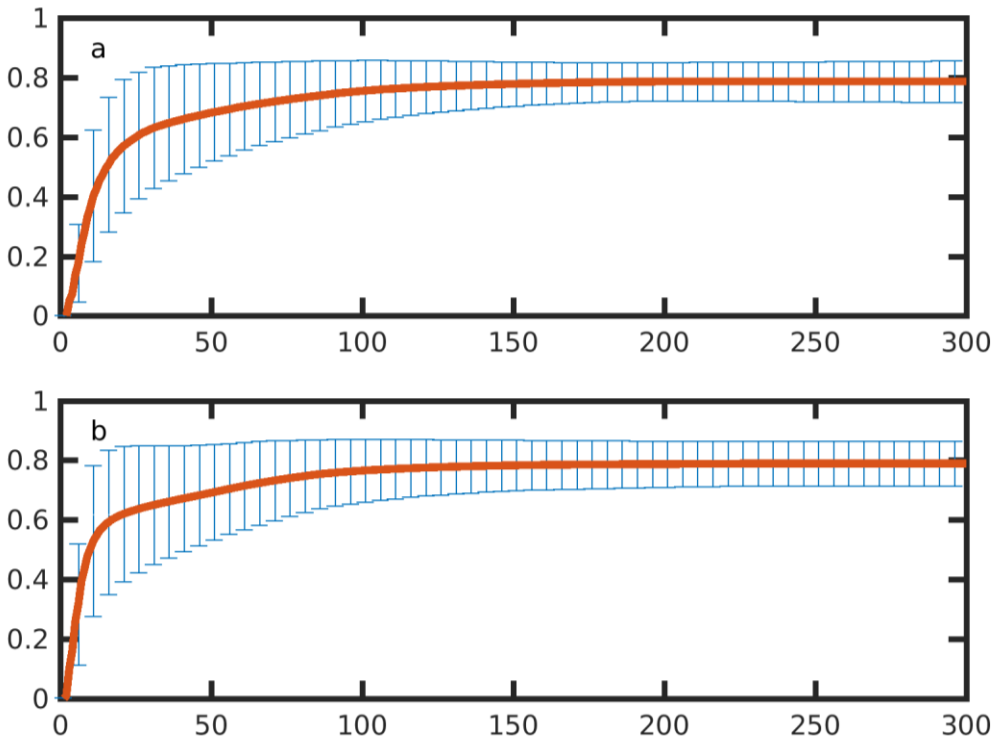

Figure 5. 12. The mean correlation coefficients at each time step between the mean MODIS landcover and the member simulated landcover for FF and FFI experiments. The panel a is the FF experiment results and the panel b is for the FFI results. The x-axis is the simulation time and the y-axis is the correlation coefficients. The lines show the mean and the error bar is the standard deviation at each time step.

These six resulted timeseries of the forest amount in our Africa domain are shown in Fig.5.13. The results show the FFI model simulates larger forest change than FF model under same fire suppression pathway. This is agreed with previous study that suggests the interaction could accelerate change of the landcover to the dominant direction (Staal et al.,

2016). The discrepancy between the two models increase as the fire reduction increase. From Fig.13, the forest amount increases as the fire reduction increase, and only the 90% reduction of fire can reach the forest increasing target at 2100 under FFI simulation. The 70% reduction of fire only resulted in around 20% forest increase. This may be a reason that the current fire reduction (around 30%) does not produce significant reforestation in observation. However, the fire suppression is one of the forest management practice, the reforestation can not only rely on fire suppression

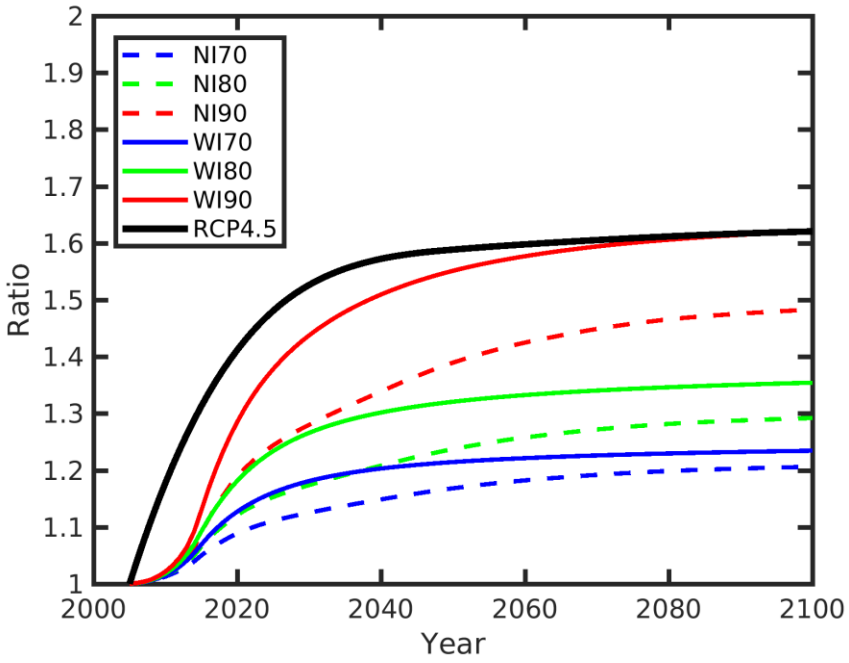

Figure 5. 13. The comparison between the RCP4.5 forest landcover pathway and the model results. The blue, green and red color represent the fire reduction at 70%, 80% and 90% compared to the 2005 level. The solid line is the results from FFI model, and the dashed line is the results from FF model. The change of the forest is shown as the ratio of simulated results to the 2005 forest amount.

5.3 Conclusion

The bistability is a mechanism to explain the observed discontinuous tree cover distribution in tropical region. Fire plays an important role in the bistability ecosystem. Though suppressing the tree sapling recruitment, the fire is recognized as a disturbance to shaping the forest and grass distribution. By analyzing the MODIS landcover data and the GFED burned area data, new evidence about the fire-forest interaction is present in this study. The results show a good correlation between the burned area and the forest amount in Africa savanna area. During 2001 to 2012, the forest increase in NHAF can be explained by the observed fire reduction, while the forest decreases in SHAF resulted from the fire increase in the region. The correlation coefficients are significant and the burned area leads the forest change. It motivates the investigation about the extent of the forest management (fire suppression) by which the forest growth could reach the RCP4.5 target in Africa by 2100. To reach the goal, we firstly modified the Staver-2011 model to convert it to explicitly including the fire-forest feedback. The modified model can be driven by fire forcing and includes the interactions between the patches. Additionally, the model's dependence on parameters are investigated, suggesting the tree mortality rate, tree sapling birth rate and the sapling recruitment rate are import parameters to determine the bistability state. By choosing a wild range of parameter sets that lead bistability, ensemble runs are performed to determine which fire reduction scenario can reach the RCP4.5 forest increase target at the end of 2100. The results show only when the fire is reduced by 90% the RCP4.5 can be reached. This result suggested that fire suppression alone is hard to achieve the reforestation target and other forest management method are needed.

APPENDIX A. THE MFRP TABLE

Table A1.a The values as a function of regions and PFT in January.

Regions / PFTs	BONA	WTNA	ETNA	CEAM	NHSA	SHSA	EURO	MIDE	NHAF	SHAF	BOAS	CEAS	SEAS	EQAS	AUST
PFT1	599	769	0	0	0	96	417	0	0	0	166	123	0	0	0
PFT2	294	365	609	1046	1298	453	179	528	1815	504	644	1106	1087	2129	761
PFT3	0	5027	1150	37	1927	364	336	477	993	3	825	181	0	1436	976
PFT4	244	2201	1185	562	1047	787	161	753	984	65	647	581	97	1928	1004
PFT5	227	752	528	433	669	259	785	560	1161	260	601	384	1276	1777	805
PFT6	0	444	70	0	496	0	257	350	156	0	695	146	0	2150	0

Table A1.b The MFRP values as a function of regions and PFT in February.

Regions / PFTs	BONA	WTNA	ETNA	CEAM	NHSA	SHSA	EURO	MIDE	NHAF	SHAF	BOAS	CEAS	SEAS	EQAS	AUST
PFT1	469	1494	0	0	0	278	0	0	0	0	1071	0	0	0	186
PFT2	582	1044	981	999	1271	615	46	553	1847	635	795	1291	877	2440	754
PFT3	0	783	1309	67	1645	154	1182	542	1215	443	430	189	0	1787	375
PFT4	78	1294	786	611	969	1050	161	713	1114	142	1100	642	164	1724	936
PFT5	543	1923	566	559	661	415	628	597	634	594	614	470	1256	1899	1080
PFT6	0	144	0	0	737	0	265	735	158	0	867	742	0	1035	0

Table A1.c The MFRP values as a function of regions and PFT in March.

Regions / PFTs	BONA	WTNA	ETNA	CEAM	NHSA	SHSA	EURO	MIDE	NHAF	SHAF	BOAS	CEAS	SEAS	EQAS	AUST
PFT1	386	1432	0	0	0	1410	0	0	0	676	926	713	0	0	204
PFT2	341	472	745	623	952	902	144	780	1122	745	977	1709	806	1837	876
PFT3	56	1443	1731	28	2053	1160	661	570	1077	204	830	388	0	1231	469
PFT4	161	1066	888	641	817	1230	810	722	944	972	946	1063	371	1678	947
PFT5	218	1318	620	527	775	677	493	591	1122	1605	775	924	1098	1235	965
PFT6	55	225	253	0	239	0	251	559	154	0	538	608	33	31	0

Table A1.d The MFRP values as a function of regions and PFT in April.

Table A1.d The MFRP values as a function of regions and PFT in April.

Regions / PFTs	BONA	WTNA	ETNA	CEAM	NHSA	SHSA	EURO	MIDE	NHAF	SHAF	BOAS	CEAS	SEAS	EQAS	AUST
PFT1	787	764	0	0	0	233	0	0	0	1178	1161	259	0	0	0
PFT2	751	965	883	549	1155	480	0	774	939	1046	1318	1520	981	1469	952
PFT3	0	1631	1882	70	2076	620	300	896	1452	1121	906	413	0	1272	30
PFT4	314	1983	919	728	635	688	408	1295	1604	1274	1029	928	445	969	1092
PFT5	717	751	782	553	501	565	454	727	717	923	835	747	705	763	796
PFT6	52	372	424	0	459	642	249	385	0	0	1248	429	0	203	0

Table A1.e The MFRP values as a function of regions and PFT in May.

Regions / PFTs	BONA	WTNA	ETNA	CEAM	NHSA	SHSA	EURO	MIDE	NHAF	SHAF	BOAS	CEAS	SEAS	EQAS	AUST
PFT1	2275	1847	0	0	0	375	0	0	0	1125	1135	79	0	0	106
PFT2	2287	578	745	1805	1030	362	0	355	2441	1256	1727	1358	883	1140	2211
PFT3	1302	1861	1751	66	501	1074	346	807	955	1021	913	221	0	1094	665
PFT4	1667	1716	620	1132	813	962	486	1373	653	1278	1408	784	268	746	1712
PFT5	1066	961	697	319	616	332	365	632	544	888	1248	335	706	872	827
PFT6	1675	134	180	0	158	1346	209	473	172	1654	434	208	0	32	0

Table A1.f The MFRP values as a function of regions and PFT in June.

Regions / PFTs	BONA	WTNA	ETNA	CEAM	NHSA	SHSA	EURO	MIDE	NHAF	SHAF	BOAS	CEAS	SEAS	EQAS	AUST
PFT1	2098	2783	0	0	0	575	126	0	0	1217	469	269	0	0	69
PFT2	2526	305	679	452	1875	1086	196	218	951	1379	1238	896	904	861	966
PFT3	1660	2277	1295	60	542	3438	756	408	1256	1055	454	486	0	1275	467
PFT4	2137	2865	618	1060	1297	2500	863	624	1083	1092	1192	532	830	633	837
PFT5	2201	2198	470	355	1326	630	509	411	892	1249	355	336	887	929	988
PFT6	2222	446	634	0	325	0	231	3174	1236	1234	289	184	0	169	0

Table A1.g The MFRP values as a function of regions and PFT in July.

Regions / PFT	BONA	WTNA	ETNA	CEAM	NHSA	SHSA	EURO	MIDE	NHAF	SHAF	BOAS	CEAS	SEAS	EQAS	AUST
PFT1	2196	2002	0	0	0	2768	1393	0	0	1142	348	111	0	0	177
PFT2	1362	627	462	642	2050	1411	288	235	1469	1033	655	589	727	781	762
PFT3	1867	2354	1316	107	1640	963	846	256	1285	1105	475	160	0	1319	450
PFT4	1718	2197	506	523	1262	1680	1059	398	1294	1046	949	479	302	748	1079
PFT5	555	1449	439	400	1057	889	620	413	928	1703	736	473	618	509	1066
PFT6	667	561	412	0	358	0	223	1311	594	728	483	231	0	68	0

Table A1.h The MFRP values as a function of regions and PFT in August

Regions / PFTs	BONA	WTNA	ETNA	CEAM	NHSA	SHSA	EURO	MIDE	NHAF	SHAF	BOAS	CEAS	SEAS	EQAS	AUST
PFT1	2245	2255	0	0	0	1812	568	0	0	1080	559	119	0	0	70
PFT2	1704	1603	387	694	1760	787	3542	212	1066	886	811	939	976	733	1472
PFT3	1314	2502	2696	600	1446	2255	922	557	1380	957	627	42	0	1669	304
PFT4	1641	2473	2769	554	1262	1876	1241	554	1190	1215	1019	536	607	836	801
PFT5	448	1338	462	369	1210	702	925	326	922	795	745	765	1068	1206	651
PFT6	729	821	187	0	262	48	214	2026	218	1417	946	0	0	174	0

Table A1.i The MFRP values as a function of regions and PFT in September.

Regions / PFTs	BONA	WTNA	ETNA	CEAM	NHSA	SHSA	EURO	MIDE	NHAF	SHAF	BOAS	CEAS	SEAS	EQAS	AUST
PFT1	1810	1873	0	0	0	2046	729	0	0	1000	2017	0	0	0	0
PFT2	1724	818	969	756	1681	702	176	252	1055	956	681	1067	713	969	1150
PFT3	1362	2021	2318	48	1705	950	632	338	1252	860	374	86	0	1699	149
PFT4	1367	2211	420	640	1265	1684	814	651	910	965	995	339	619	931	1026
PFT5	808	1371	478	364	1141	732	782	527	849	753	906	367	766	773	556
PFT6	969	179	122	0	461	0	231	269	463	1710	670	40	0	430	0

Table A1.j The MFRP values as a function of regions and PFT in October.

Regions / PFTs	BONA	WTNA	ETNA	CEAM	NHSA	SHSA	EURO	MIDE	NHAF	SHAF	BOAS	CEAS	SEAS	EQAS	AUST
PFT1	1047	1127	0	0	0	2515	0	0	0	1084	1743	97	0	0	0
PFT2	1067	936	320	806	1594	826	92	159	1166	1019	674	319	670	1699	844
PFT3	159	2873	3362	41	1678	376	362	503	1259	888	303	186	0	1741	35
PFT4	963	1697	1121	442	1220	1061	700	600	818	1294	1024	333	659	1008	867
PFT5	1234	1891	1684	477	958	497	450	457	642	1287	932	222	721	1669	838
PFT6	283	539	103	0	333	0	257	730	572	2016	263	255	0	1339	0

Table A1.k The MFRP values as a function of regions and PFT in November.

Regions / PFTs	BONA	WTNA	ETNA	CEAM	NHSA	SHSA	EURO	MIDE	NHAF	SHAF	BOAS	CEAS	SEAS	EQAS	AUST
PFT1	941	625	0	0	0	692	0	0	0	0	127	163	0	0	127
PFT2	601	349	411	944	1491	442	0	180	1354	596	513	560	507	1761	571
PFT3	0	3052	3019	0	1794	765	279	628	1319	169	421	142	0	1516	0
PFT4	140	788	330	456	1121	1219	329	685	714	556	813	1151	965	994	842
PFT5	564	1420	320	377	831	394	378	587	643	1050	927	230	873	1408	504
PFT6	0	0	141	0	619	0	246	2807	678	0	259	72	0	1313	0

Table A1.l The MFRP values as a function of regions and PFT in December.

Regions / PFTs	BONA	WTNA	ETNA	CEAM	NHSA	SHSA	EURO	MIDE	NHAF	SHAF	BOAS	CEAS	SEAS	EQAS	AUST
PFT1	734	689	0	0	0	230	0	0	0	0	97	843	0	0	0
PFT2	454	325	1109	866	1110	471	68	416	1407	133	682	834	450	2355	628
PFT3	107	886	589	41	1853	242	376	459	983	271	374	101	0	1462	0
PFT4	226	605	578	549	939	1882	312	754	923	476	518	565	526	964	834
PFT5	169	752	408	373	824	408	392	625	472	422	583	437	235	1642	626
PFT6	0	0	369	0	373	0	267	219	596	0	338	75	0	765	0

REFERENCES

Adam, M., Pahlow, M., Kovalev, V. A., Ondov, J. M., Parlange, M. B. and Nair, N.: Aerosol optical characterization by nephelometer and lidar: The Baltimore Supersite experiment during the Canadian forest fire smoke intrusion, J. Geophys. Res. D Atmos., 109(16), 1–15, doi:10.1029/2003JD004047, 2004.

Aleman, J. C., Blarquez, O., Gourlet-Fleury, S., Bremond, L. and Favier, C.: Tree cover in Central Africa: Determinants and sensitivity under contrasted scenarios of global change, Sci. Rep., 7(December 2016), 1–12, doi:10.1038/srep41393, 2017.

Aleman, J. C., Jarzyna, M. A. and Staver, A. C.: Forest extent and deforestation in tropical Africa since 1900, Nat. Ecol. Evol., 2(1), 26–33, doi:10.1038/s41559-017-0406-1, 2018.

Allen, R. J., Sherwood, S. C., Norris, J. R. and Zender, C. S.: Recent Northern Hemisphere tropical expansion primarily driven by black carbon and tropospheric ozone, Nature, 485(7398), 350–354, doi:10.1038/nature11097, 2012.

Andela, N. and van der Werf, G. R.: Recent trends in African fires driven by cropland expansion and El Niño to La Niña transition, Nat. Clim. Chang., 4(September), 791–795, doi:10.1038/nclimate2313, 2014a.

Andela, N. and van der Werf, G. R.: Recent trends in African fires driven by cropland expansion and El Niño to La Niña transition, Nat. Clim. Chang., advance on(September), 791–795, doi:10.1038/nclimate2313, 2014b.

Andela, N., Morton, D. C., Giglio, L., Chen, Y., van der Werf, G. R., Kasibhatla, P. S., Defries, R. S., Collatz, G. J., Hantson, S., Kloster, S., Bachelet, D., Forrest, M., Lasslop, G., Li, F., Mangeon, S., Melton, J., Yue, C. and Randerson, J. T.: A human-driven decline in global burned area, Science (80-.)., 356(6345), 1356–1362, doi:10.1126/science.aal4108, 2017.

Andreae, M. O. and Merlet, P.: Emission of trace gases and aerosols from biomass burning, Global Biogeochem. Cycles, 15(4), 955–966, doi:10.1029/2000GB001382, 2001.

Arden Pope III, C., Majid, E. and W., D. D.: Fine-Particulate Air Pollution and Life Expectancy in the United States, N. Engl. J. Med., 360(4), 376–386,

doi:10.1056/NEJMsa0805646, 2009.

Bates, J. T., Weber, R. J., Abrams, J., Verma, V., Fang, T., Klein, M., Strickland, M. J., Sarnat, S. E., Chang, H. H., Mulholland, J. A., Tolbert, P. E. and Russell, A. G.: Reactive Oxygen Species Generation Linked to Sources of Atmospheric Particulate Matter and Cardiorespiratory Effects, Environ. Sci. Technol., 49(22), 13605–13612, doi:10.1021/acs.est.5b02967, 2015.

Bauer, S. E. and Menon, S.: Aerosol direct, indirect, semidirect, and surface albedo effects from sector contributions based on the IPCC AR5 emissions for preindustrial and present-day conditions, J. Geophys. Res. Atmos., 117(1), 1–15, doi:10.1029/2011JD016816, 2012.

Boucher, O., Randall, D., Artaxo, P., Bretherton, C., Feingold, G., Forster, P., Kerminen, V.-M. V.-M., Kondo, Y., Liao, H., Lohmann, U., Rasch, P., Satheesh, S. K., Sherwood, S., Stevens, B., Zhang, X. Y. and Zhan, X. Y.: IPCC AR5 Clouds and Aerosols., 2013.

Browman, D. M. J. S., Balch, J. K., Artaxo, P., Bond, W. J., Carlson, J. M., Cochrane, M. A., D'Antonio, C. M. A., DeFries, R. S., Doyle, J. C., Harrison, S. P., Johnston, F. H., Keeley, J. E., Krawchuk, M. A., Kull, C. a, Marston, J. B., Moritz, M. a, Prentice, I. C., Roos, C. I., Scott, A. C., Swetnam, T. W., van der Werf, G. R., Bowman, D. M. J. S., S.J., P., D'Antonio, C. M. and Pyne, S. J.: Fire in the Earth System, Science (80-.)., 324(5926), 481–484, doi:10.1126/science.1163886, 2009.

Channan, S., Collins, K. and Emanuel, W. R.: Global mosaics of the standard MODIS land cover type data, Univ. Maryl. Pacific Northwest Natl. Lab. Coll. Park. Maryland, USA, 30, 2014.

Chen, Y., Morton, D. C., Andela, N., Giglio, L. and Randerson, J. T.: How much global burned area can be forecast on seasonal time scales using sea surface temperatures?, Environ. Res. Lett., 11(4), 45001, doi:10.1088/1748-9326/11/4/045001, 2016a.

Chen, Y., Morton, D. C., Andela, N., Giglio, L. and Randerson, J. T.: How much global burned area can be forecast on seasonal time scales using sea surface temperatures?, Environ. Res. Lett., 11(4), 45001, doi:10.1088/1748-9326/11/4/045001, 2016b.

Chen, Y., Morton, D. C., Andela, N., Giglio, L. and Randerson, J. T.: How much global burned area can be forecast on seasonal time scales using sea surface temperatures?, Environ. Res. Lett., 11, 45001, doi:10.1088/1748-9326/11/4/045001, 2016c.

Christoudias, T., Pozzer, A. and Lelieveld, J.: Influence of the North Atlantic Oscillation on air pollution transport, Atmos. Chem. Phys., 12(2), 869–877, doi:10.5194/acp-12-869-2012, 2012.

Colarco, P. R.: Transport of smoke from Canadian forest fires to the surface near Washington, D.C.: Injection height, entrainment, and optical properties, J. Geophys. Res., 109(D6), 1–12, doi:10.1029/2003JD004248, 2004.

DeBell, L. J., Talbot, R. W., Dibb, J. E., Munger, J. W., Fischer, E. V. and Frolking, S. E.: A major regional air pollution event in the northeastern United States caused by extensive forest fires in Quebec, Canada, J. Geophys. Res. D Atmos., 109(19), 1–16, doi:10.1029/2004JD004840, 2004.

Delfino, R. J., Sioutas, C. and Malik, S.: Potential role of ultrafine particles in associations between airborne particle mass and cardiovascular health, Environ. Health Perspect., 113(8), 934–946, doi:10.1289/ehp.7938, 2005.

Dempsey, F.: Forest fire effects on air quality in Ontario: Evaluation of several recent examples, Bull. Am. Meteorol. Soc., 94(7), 1059–1064, doi:10.1175/BAMS-D-11-00202.1, 2013.

Dirksen, R. J., Folkert Boersma, K., De Laat, J., Stammes, P., Van Der Werf, G. R., Martin, M. V. and Kelder, H. M.: An aerosol boomerang: Rapid around-the-world transport of smoke from the December 2006 Australian forest fires observed from space, J. Geophys. Res. Atmos., 114(21), 1–15, doi:10.1029/2009JD012360, 2009.

Doherty, S. J., Dang, C., Hegg, D. A., Zhang, R. R., Warren, S. G., Ames, R. B., Fox, D. G., Malm, W. C., Schichtel, B. A., Bowman, D. M. J. S., Williamson, G. J., Abatzoglou, J. T., Kolden, C. A., Cochrane, M. A., Smith, A. M. S., Liu, Y., Goodrick, S. L., Heilman, W. E., Liu, Y., Urbanski, S. P., Kovalev, V., Mickler, R., Yang, J., Tian, H., Tao, B., Ren, W., Kush, J., Liu, Y., Wang, Y., Rothermel, R. C., Veraverbeke, S., Hook, S. J., Fallis, A. ., Ratio, N. B., Bhattarai, K. P., Picotte, J., Howard, S. M., Boschetti, L., Roy, D. P., Hoffmann, A. A., Humber, M., Scott, J. H., Groot, W. J. De, Anderson, G. K., Sandberg, D. V., Norheim, R. A., EPA, Liu, Y., Dentener, F., Kinne, S., Bond, T. C., Boucher, O., Cofala, J., Generoso, S., Ginoux, P., Gong, S., Hoelzemann, J. J., Ito, A., Marelli, L., Penner, J. E., Putaud, J.-P., Textor, C., Schulz, M., van der Werf, G. R., Wilson, J., Devore, J., Tai, A. P. K., Martin, M. V., Heald, C. L., Wang, Y., Wang, M., Zhang, R. R., Ghan, S. J., Lin, Y., Hu, J., Pan, B., Levy, M., Jiang, J. H., Molina, M. J., Biasutti, M., Urbanski, S. P., Miller, C., Ager, A. A., Knorr, W., Lehsten, V., Arneth, A., Huber, S., Fensholt, R., Rasmussen, K., French, N. H. F., de Groot, W. J. W. J., Jenkins, L. K., Rogers, B. M., Alvarado, E., Amiro, B. B. D., De Jong, B., Goetz, S., Hoy, E., Hyer, E., et al.: Modeling of biomass smoke injection into the lower stratosphere by a large forest fire (Part

II): sensitivity studies, Atmos. Chem. Phys., 6(4), 5261–5277, doi:10.5194/acpd-6-6081-2006, 2013.

Donaldson, K., Stone, V., Seaton, A. and MacNee, W.: Ambient particle inhalation and the cardiovascular system: Potential mechanisms, Environ. Health Perspect., 109(SUPPL. 4), 523–527, doi:10.2307/3454663, 2001.

Dreessen, J., Sullivan, J. and Delgado, R.: Observations and impacts of transported Canadian wildfire smoke on ozone and aerosol air quality in the Maryland region on June 9–12, 2015, J. Air Waste Manage. Assoc., 66(9), 842–862, doi:10.1080/10962247.2016.1161674, 2016.

Ellicott, E., Vermote, E., Giglio, L. and Roberts, G.: Estimating biomass consumed from fire using MODIS FRE, Geophys. Res. Lett., 36(13), 1–5, doi:10.1029/2009GL038581, 2009.

Evangeliou, N., Balkanski, Y., Hao, W. M., Petkov, A., Silverstein, R. P., Corley, R., Nordgren, B. L., Urbanski, S. P., Eckhardt, S., Stohl, A., Tunved, P., Crepinsek, S., Jefferson, A., Sharma, S., Nøjgaard, J. K. and Skov, H.: Wildfires in Northern Eurasia affect the budget of black carbon in the Arctic. A 12-year retrospective synopsis (2002–2013)., Atmos. Chem. Phys. Discuss., (February), 1–41, doi:10.5194/acp-2015-994, 2016.

Fang, T., Verma, V., T Bates, J., Abrams, J., Klein, M., Strickland, J. M., Sarnat, E. S., Chang, H. H., Mulholland, A. J., Tolbert, E. P., Russell, G. A. and Weber, J. R.: Oxidative potential of ambient water-soluble PM2.5 in the southeastern United States: Contrasts in sources and health associations between ascorbic acid (AA) and dithiothreitol (DTT) assays, Atmos. Chem. Phys., 16(6), 3865–3879, doi:10.5194/acp-16-3865-2016, 2016.

Fiore, A. and Jacob, D.: Application of empirical orthogonal functions to evaluate ozone simulations with regional and global models, J. Geophys. …, 108(D14), 4431, doi:10.1029/2002JD003151, 2003.

Fiore, A. M., Pierce, R. B., Dickerson, R. R. and Lin, M.: Detecting and attributing episodic high background ozone events, EM Air Waste Manag. Assoc. Mag. Environ. Manag., (FEB), 22–28, 2014.

Freeborn, P. H., Wooster, M. J., Hao, W. M., Ryan, C. A., Nordgren, B. L., Baker, S. P. and Ichoku, C.: Relationships between energy release, fuel mass loss, and trace gas an aerosol emissions during laboratory biomass fires, J. Geophys. Res. Atmos., 113(1), 1–17, doi:10.1029/2007JD008679, 2008.

Freitas, S. R., Longo, K. M., Chatfield, R., Latham, D., Silva Dias, M. a. F., Andreae, M. O., Prins, E., Santos, J. C., Gielow, R. and Carvalho, J. a.: Including the sub-grid scale plume rise of vegetation fires in low resolution atmospheric transport models, Atmos. Chem. Phys. Discuss., 6(6), 11521–11559, doi:10.5194/acpd-6-11521-2006, 2006.

Freitas, S. R., Longo, K. M., Chatfield, R., Latham, D., Silva Dias, M. a. F., Andreae, M. O., Prins, E., Santos, J. C., Gielow, R. and Carvalho, J. a.: Including the sub-grid scale plume rise of vegetation fires in low resolution atmospheric transport models, Atmos. Chem. Phys. Discuss., 7(7), 3385–3398, doi:10.5194/acpd-6-11521-2006, 2007.

Freitas, S. R., Longo, K. M., Trentmann, J. and Latham, D.: Technical Note: Sensitivity of 1-D smoke plume rise models to the inclusion of environmental wind drag, Atmos. Chem. Phys., 10(2), 585–594, doi:10.5194/acp-10-585-2010, 2010.

Gégo, E., Porter, P. S., Gilliland, A. and Rao, S. T.: Observation-based assessment of the impact of nitrogen oxides emissions reductions on ozone air quality over the Eastern United States, J. Appl. Meteorol. Climatol., 46(7), 994–1008, doi:10.1175/JAM2523.1, 2007.

Giglio, L.: MODIS collection 5 active fire product user's guide version 2.4. [online] Available from: http://198.118.255.205/sites/default/files/field/document/MODIS_Fire_users_Guide_2.4.pdf, 2013.

Giglio, L., Csiszar, I. and Justice, C. O.: Global distribution and seasonality of active fires as observed with the Terra and Aqua Moderate Resolution Imaging Spectroradiometer (MODIS) sensors, J. Geophys. Res. Biogeosciences, 111(2), 1–12, doi:10.1029/2005JG000142, 2006.

Giglio, L., Randerson, J. T. and Van Der Werf, G. R.: Analysis of daily, monthly, and annual burned area using the fourth-generation global fire emissions database (GFED4), J. Geophys. Res. Biogeosciences, 118(1), 317–328, doi:10.1002/jgrg.20042, 2013.

de Gouw, J. A., Warneke, C., Stohl, A., Wollny, A. G., Brock, C. A., Cooper, O. R., Holloway, J. S., Trainer, M., Fehsenfeld, F. C., Atlas, E. L., Donnelly, S. G., Stroud, V. and Lueb, A.: Volatile organic compounds composition of merged and aged forest fire plumes from Alaska and western Canada, J. Geophys. Res. Atmos., 111(10), 1–20, doi:10.1029/2005JD006175, 2006.

Grell, G., Freitas, S. R., Stuefer, M. and Fast, J.: Inclusion of biomass burning in

WRF-Chem: Impact of wildfires on weather forecasts, Atmos. Chem. Phys., 11(11), 5289–5303, doi:10.5194/acp-11-5289-2011, 2011.

Hirota, M., Holmgren, M., Nes, E. H. Van and Scheffer, M.: Global Resilience of Tropical Forest and Savanna to Critical Transitions, Science (80-.)., 334(October), 232–235, doi:10.1126/science.1210657, 2011.

Hodnebrog, Ø., Myhre, G., Forster, P. M., Sillmann, J. and Samset, B. H.: Local biomass burning is a dominant cause of the observed precipitation reduction in southern Africa, Nat. Commun., 7, 11236, doi:10.1038/ncomms11236, 2016.

Hu, Y., Odman, M. T., Chang, M. E., Jackson, W., Lee, S., Edgerton, E. S., Baumann, K. and Russell, A. G.: Simulation of Air Quality Impacts from Prescribed Fires on an Urban Area, Environ. Sci. Technol., 42(10), 3676–3682, doi:10.1021/es071703k, 2008.

Ichoku, C., Ellison, L. T., Willmot, K. E., Matsui, T., Dezfuli, A. K., Gatebe, C. K., Wang, J., Wilcox, E. M., Lee, J., Adegoke, J., Okonkwo, C., Bolten, J., Policelli, F. S. and Habib, S.: Biomass burning, land-cover change, and the hydrological cycle in Northern sub-Saharan Africa, Environ. Res. Lett., 11(9), 95005, doi:10.1088/1748-9326/11/9/095005, 2016.

Jaffe, D., Hafner, W., Chand, D., Westerling, A. and Spracklen, D.: Interannual variations in PM2.5 due to wildfires in the Western United States, Environ. Sci. Technol., 42(8), 2812–2818, doi:10.1021/es702755v, 2008.

Jaffe, D. A. and Wigder, N. L.: Ozone production from wildfires: A critical review, Atmos. Environ., 51, 1–10, doi:10.1016/j.atmosenv.2011.11.063, 2012.

Jiang, Y., Lu, Z., Liu, X., Qian, Y., Zhang, K., Wang, Y. and Yang, X. Q.: Impacts of global open-fire aerosols on direct radiative, cloud and surface-albedo effects simulated with CAM5, Atmos. Chem. Phys., 16(23), 14805–14824, doi:10.5194/acp-16-14805-2016, 2016.

Kahn, R. A., Li, W. H., Moroney, C., Diner, D. J., Martonchik, J. V. and Fishbein, E.: Aerosol source plume physical characteristics from space-based multiangle imaging, J. Geophys. Res. Atmos., 112(11), 1–20, doi:10.1029/2006JD007647, 2007.

Kahn, R. A., Chen, Y., Nelson, D. L., Leung, F. Y., Li, Q., Diner, D. J. and Logan, J. A.: Wildfire smoke injection heights: Two perspectives from space, Geophys. Res. Lett.,

35(4), 18–21, doi:10.1029/2007GL032165, 2008.

Kalnay, E., Kanamitsu, M., Kistler, R., Collins, W., Deaven, D., Gandin, L., Iredell, M., Saha, S., White, G., Woollen, J., Zhu, Y., Chelliah, M., Ebisuzaki, W., Higgins, W., Janowiak, J., Mo, K. C., Ropelewski, C., Wang, J., Leetmaa, A., Reynolds, R., Jenne, R. and Joseph, D.: The NCEP/NCAR 40-year reanalysis project, Bull. Am. Meteorol. Soc., 77(3), 437–471, doi:10.1175/1520-0477(1996)077<0437:TNYRP>2.0.CO;2, 1996.

Kang, C. M., Gold, D. and Koutrakis, P.: Downwind O3 and PM2.5 speciation during the wildfires in 2002 and 2010, Atmos. Environ., 95, 511–519, doi:10.1016/j.atmosenv.2014.07.008, 2014.

Keegan, K. M., Albert, M. R., McConnell, J. R. and Baker, I.: Climate change and forest fires synergistically drive widespread melt events of the Greenland Ice Sheet., Proc. Natl. Acad. Sci. U. S. A., 111(22), 7964–7, doi:10.1073/pnas.1405397111, 2014.

Künzli, N., Avol, E., Wu, J., Gauderman, W. J., Rappaport, E., Millstein, J., Bennion, J., McConnell, R., Gilliland, F. D., Berhane, K., Lurmann, F., Winer, A. and Peters, J. M.: Health effects of the 2003 Southern California wildfires on children, Am. J. Respir. Crit. Care Med., 174(11), 1221–1228, doi:10.1164/rccm.200604-519OC, 2006.

Lamarque, J. F., Bond, T. C., Eyring, V., Granier, C., Heil, A., Klimont, Z., Lee, D., Liousse, C., Mieville, A., Owen, B., Schultz, M. G., Shindell, D., Smith, S. J., Stehfest, E., Van Aardenne, J., Cooper, O. R., Kainuma, M., Mahowald, N., McConnell, J. R., Naik, V., Riahi, K. and Van Vuuren, D. P.: Historical (1850-2000) gridded anthropogenic and biomass burning emissions of reactive gases and aerosols: Methodology and application, Atmos. Chem. Phys., 10(15), 7017–7039, doi:10.5194/acp-10-7017-2010, 2010.

Lamb, R. G. and Durran, D. R.: Eddy Diffusivities Derived from a Numerical Model of the Convective Planetary Boundary Layer (’)., NUOVO Cim., 1C, 1–17, 1978.

Latham, D.: PLUMP: A one-dimensional plume predictor and cloud model for fire and smoke managers, Gen. Tech. Rep. INT-GTR-314, Intermt. Res. Station. USDA For. Serv., 11526, 11528–11529, 1994.

LAWRENCE, P. J., FEDDEMA, J. J., BONAN, G. B., A.MEEHL, G., O’NEILL, B. C., OLESON, K. W., LEVIS, S., LAWRENCE, D. M., KLUZEK, E., LINDSAY, K. and THORNTON, P. E.: Simulating the Biogeochemical and Biogeophysical Impacts of Transient Land Cover Change and Wood Harvest in the Community Climate System Model (CCSM4) from 1850 to 2100, J. Clim., 25(9), 3071–3095, doi:10.1175/JCLI-D-11-00256.1, 2012.

Levy, R. C., Remer, L. A., Mattoo, S., Vermote, E. F. and Kaufman, Y. J.: Second-generation operational algorithm: Retrieval of aerosol properties over land from inversion of Moderate Resolution Imaging Spectroradiometer spectral reflectance, J. Geophys. Res. Atmos., 112(13), 1–21, doi:10.1029/2006JD007811, 2007.

Li, Y., Sulla-Menashe, D., Motesharrei, S., Song, X. P., Kalnay, E., Ying, Q., Li, S. and Ma, Z.: Inconsistent estimates of forest cover change in China between 2000 and 2013 from multiple datasets: Differences in parameters, spatial resolution, and definitions, Sci. Rep., 7(1), 1–12, doi:10.1038/s41598-017-07732-5, 2017.

Liu, X., Easter, R. C., Ghan, S. J., Zaveri, R., Rasch, P., Shi, X., Lamarque, J. F., Gettelman, A., Morrison, H., Vitt, F., Conley, A., Park, S., Neale, R., Hannay, C., Ekman, A. M. L., Hess, P., Mahowald, N., Collins, W., Iacono, M. J., Bretherton, C. S., Flanner, M. G. and Mitchell, D.: Toward a minimal representation of aerosols in climate models: Description and evaluation in the Community Atmosphere Model CAM5, Geosci. Model Dev., 5(3), 709–739, doi:10.5194/gmd-5-709-2012, 2012.

Liu, Y.: Variability of wildland fire emissions across the contiguous United States, Atmos. Environ., 38(21), 3489–3499, doi:10.1016/j.atmosenv.2004.02.004, 2004.

Liu, Y., Stanturf, J. and Goodrick, S.: Trends in global wildfire potential in a changing climate, For. Ecol. Manage., 259(4), 685–697, doi:10.1016/j.foreco.2009.09.002, 2010.

Liu, Y., Goodrick, S. and Heilman, W.: Wildland fire emissions, carbon, and climate: Wildfire-climate interactions, For. Ecol. Manage., 317, 80–96, doi:10.1016/j.foreco.2013.02.020, 2014.

Lutsch, E., Dammers, E., Conway, S. and Strong, K.: Long-range Transport of NH 3 , CO, HCN and C 2 H 6 from the 2014 Canadian Wildfires, Geophys. Res. Lett., 1–12, doi:10.1002/2016GL070114, 2016.

Ma, X., Bartlett, K., Harmon, K. and Yu, F.: Comparison of AOD between CALIPSO and MODIS: Significant differences over major dust and biomass burning regions, Atmos. Meas. Tech., 6(9), 2391–2401, doi:10.5194/amt-6-2391-2013, 2013.

Madden, J. M., Mölders, N. and Sassen, K.: Assessment of WRF / Chem Simulated Vertical Distributions of Particulate Matter from the 2009 Minto Flats South Wildfire in Interior Alaska by CALIPSO Total Backscatter and Depolarization Measurements, Open J. Air Pollut., 4(September), 119–138 [online] Available from: http://www.scirp.org/journal/ojap

http://dx.doi.org/10.4236/ojap.2015.43012%5CnAssessment, 2015.

Maidment, R. I., Allan, R. P. and Black, E.: Recent observed and simulated changes in precipitation over Africa, Geophys. Res. Lett., 42(19), 1–10, doi:10.1002/2015GL065765.Received, 2015.

Malm, W. C., Schichtel, B. A., Pitchford, M. L., Ashbaugh, L. L. and Eldred, R. A.: Spatial and monthly trends in speciated fine particle concentration in the United States, J. Geophys. Res. Atmos., 109(D3), n/a-n/a, doi:10.1029/2003JD003739, 2004.

Mayer, A. L. and Khalyani, A. H.: Grass Trumps Trees with Fire, Science (80-.)., 334(6053), 188–189, doi:10.1126/science.1213908, 2011.

McKeen, S. A., Wotawa, G., Parrish, D. D., Holloway, J. S., Buhr, M. P., Hübler, G., Fehsenfeld, F. C. and Meagher, J. F.: Ozone production from Canadian wildfires during June and July of 1995, J. Geophys. Res. Atmos., 107(14), 1–25, doi:10.1029/2001JD000697, 2002.

Monks, S. A., Arnold, S. R. and Chipperfield, M. P.: Evidence for El Niño-Southern Oscillation (ENSO) influence on Arctic CO interannual variability through biomass burning emissions, Geophys. Res. Lett., 39(14), 1–6, doi:10.1029/2012GL052512, 2012.

Mu, M., Randerson, J. T., Van Der Werf, G. R., Giglio, L., Kasibhatla, P., Morton, D., Collatz, G. J., Defries, R. S., Hyer, E. J., Prins, E. M., Griffith, D. W. T., Wunch, D., Toon, G. C., Sherlock, V. and Wennberg, P. O.: Daily and 3-hourly variability in global fire emissions and consequences for atmospheric model predictions of carbon monoxide, J. Geophys. Res. Atmos., 116(24), 1–19, doi:10.1029/2011JD016245, 2011.

Myneni, R. B., Yang, W., Nemani, R. R., Huete, A. R., Dickinson, R. E., Knyazikhin, Y., Didan, K., Fu, R., Negrón Juárez, R. I., Saatchi, S. S., Hashimoto, H., Ichii, K., Shabanov, N. V, Tan, B., Ratana, P., Privette, J. L., Morisette, J. T., Vermote, E. F., Roy, D. P., Wolfe, R. E., Friedl, M. a, Running, S. W., Votava, P., El-Saleous, N., Devadiga, S., Su, Y. and Salomonson, V. V: Large seasonal swings in leaf area of Amazon rainforests., Proc. Natl. Acad. Sci. U. S. A., 104(12), 4820–4823, doi:10.1073/pnas.0611338104, 2007.

Neale, R. B., Gettelman, A., Park, S., Chen, C., Lauritzen, P. H., Williamson, D. L., Conley, A. J., Kinnison, D., Marsh, D., Smith, A. K., Vitt, F., Garcia, R., Lamarque, J., Mills, M., Tilmes, S., Morrison, H., Cameron-smith, P., Collins, W. D., Iacono, M. J., Easter, R. C., Liu, X., Ghan, S. J., Rasch, P. J. and Taylor, M. a: Description of the NCAR Community Atmosphere Model (CAM 5.0). NCAR Technical Notes., Natl. Cent. Atmos.

Res., 214, doi:10.5065/D6N877R0., 2012.

Neami, R. R. ., Keeling, C. D. . and Hashimoto, H. . E. Al: Climate-Driven Increases in Global Terrestrial Net Primary Production From 192 To 1999, Science, 300(5625), 1560–3, doi:10.1126/science.1082750, 2003.

Oleson, K. W., Lawrence, D. M., Gordon, B., Flanner, M. G., Kluzek, E., Peter, J., Levis, S., Swenson, S. C., Thornton, E., Dai, A., Decker, M., Dickinson, R., Feddema, J., Heald, C. L., Lamarque, J., Niu, G., Qian, T., Running, S., Sakaguchi, K., Slater, A., Stöckli, R., Wang, A., Yang, L., Zeng, X. and Zeng, X.: Technical Description of version 4 . 0 of the Community Land Model (CLM)., 2010.

Pablo E. Saide, Thompson, G., Eidhammer, T., Silva, A. M. da, Pierce, R. B. and Carmichael, G. R.: Assessment of biomass burning smoke influence on environmental conditions for multiyear tornado outbreaks by combining aerosol-aware microphysics and fire emission constraints, , (121), 10294–10311, doi:10.1002/2015JD024524.Received, 2016.

Park, R. J., Jacob, D. J. and Logan, J. A.: Fire and biofuel contributions to annual mean aerosol mass concentrations in the United States, Atmos. Environ., 41(35), 7389–7400, doi:10.1016/j.atmosenv.2007.05.061, 2007.

Paugam, R., Wooster, M., Freitas, S. and Val Martin, M.: A review of approaches to estimate wildfire plume injection height within large-scale atmospheric chemical transport models, Atmos. Chem. Phys., 16(2), 907–925, doi:10.5194/acp-16-907-2016, 2016.

Pechony, O. and Shindell, D. T.: Driving forces of global wildfires over the past millennium and the forthcoming century, Proc. Natl. Acad. Sci., 107(45), 19167–19170, doi:10.1073/pnas.1003669107, 2010.

Pfister, G. G., Avise, J., Wiedinmyer, C., Edwards, D. P., Emmons, L. K., Diskin, G. D., Podolske, J. and Wisthaler, A.: CO source contribution analysis for California during ARCTAS-CARB, Atmos. Chem. Phys., 11(15), 7515–7532, doi:10.5194/acp-11-7515-2011, 2011.

Randerson, J. T., Chen, Y., Van Der Werf, G. R., Rogers, B. M. and Morton, D. C.: Global burned area and biomass burning emissions from small fires, J. Geophys. Res. Biogeosciences, 117(4), doi:10.1029/2012JG002128, 2012.

Saha, S., Moorthi, S., Wu, X., Wang, J., Nadiga, S., Tripp, P., Behringer, D., Hou, Y. T., Chuang, H. Y., Iredell, M., Ek, M., Meng, J., Yang, R., Mendez, M. P., Van Den Dool, H., Zhang, Q., Wang, W., Chen, M. and Becker, E.: The NCEP climate forecast system version 2, J. Clim., 27(6), 2185–2208, doi:10.1175/JCLI-D-12-00823.1, 2014.

Sankaran, M., Ratnam, J. and Hanan, N. P.: Tree-grass coexistence in savannas revisited - Insights from an examination of assumptions and mechanisms invoked in existing models, Ecol. Lett., 7(6), 480–490, doi:10.1111/j.1461-0248.2004.00596.x, 2004.

Sankaran, M., Hanan, N. P., Scholes, R. J., Ratnam, J., Augustine, D. J., Cade, B. S., Gignoux, J., Higgins, S. I., Le Roux, X., Ludwig, F., Ardo, J., Banyikwa, F., Bronn, A., Bucini, G., Caylor, K. K., Coughenour, M. B., Diouf, A., Ekaya, W., Feral, C. J., February, E. C., Frost, P. G. H., Hiernaux, P., Hrabar, H., Metzger, K. L., Prins, H. H. T., Ringrose, S., Sea, W., Tews, J., Worden, J. and Zambatis, N.: Determinants of woody cover in African savannas., Nature, 438(7069), 846–849, doi:10.1038/nature04070, 2005.

Sankaran, M., Ratnam, J. and Hanan, N.: Woody cover in African savannas: The role of resources, fire and herbivory, Glob. Ecol. Biogeogr., 17(2), 236–245, doi:10.1111/j.1466-8238.2007.00360.x, 2008.

Sapkota, A., Symons, J. M., Kleissl, J., Wang, L., Parlange, M. B., Ondov, J., Breysse, P. N., Diette, G. B., Eggleston, P. a and Buckley, T. J.: Impact of the 2002 Canadian forest fires on particulate matter air quality in Baltimore city., Environ. Sci. Technol., 39(1), 24–32, doi:10.1021/es035311z, 2005.

Saunders, R. O. and Waugh, D. W.: Variability and potential sources of summer PM2.5 in the Northeastern United States, Atmos. Environ., 117, 259–270, doi:10.1016/j.atmosenv.2015.07.007, 2015.

Schuster, G. L., Vaughan, M., MacDonnell, D., Su, W., Winker, D., Dubovik, O., Lapyonok, T. and Trepte, C.: Comparison of CALIPSO aerosol optical depth retrievals to AERONET measurements, and a climatology for the lidar ratio of dust, Atmos. Chem. Phys., 12(16), 7431–7452, doi:10.5194/acp-12-7431-2012, 2012.

Seddon, A. W. R., Macias-Fauria, M., Long, P. R., Benz, D. and Willis, K. J.: Sensitivity of global terrestrial ecosystems to climate variability, Nature, 531(7593), 229–232, doi:10.1038/nature16986, 2016.

Simpson, J. and Wiggert, V.: models of percipitating cumulus towers, Mon. Weather Rev., 97(7), 471–489, doi:10.1126/science.27.693.594, 1969.

Sofiev, M., Ermakova, T. and Vankevich, R.: Evaluation of the smoke-injection height from wild-land fires using remote-sensing data, Atmos. Chem. Phys., 12(4), 1995–2006, doi:10.5194/acp-12-1995-2012, 2012.

Sofiev, M., Vankevich, R., Ermakova, T. and Hakkarainen, J.: Global mapping of maximum emission heights and resulting vertical profiles of wildfire emissions, Atmos. Chem. Phys., 13(14), 7039–7052, doi:10.5194/acp-13-7039-2013, 2013.

Staal, A., Dekker, S. C., Xu, C. and van Nes, E. H.: Bistability, Spatial Interaction, and the Distribution of Tropical Forests and Savannas, Ecosystems, 19(6), 1080–1091, doi:10.1007/s10021-016-0011-1, 2016.

Staver, A. C. and Levin, S. A.: Integrating Theoretical Climate and Fire Effects on Savanna and Forest Systems, Am. Nat., 180(2), 211–224, doi:10.1086/666648, 2012.

Staver, A. C., Archibald, S. and Levin, S.: The Global Extent and Determinants of, Science (80-.)., 334(6053), 230–232, doi:10.1126/science.1210465, 2011a.

Staver, A. C., Archibald, S. and Levin, S. A.: The Global Extent and Determinants of Savanna and Forest as Alternative Biome States, Science (80-.)., 334(6053), 230–232, doi:10.1126/science.1210465, 2011b.

Staver, A. C., Archibald, S. and Levin, S.: Tree cover in sub-Saharan Africa: Rainfall and fire constrain forest and savanna as alternative stable states, Ecology, 92(5), 1063–1072, doi:10.1890/i0012-9658-92-5-1063, 2011c.

Stein, A. F., Rolph, G. D., Draxler, R. R., Stunder, B. and Ruminski, M.: Verification of the NOAA Smoke Forecasting System: Model Sensitivity to the Injection Height, Weather Forecast., 24(2), 379–394, doi:10.1175/2008WAF2222166.1, 2009.

Tosca, M. G., Randerson, J. T., Zender, C. S., Nelson, D. L., Diner, D. J. and Logan, J. A.: Dynamics of fire plumes and smoke clouds associated with peat and deforestation fires in Indonesia, J. Geophys. Res. Atmos., 116(8), 1–14, doi:10.1029/2010JD015148, 2011.

Tosca, M. G., Randerson, J. T. and Zender, C. S.: Global impact of smoke aerosols from landscape fires on climate and the Hadley circulation, Atmos. Chem. Phys., 13(10), 5227–5241, doi:10.5194/acp-13-5227-2013, 2013a.

Tosca, M. G., Randerson, J. T. and Zender, C. S.: Global impact of smoke aerosols from landscape fires on climate and the Hadley circulation, Atmos. Chem. Phys., 13(10), 5227–5241, doi:10.5194/acp-13-5227-2013, 2013b.

Tosca, M. G., Diner, D. J., Garay, M. J. and Kalashnikova, O. V.: Human-caused fires limit convection in tropical Africa: First temporal observations and attribution, Geophys. Res. Lett., 42(15), 6492–6501, doi:10.1002/2015GL065063, 2015.

Touboul, J. D., Carla, A. and Asher, S.: On the complex dynamics of savanna landscapes, Proc. Natl. Acad. Sci., doi:10.1073/pnas.1712356115, 2017.

Trentmann, J., Andreae, M. O., Graf, H.-F., Hobbs, P. V. V, Ottmar, R. D. D. and Trautmann, T.: Simulation of a biomass-burning plume: Comparison of model results with observations, J. Geophys. Res., 107(D2), 4013, doi:10.1029/2001JD000410, 2002.

Turner, J. S.: Buoyancy effects in fluids, Cambridge University Press., 1979.

Val Martin, M., Logan, J. a., Kahn, D., Leung, F. Y., Nelson, D. and Diner, D.: Smoke injection heights from fires in North America: analysis of 5 years of satellite observations, Atmos. Chem. Phys. Discuss., 9(5), 20515–20566, doi:10.5194/acpd-9-20515-2009, 2009.

Val Martin, M., Kahn, R. A., Logan, J. A., Paugam, R., Wooster, M. and Ichoku, C.: Space-based observational constraints for 1-D fire smoke plume-rise models, J. Geophys. Res. Atmos., 117(22), 1–18, doi:10.1029/2012JD018370, 2012.

Verbesselt, J., Umlauf, N., Hirota, M., Holmgren, M., Van Nes, E. H., Herold, M., Zeileis, A. and Scheffer, M.: Remotely sensed resilience of tropical forests, Nat. Clim. Chang., 6(11), 1028–1031, doi:10.1038/nclimate3108, 2016.

Vermote, E., Ellicott, E., Dubovik, O., Lapyonok, T., Chin, M., Giglio, L. and Roberts, G. J.: An approach to estimate global biomass burning emissions of organic and black carbon from MODIS fire radiative power, J. Geophys. Res. Atmos., 114(18), 1–22, doi:10.1029/2008JD011188, 2009.

van der Werf, G. R., Randerson, J. T., Giglio, L., Collatz, G. J., Kasibhatla, P. S. and Arellano, A. F., J.: Interannual variability in global biomass burning emissions from 1997 to 2004, Atmos. Chem. Phys., 6(11), 3423–3441, doi:10.5194/acpd-6-3175-2006, 2006.

van der Werf, G. R., Randerson, J. T., Giglio, L., van Leeuwen, T. T., Chen, Y., Rogers, B. M., Mu, M., van Marle, M. J. E., Morton, D. C., Collatz, G. J., Yokelson, R. J. and Kasibhatla, P. S.: Global fire emissions estimates during 1997–2015, Earth Syst. Sci. Data Discuss., 1–43, doi:10.5194/essd-2016-62, 2017.

Van Der Werf, G. R., Randerson, J. T., Giglio, L., Gobron, N. and Dolman, A. J.: Climate controls on the variability of fires in the tropics and subtropics, Global Biogeochem. Cycles, 22(3), 1–13, doi:10.1029/2007GB003122, 2008.

Van Der Werf, G. R., Randerson, J. T., Giglio, L., Collatz, G. J., Mu, M., Kasibhatla, P. S., Morton, D. C., Defries, R. S., Jin, Y. and Van Leeuwen, T. T.: Global fire emissions and the contribution of deforestation, savanna, forest, agricultural, and peat fires (1997-2009), Atmos. Chem. Phys., 10(23), 11707–11735, doi:10.5194/acp-10-11707-2010, 2010.

Westerling, a. L., Hidalgo, H. G., Cayan, D. R. and Swetnam, T. W.: Warming and earlier spring increase western U.S. forest wildfire activity, Science (80-.)., 313(5789), 940–3, doi:10.1126/science.1128834, 2006.

Winiger, P., Andersson, A., Eckhardt, S., Stohl, A. and Gustafsson, Ö.: The sources of atmospheric black carbon at a European gateway to the Arctic, Nat. Commun., 7, 12776, doi:10.1038/ncomms12776, 2016.

Winker, D. M., Pelon, J., Coakley, J. A., Ackerman, S. A., Charlson, R. J., Colarco, P. R., Flamant, P., Fu, Q., Hoff, R. M., Kittaka, C., Kubar, T. L., Le Treut, H., McCormick, M. P., Mégie, G., Poole, L., Powell, K., Trepte, K., Vaughan, M. A. and Wielicki, B. A.: The Calipso Mission: A Global 3D View of Aerosols and Clouds, Bull. Am. Meteorol. Soc., 91(9), 1211–1229, doi:10.1175/2010BAMS3009.1, 2010.

Wooster, M. J., Roberts, G., Perry, G. L. W. and Kaufman, Y. J.: Retrieval of biomass combustion rates and totals from fire radiative power observations: FRP derivation and calibration relationships between biomass consumption and fire radiative energy release, J. Geophys. Res. Atmos., 110(24), 1–24, doi:10.1029/2005JD006318, 2005.

Wuyts, B., Champneys, A. R. and House, J. I.: Amazonian forest-savanna bistability and human impact, Nat. Commun., 15519, 1–11, 2017a.

Wuyts, B., Champneys, A. R. and House, J. I.: Amazonian forest-savanna bistability and human impact, Nat. Commun., 8(May), 1–11, doi:10.1038/ncomms15519, 2017b.

Yuan Zhang, Wallace, J. M. and Battisti, D. S.: ENSO-like interdecadal variability: 1900-93, J. Clim., 10(5), 1004–1020, doi:10.1175/1520-0442(1997)010<1004:ELIV>2.0.CO;2, 1997.

Zeng, T. and Wang, Y.: Nationwide summer peaks of OC/EC ratios in the contiguous United States, Atmos. Environ., 45(3), 578–586, doi:10.1016/j.atmosenv.2010.10.038, 2011.